TU/e EINDHOVEN UNIVERSITY OF TECHNOLOGY

Atomic layer deposition on graphene : towards graphene device integration

Citation for published version (APA):
Vervuurt, R. H. J. (2017). *Atomic layer deposition on graphene : towards graphene device integration*. [Phd Thesis 1 (Research TU/e / Graduation TU/e), Applied Physics]. Technische Universiteit Eindhoven.

Document status and date:
Published: 21/09/2017

Document Version:
Publisher's PDF, also known as Version of Record (includes final page, issue and volume numbers)

Please check the document version of this publication:

• A submitted manuscript is the version of the article upon submission and before peer-review. There can be important differences between the submitted version and the official published version of record. People interested in the research are advised to contact the author for the final version of the publication, or visit the DOI to the publisher's website.
• The final author version and the galley proof are versions of the publication after peer review.
• The final published version features the final layout of the paper including the volume, issue and page numbers.

Link to publication

General rights
Copyright and moral rights for the publications made accessible in the public portal are retained by the authors and/or other copyright owners and it is a condition of accessing publications that users recognise and abide by the legal requirements associated with these rights.

• Users may download and print one copy of any publication from the public portal for the purpose of private study or research.
• You may not further distribute the material or use it for any profit-making activity or commercial gain
• You may freely distribute the URL identifying the publication in the public portal.

If the publication is distributed under the terms of Article 25fa of the Dutch Copyright Act, indicated by the "Taverne" license above, please follow below link for the End User Agreement:

www.tue.nl/taverne

Take down policy
If you believe that this document breaches copyright please contact us at:

openaccess@tue.nl

providing details and we will investigate your claim.

Download date: 16. Jul. 2022

Atomic Layer Deposition on Graphene: Towards Graphene Device Integration

PROEFSCHRIFT

ter verkrijging van de graad van doctor aan de Technische Universiteit Eindhoven, op gezag van de rector magnificus prof.dr.ir. F.P.T. Baaijens, voor een commissie aangewezen door het College voor Promoties, in het openbaar te verdedigen op donderdag 21 september 2017 om 16:00 uur

door

René Henricus Jozef Vervuurt

geboren te Roermond

Dit proefschrift is goedgekeurd door de promotoren en de samenstelling van de promotiecommissie is als volgt:

voorzitter:	prof.dr.ir. G.M.W. Kroesen
1e promotor:	prof.dr.ir. W.M.M. Kessels
copromotor:	dr. A.A. Bol
leden:	prof.dr. M.A. Loi (RUG)
	prof.dr. C. Vallée (Université Grenoble Alpes - UGA)
	dr.ir. C.F.J. Flipse
	prof.dr. G. de With
	prof.dr. S. Hofmann (University of Cambridge)

Het onderzoek dat in dit proefschrift wordt beschreven is uitgevoerd in overeenstemming met de TU/e Gedragscode Wetenschapsbeoefening.

The work presented in this thesis is part of the research program of the Foundation for Fundamental Research on Matter (FOM), which is part of the Netherlands Organization for Scientific Research (NWO). The grant for this work is part of the Natuurkunde Projectruimte 12PR3101.



Printed and bound by: Ipskamp Printing, Enschede
Cover design: R.H.J. Vervuurt

A catalogue record is available from the Eindhoven University of Technology Library
ISBN: 978-90-386-4330-4

Contents

1 General Introduction **1**

1.1 Graphene for Future Nano-electronic Applications 3
1.2 Atomic Layer Deposition 7
1.3 Research Objective, Framework & Outline 9

2 Atomic Layer Deposition for Graphene Device Integration **17**

2.1 Introduction 18
2.2 ALD on Pristine Graphene 20
2.3 Uniform ALD on Graphene Through Surface Preparation 36
2.4 Summary & Prospects 53

3 Uniform Atomic Layer Deposition of Al_2O_3 on Graphene by Reversible Hydrogen Plasma Functionalization **65**

3.1 Introduction 66
3.2 Methodology 68
3.3 Results and Discussion 70
3.4 Conclusions 88
3.5 Appendix A 89
3.6 Appendix B 91

4 Area-Selective Atomic Layer Deposition of Platinum Using Photosensitive Polyimide **97**

4.1 Introduction 98
4.2 Methods 99
4.3 Results and Discussion 100
4.4 Conclusions 107
4.5 Appendix A 108
4.6 Appendix B 110
4.7 Appendix C 111
4.8 Appendix D 112

5 Pt-Graphene Contacts Fabricated by Plasma Functionalization and Atomic Layer Deposition **117**

5.1 Introduction 118
5.2 Methods 120
5.3 Results & Discussion 123
5.4 Conclusions 144

6 Conclusion & Outlook **153**

6.1 Conclusions 153
6.2 Outlook 155

Summary **159**

Contributions of the Author **161**

List of Publications **162**

Acknowledgements **165**

Curriculum Vitae **167**

Chapter 1

General Introduction

For over 50 years the advancement in the field of micro-electronics has mainly been driven by the continuous shrinking of the silicon field effect transistor (FET), the fundamental building block of integrated circuits (Figure 1.1a). By decreasing the transistor dimensions more can be fitted on the same microchip, reducing the cost and power consumption per transistor, while at the same time improving its speed. The resulting increase in computational power at a reduced cost has not only made the introduction of the internet, and the development of a wide range of electronic devices such as computers, mobile phones, etc. possible, but also made them affordable for everyone. This digital revolution has greatly changed our daily life and social organization and led to what is currently known as the information age [1].

Since 1965 the amount of transistors per area has roughly doubled every 18-24 months. This regularity was first observed by Gordon Moore and is commonly known today as 'Moore's Law' [2]. The semiconductor industry has used Moore's Law ever since as a guide for the further development of the integrated circuits and the further downscaling of its basic element the silicon FET [3]. Initially, down-scaling was purely obtained by improvements in lithographic processing, also known as lithography enabled scaling, while the materials used to fabricate the transistor remained mostly the same. However, to meet the increasing scaling demands different materials have been

introduced in Si FET fabrication since 2003, for example the use of high-κ materials as the gate dielectric (Figure 1.1b) [4,5]. Despite the introduction of new materials and device designs, silicon has always been the channel material of choice. The fundamental limits of silicon are however, being approached. In the end the minimum silicon channel size is limited to ~ 8 nm [3,6]. At this dimension quantum confinement effects start play a role in the device performance, increasing device to device variation and deteriorating carrier transport properties. Currently, the introduction of the 7 nm node[1] is expected in 2024, and although there are many promising candidates available it is still unclear which material will ultimately replace silicon [3].

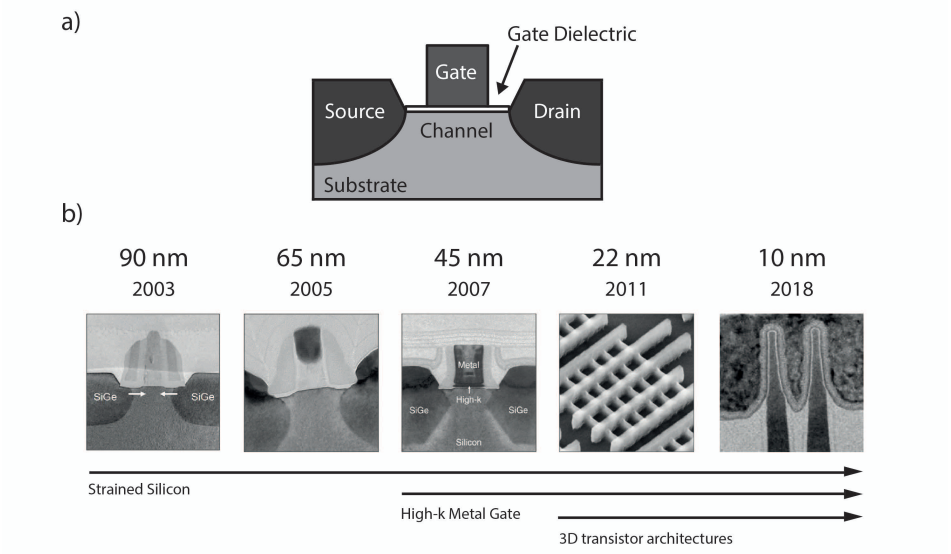


Figure 1.1: a) schematic illustration of the traditional metal-oxide-semiconductor field effect transistor (MOSFET). The MOSFET consist of a semiconducting channel connected to a metal source and drain. The current from source to drain can be controlled by a metal gate separated from the channel by a dielectric. Depending on the voltage applied to the gate the charge carrier density in the channel changes. This allows for control of the current flowing through the channel from source to drain, and makes it possible to switch the transistor on and off. b) Development of the transistor in integrated circuits, and the innovations implemented by Intel to keep up with Moore's law [4,5].

[1] Here it is assumed that the channel length is approximately equal to the node size. While this used to be true for past technology nodes (> 32 nm), due to short channel effects, such as drain induced barrier lowering, the channel length can no longer be scaled as aggressively. The channel length for the current technology nodes is larger than the node size, the 14 nm node, for example, uses a channel ~ 22 nm long [20]. This further illustrates that the limits of silicon as a channel material are being approached.

1.1 Graphene for Future Nano-electronic Applications

One group of materials that has received considerable attention in recent years as a future replacement for silicon in FETs and other device structures are the 2D-nanomaterials. In these layered materials the charge carriers are naturally confined in plane, a result of the weak van der Waals interaction between the nanomaterial and its surroundings [7]. The 2D-nanomaterials are therefore often classified as van der Waals materials. This weak interaction also makes it possible to isolate single layers of these materials, often just one atomic layer thick. The intrinsic monolayer thickness of the 2D-nanomaterials makes them a promising option to meet the scaling demands required for the future technology nodes.

The interest in 2D-nanomaterials was sparked by the discovery of graphene and the study of its properties by Novoselov *et al.* in 2004 [8]. Graphene is a single atomic layer of carbon atoms arranged in a hexagonal pattern, schematically displayed in Figure 1.2. Graphene proved to be a very interesting material due to its unique properties. Amongst others, it is the thinnest material discovered to date (only 3.35 Å thick), it has a record high charge carrier mobility (above of 200.000 $cm^{2/}Vs$), it is extremely flexible and stretchable, it is transparent over a wide spectral range (30 μm – 280 nm) with an absorption coefficient of only 2.3%, it has a high saturation current density (10^6 times higher than copper) and has a high thermal conductivity (similar to that of diamond) [9,10].

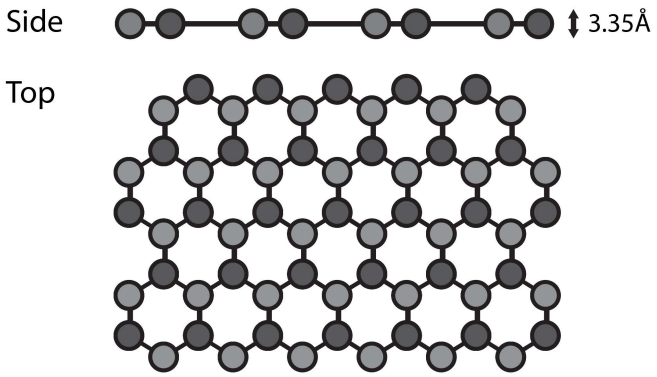


Figure 1.2: Schematic representation of graphene, side and top view. The carbon atoms are displayed in gray scale and correspond to the two different atoms that make up the graphene unit cell. Graphene has no out-of-plane bonds, all bonds lie in-plane in a sp^2 carbon configuration

The unique properties of graphene attracted interest throughout the research community and elevated graphene's status to that of a true wonder material. Applications of graphene are envisioned in many areas: the high conductivity of graphene and its large surface area, for example, make it a promising material for batteries and energy storage applications [9], while its transparency, conductivity and flexibility make it an interesting material for flexible displays and touch screens [11]. Other applications include the use of graphene as a conductive ink, chemical sensor, barrier layer or heat spreader [9]. Yet, the initial interest in graphene, was sparked by its potential for post-silicon optical and electronic applications, due to its high intrinsic mobility, scalability and the observation of the electric field effect in graphene [3,8,12].

Graphene however, is a zero-bandgap material. This limits its applicability as a FET channel material as the on-off ratio of a graphene transistor is limited to ~30 while for logic operation an on-off ratio in the order of 10^4-10^7 is desired. Despite its lack of a bandgap, graphene might still be of interest for transistor logic. This is because a bandgap can be opened in graphene when it is cut in to ribbons of a few nm in width or by stacking two graphene layers on top of each other and applying a vertical electrical field [13]. Another option could be the design of a graphene transistor which does not rely on a bandgap for logic operation [13–15]. An example of graphene device not relying on a bandgap for switching is shown in Figure 1.3. The figure shows a schematic representation of a bilayer pseudospin FET (BiSFET). The BiSFET relies on the control of the tunneling current between two graphene layers separated by a very thin dielectric, to switch the device on and off. The BiSFET should be able to operate at extremely low voltages (< 25 mV), making it an extremely low power device compared to traditional FETs which have a typical operation range ~1 V. The promise of ultra-low power consumption has also earned the BiSFET a place on the 'International Technology Roadmap for Semiconductors' [16]. Unfortunately, the BiSFET has yet to be experimentally realized as currently only simulations of its predicted performance exist. Despite being not proven yet, the BiSFET shows that alternative FET configurations might make logic devices based on graphene possible.

The lack of a band-gap in graphene could mean that other 2D nanomaterials such as MoS_2 or other transition metal dichalcogenides (TMDs) prove more useful as a FET channel material, as they do possess a bandgap [3,13]. Despite that the mobility in these materials is not higher compared to Si, they offer advantages for scaling and flexible electronics. One of the device structures of particular interest in this case is the all 2D-FET (Figure 1.4), a FET consisting of only 2D materials [13,15]. The advantage of an all 2D transistor is that due to the weak interaction between the layers they do not suffer

from lattice mismatch problems between the layers, increasing the choice of possible device structures. Furthermore, due to this weak interaction, the interface of these materials is not disturbed and therefore the material retains its pristine properties, independent from which 2D-material is stacked on top. In an all 2D-FET, graphene could serve as the source, drain and gate contact, whereas MoS_2 could be used as a channel material and hexagonal BN (*h*-BN) as the gate dielectric. 2D-FETs have already been demonstrated experimentally and excellent on-off ratios (up to 10^8) and switching behavior (60 mV/ decade) have been reported in the literature [15].

Apart from logic operation FETs can also be used for radiofrequency applications, such as wireless communication networks. In radiofrequency FETs, the ability to switch off the device is not necessarily required (the device structure is similar to that shown in Figure 1.1, with graphene instead of Si as the channel material) [12]. The high intrinsic mobility of graphene combined with its 2D structure might make it a suitable channel material for a radiofrequency FETs. Radiofrequency graphene FETs are thoroughly investigated in literature, and although their current saturation behavior is still less than optimal they have shown to outperform silicon FETs even in low current saturation regimes [12].

No matter what will ultimately be the application of graphene, in the end it will always need to be connected to its 3D surroundings. Therefore it needs to be compatible with existing metal oxide semiconductor technology, in particular with respect to the formation of ohmic contacts to inject charges into the graphene and dielectric interfaces for electrostatic control. This thesis will focus on the deposition of metal oxides and metals on graphene. It is important that the properties of the graphene are not adversely effected by the deposition of the dielectric or metal. One therefore needs a deposition technique that is able to deposit high quality materials, with good thickness control on graphene that avoids damaging the graphene in the process. A deposition technique that might be able to meet these requirements is atomic layer deposition (ALD).

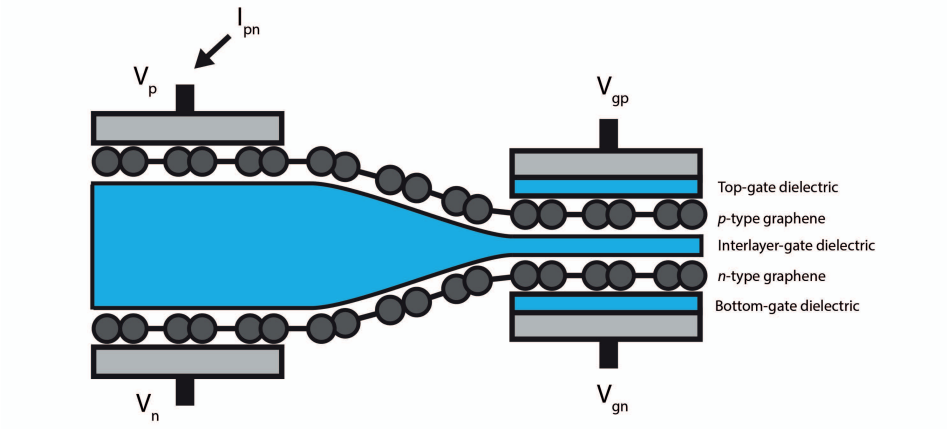


Figure 1.3: Schematic design of a graphene BiSFET. The BiSFET transistor can be turned on and off by controlling the tunneling current I_{pn}. The tunneling should occur in the right side of the device where the dielectric layer is thin enough for electrons and holes to tunnel through. Tunneling is controlled by applying two opposite voltages V_{gp} and V_{gn} this creates a *p*-type and *n*-type graphene layer. If the collective interaction between the holes and electrons on each side of the dielectric is strong enough these will bind into excitons. By applying a low voltage across the two terminals of the device V_{pn} $(V_p\text{-}V_n)$ a current will start to flow. At slightly higher voltages (still < 25 mV) the collective interaction between electros and holes is expected to collapse resulting in a blockage of all current flow.

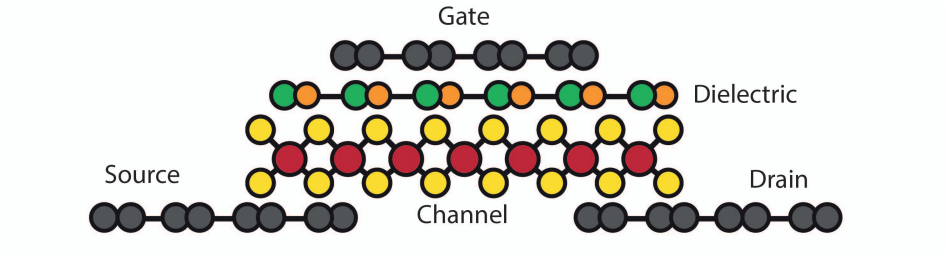


Figure 1.4: Schematic of an all 2D- FET where Graphene (grey) is used as a source/drain and gate material, MoS_2 (red/yellow) as the channel material and *h*-BN (green/orange) as the gate dielectric.

1.2 Atomic Layer Deposition

ALD is a chemical vapour deposition (CVD) technique that is able to deposit uniform layers over large areas with a precise control of the layer thickness, while at the same time achieving good step coverage or conformality. ALD was first introduced in the transistor fabrication process by Intel, for the deposition of the high-κ metal gate in 2007 [4]. Other application areas of ALD include the deposition of high-κ oxides and metals for DRAM capacitors, spacers for self-aligned double patterning (SADP) to enhance the feature density during photolithographic processing and passivation layers in solar cells [17]. The layers fabricated by ALD are generally of high quality and can often be deposited at lower temperatures when compared to other CVD techniques.

The ALD process is a cyclic process that consists of two self-limiting half reactions separated by pump and purge steps. The alternative pulsing and purging of reactants and co-reactants results in a self-limiting process that is independent of the precursor flux. To illustrate the self-limiting nature in more detail, the ALD process of Al_2O_3 will be used as an example (see Figure 1.5). The Al_2O_3 ALD process is well understood and is often considered a model system ALD process [17].

For the deposition of Al_2O_3 by ALD, trimethylaluminium ($Al(CH_3)_3$, TMA) is mostly used as the precursor molecule. The TMA adsorbs on reactive surface sites present on the substrate used (typically −OH groups for oxide materials). The TMA reacts with these surface groups forming an O-Al bond and releasing CH_4 in the gas phase. This process continues until the TMA has reacted with all available surface sites. Since the precursor molecules do not react with each other, nor with the newly created $-CH_3$ terminated surface the reaction stops (i.e. saturation of precursor adsorption is achieved). The reaction products, and excess TMA are removed from the system by a purge and/or pump step. In the second half cycle, a co-reactant H_2O is dosed in the system. The H_2O removes the CH_3 groups bonded to the Al through a ligand exchange mechanism resulting in the release of CH_4 and formation of –OH surface groups. This reaction stops once all CH_3 groups have been removed from the surface. The reaction products and excess H_2O are removed with a purge or pump step. The surface left behind after H_2O exposure is identical to the starting surface before TMA exposure. This makes it possible to repeat the process until the desired layer thickness is achieved. A sub-monolayer of material is deposited each cycle, which is about 1 Å in thickness for Al_2O_3 at 200 °C.

Similar to the Al_2O_3 ALD process, ALD processes of other materials often consist of a metalorganic complex that is used as the precursor and a reactive gas that is used as

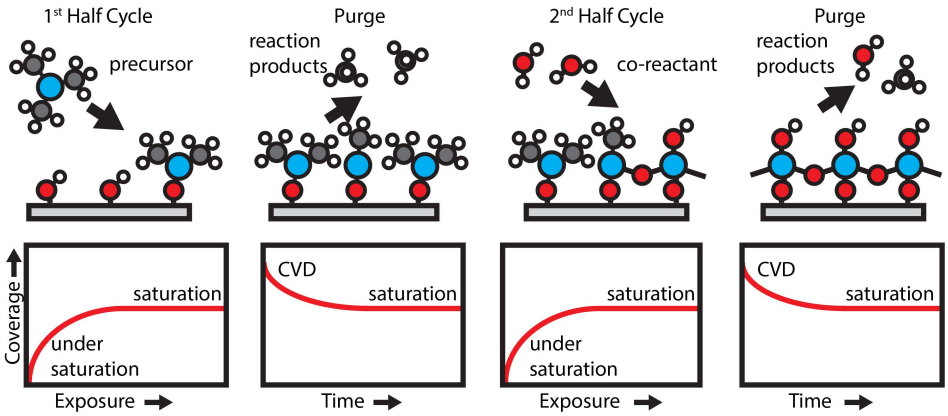


Figure 1.5: Schematic representation of the ALD process of Al_2O_3 consisting of two self-limiting half reactions. The reactants in the first half-cycle ($Al(CH_3)_3$ precursor exposure) and second half-cycle (H_2O co-reactant exposure) are self-limiting, i.e. the process stops once all available surface sites have reacted. The precursor and co-reactant dose are separated by pump or purge steps to prevent unwanted gas phase reactions between the precursor and co-reactant. At the end of the second half-cycle a surface is obtained identical to the starting surface of the first half cycle. This makes it possible to obtain the desired film thickness by repeating the half-cycles in an ABAB fashion. The resulting coverage, or growth per cycle (GPC), as a function of the exposure and purge time is indicated as well. Care should be taken that the exposure steps and purge steps are sufficiently long such that saturated growth is obtained and the reaction between the precursor and the co-reactant in the gas phase is prevented (CVD growth). Oxygen (red), Hydrogen (white), Aluminium (Blue) and Carbon (Gray).

the co-reactant. Depending on the material to be deposited this is often H_2O or O_2 plasma for metal oxides, NH_3 or N_2 plasma for metal nitrides and O_2 or H_2 plasma for metals. If only thermal energy is used to drive the surface reactions the ALD process is referred to as Thermal ALD. When additional energy is added to the co-reactant for example by creating a plasma, the term Plasma-ALD or Plasma-enhanced ALD (PEALD) is used. Plasma ALD is of interest when the material to be deposited cannot be grown by conventional thermal ALD, or when lower substrate temperatures are required, such as the deposition of SiO_2 on plastic substrates [18].

The cyclic nature of the ALD process makes it the ideal candidate for the deposition of thin dielectric and metal layers on graphene. However, as stated, ALD relies on the presence of reactive surface sites for the precursor molecules to adsorb on a surface. Graphene lacks these reactive sites due to its sp^2 carbon configuration. All bonds lie in plane and only a weak van der Waals interaction between the graphene and its surroundings exist. The ALD precursor molecules therefore have difficulty adsorbing

on the graphene plane as illustrated in **Figure 1.6**. Only on reactive surface sites such as defects, grain boundaries and wrinkles ALD growth is obtained. The lack of reactive surface sites on the graphene plane makes the initiation of ALD growth on graphene challenging.

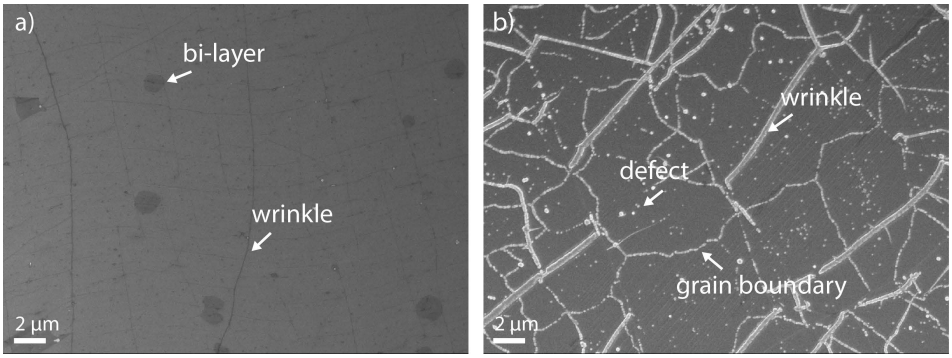


Figure 1.6: a) Scanning electron microscopy (SEM) image of graphene on a SiO_2 substrate. The bi-layers spots and wrinkles, which are a result of the graphene growth process are indicated as well. b) graphene after 100 cycles of Pt ALD. No uniform growth of Pt on the graphene plane is obtained, due to the absence of reactive surface sites. Only on reactive sites such as: defects, grain boundaries, and wrinkles Pt growth is obtained.

1.3 Research Objective, Framework & Outline

The properties of graphene make it a promising material for post silicon optical and electronic applications. As mentioned in Section 1.1, regardless of what will ultimately be the application of graphene, it needs to be connected to its 3D surroundings. Graphene therefore needs to be made compatible with existing semiconductor processing technology. Of particular importance for device integration are the creation of dielectric interfaces with the graphene for electrostatic control and the formation of metal-graphene contacts for the injection of charge carriers into the graphene. It is important that the intrinsic properties of graphene are not adversely affected by the creation of these interfaces and contacts. For the deposition of these layers ALD is the method of choice due to its ability to deposit high quality materials with sub-monolayer thickness control. Compared to other deposition techniques such as e-beam evaporation, sputtering, and pulsed laser deposition, thermal ALD also has the advantage that no highly reactive radicals, ions and photons are present during deposition. These reactive species can damage the graphene, deteriorating its electrical properties. However, as

stated in the Section 1.2, the initiation of uniform ALD growth on graphene is not straightforward.

Therefore the objective of the work described in this thesis is the development of ALD processes for the growth of thin uniform dielectric and metallic layers on graphene. This should be done with little or no impact on the graphene properties, which is essential for the integration of graphene in future optical and electronic devices.

1.3.1 Framework of the Project

The research presented in this thesis has been carried out within the Plasma & Materials Processing (PMP) group of the Eindhoven University of technology in the Netherlands. The PMP group has extensive experience in the areas of plasma-surface interaction, and the deposition of nanolayers, especially by (plasma-enhanced) ALD & CVD.

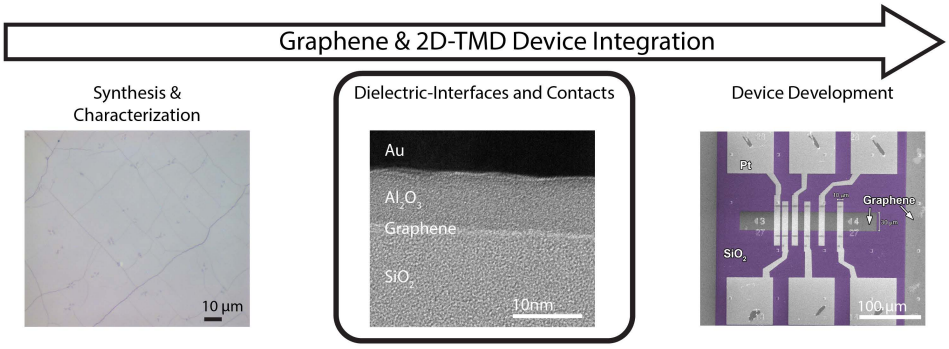


Figure 1.7: Schematic illustrating several steps required for the device integration of graphene and 2D-TMDs. The focus of this thesis lies on the creation of dielectric interfaces and metal contacts on graphene by ALD.

Within PMP, work is being performed on several different aspects required for the device integration of graphene and 2D-TMDs, see Figure 1.7. The ability to synthesize high-quality large-area 2D materials, and the development of characterization techniques can be considered the first step in this process. The initial work concerning graphene within PMP focused on the synthesis of graphene by CVD on Cu and the analysis of its properties [19]. The most important parameters of the graphene grown at PMP are shown in Figure 1.8.

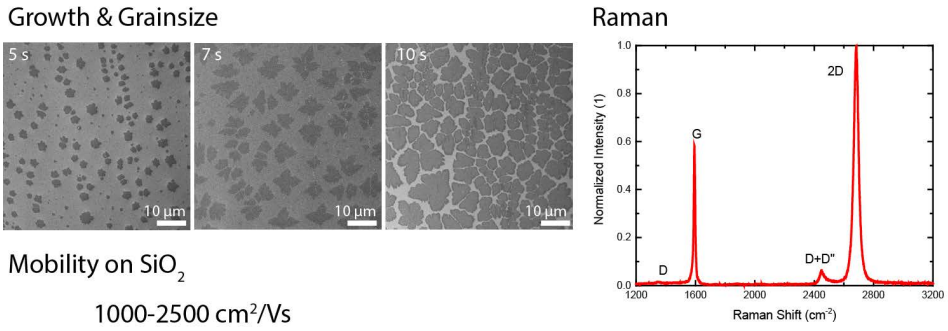


Figure 1.8: Overview of the properties of the graphene grown at PMP. From the SEM images of the initial stages of graphene growth the grainsize can be estimated to be ~ 5-10 µm. The Raman spectrum shows the characteristics of high quality graphene: a narrow 2D and G peak and a low defect peak (D). The mobility of the graphene ranges between 1000-2500 cm^2/Vs, comparable to results found in literature for graphene synthesized on Cu by CVD [19].

The establishment of graphene growth served as an excellent starting point for the formation of dielectric-interfaces and metal contacts to graphene, which is presented in this dissertation. The dissertation is part of a project of the Foundation for Fundamental Research on Matter (FOM), entitled: 'A physical-analytical approach to atomic layer deposition of ultra-thin high-κ dielectrics on graphene'. The aim is the fabrication of ultrathin (< 10 nm), uniform, pinhole free metals and metal-oxides on graphene by ALD, for the creation of dielectric interfaces and metal contacts to graphene. A combination of experimental work and theoretical simulations is used to develop ALD processes and study the underlying reaction mechanisms.

With the creation of contacts and dielectric interfaces to graphene in place, the next step is the synthesis and development of device architectures and the analysis of their performance. Within PMP this work is continued through a NWO-VIDI grant that explores the development of new fabrication techniques for carbon nano-electronics and an ERC Consolidator grant which focusses on the synthesis of 2D-TMDs by ALD, and the fabrication of devices similar to the one illustrated in Figure 1.4.

1.3.2 Outline

To obtain uniform growth by ALD on graphene, and to overcome the nucleation issues illustrated in Section 1.2 several different surface preparation techniques to initialize ALD on graphene have been explored and reported in the literature. In **Chapter 2** an overview of the different methods to achieve uniform deposition of ALD on graphene reported to date is presented. The advantages and disadvantages of each

method are discussed from the perspective of ALD. Special emphasis is given to the recent advancements in the understanding of the ALD process conditions and their influence on the deposition uniformity on graphene.

Among the functionalization methods, the creation of ALD precursor adsorption sites, through plasma functionalization shows promise. This is because of its processing ease, compatibility with silicon technology and limited amount of extra processing steps required. However, when O_2 or N_2 plasmas are used for functionalization, the sp^2 backbone of graphene is damaged, deteriorating its electrical properties, such as the charge carrier mobility. To prevent the deterioration of the graphene after plasma treatment and ALD, a new method to grow dielectrics on graphene based on reversible H_2 plasma treatments is introduced in **Chapter 3**. Al_2O_3 films are grown by ALD on H_2 plasma functionalized graphene resulting in the uniform deposition of Al_2O_3 on graphene. Hall measurements and Raman spectroscopy reveal that the hydrogen plasma functionalization is reversible upon Al_2O_3 ALD and does not deteriorate the graphene charge carrier mobility. To get insight into the underlying reaction mechanisms that play a role in the adsorption of the ALD precursor molecules on pristine and plasma treated graphene density functional theory (DFT) calculations are used.

The use of plasma treatments to initialize ALD growth of graphene could also be suitable for the fabrication of metal-graphene contacts. To fabricate these contacts by ALD, the selective deposition of the contact metal is preferred. To achieve area-selective ALD (AS-ALD), polymers or self-assembled monolayers can be used as blocking layers. The temperature stability of the polymers and SAMs is unfortunately too low to create well defined metal contacts using the typical metal ALD processes. Therefore a method to achieve AS-ALD of Pt using photosensitive polyimide has been developed and is presented in **Chapter 4**. Compared to other polymers, polyimide has a much higher temperature stability. This allows for the selective ALD deposition of Pt on the desired regions of the substrate, with improved uniformity of the Pt deposits and superior definition of the Pt patterns compared to the more commonly used poly(methyl-methacrylate) resist.

The combination AS-ALD of Pt and H_2 and O_2 plasma treatments to initiate ALD growth of Pt on graphene for the fabrication of metal-graphene contacts is demonstrated in **Chapter 5**. The plasma treatment serves two purposes: (1) It makes the uniform ALD of Pt on graphene possible, through the creation of adsorption sites for the Pt ALD precursor molecules. (2) The created functional groups also aid in the injection and extraction of charge carriers from the metal to the graphene, changing the contact resistance. Improved contact resistances were measured compared to standard

evaporated Pt-graphene contacts. Furthermore, H_2 plasma functionalization resulted in better contact resistances than O_2 plasma functionalization. Most likely a result of a different edge termination of the graphene after a H_2 or O_2 plasma treatments (C-H vs. C=O).

A summary of the main findings along with the possible directions for further research will be given in **Chapter 6**

References

1. https://en.wikipedia.org/wiki/Information_Age.

2. Moore, G.E. (1965) Cramming more components onto integrated circuits. *Electronics*, **38**, 114–117.

3. Franklin, A.D. (2015) Nanomaterials in transistors: From high-performance to thin-film applications. *Science*, **349** (6249), aab2750-aab2750.

4. Standards-22nm-3d-tri-gate-transistors, www.intel.com.

5. Mistry, K. 10 nm technology leadership, www.intel.com

6. Haron, N.Z., and Hamdioui, S. (2008) Why is CMOS scaling coming to an END? *2008 3rd Int. Des. Test Work.*, 98–103.

7. Mas-Ballesté, R., Gómez-Navarro, C., Gómez-Herrero, J., and Zamora, F. (2011) 2D materials: to graphene and beyond. *Nanoscale*, **3** (1), 20–30.

8. Novoselov, K.S., Geim, A.K., Morozov, S. V., et al. (2004) Electric Field Effect in Atomically Thin Carbon Films. *Science*, **306** (5696), 666–669.

9. Ferrari, A.C., Bonaccorso, F., Fal'ko, V., et al. (2015) Science and technology roadmap for graphene, related two-dimensional crystals, and hybrid systems. *Nanoscale*, **7** (11), 4598–4810.

10. Geim, A.K., and Novoselov, K.S. (2007) The rise of graphene. *Nat. Mater.*, **6** (3), 183–191.

11. Bae, S., Kim, H., Lee, Y., et al. (2010) Roll-to-roll production of 30-inch graphene films for transparent electrodes. *Nat. Nanotechnol.*, **5** (8), 574–578.

12. Schwierz, F. (2010) Graphene transistors. *Nat. Nanotechnol.*, **5** (7), 487–496.

13. Lemme, M.C., Li, L., Palacios, T., and Schwierz, F. (2014) Two-dimensional materials for electronic applications. *MRS Bull.*, **39** (8), 711–718.

14. Banerjee, S., Register, L., Tutuc, E., et al. (2009) Bilayer PseudoSpin Field-Effect Transistor (BiSFET): A Proposed New Logic Device. *IEEE Electron Device Lett.*, **30** (2), 158–160.

15. Roy, T., Tosun, M., Kang, J.S., et al. (2014) Field-Effect Transistors Built from All Two-Dimensional Material Components. *ACS Nano*, **8** (6), 6259–6264.

16. International Technology Roadmap for Semiconductors, Emerging Research Devices, http://www.itrs.net.

17. Pakkala, A., and Putkonen, M. (2010) Atomic Layer Deposition, in *Handbook of Deposition Technologies for Films and Coatings*, Elsevier, pp. 364–391.

18. Profijt, H.B., Potts, S.E., van de Sanden, M.C.M., and Kessels, W.M.M. (2011) Plasma-Assisted Atomic Layer Deposition: Basics, Opportunities, and Challenges. *J. Vac. Sci. Technol. A Vacuum, Surfaces, Film.*, **29** (5), 50801.

19. Weber, J.-W. (2015) Graphene an optical diagnostic study.

20. Moroz, V. (2011) Transition from Planar MOSFETs to FinFETs and its Impact on Design and Variability.

Chapter 2

Atomic Layer Deposition for Graphene Device Integration*

Abstract

Graphene is a two dimensional material with extraordinary properties, which make it an interesting material for many optical and electronic devices. The integration of graphene in these devices often requires the deposition of thin dielectric layers on top of graphene. Atomic layer deposition (ALD) is the method of choice to deposit these layers due to its ability to deposit ultra-thin, high quality films with sub-monolayer thickness control. ALD on graphene however, is a challenge due to the lack of reactive surface sites on graphene. This leads to the selective growth on grain boundaries, wrinkles and defect sites present in the graphene.

In this review an overview of the different methods to achieve uniform deposition of ALD on graphene is presented. The advantages and disadvantages of each method are discussed from the perspective of ALD together with the opportunities for further research. Special emphasis is given to the recent advancements in the understanding of the ALD process conditions and their influence on the deposition uniformity on graphene. Particularly, improving the quality of the dielectric layers deposited by ALD while maintaining the pristine properties of graphene, will prove vital for the device integration of graphene.

*R.H.J. Vervuurt, W.M.M. Kessels & A.A. Bol, *Advanced Materials Interfaces* (2017) 1700232.

2.1 Introduction

Graphene is a two-dimensional material with extraordinary properties, that has gathered considerable interest of the research community over the past few years [1]. The high charge carrier mobility of graphene combined with its good thermal conductivity, large maximum current density and the ability to absorb light over a broad spectral range make it a promising material for post-silicon electronic and optical applications [2–4]. Device integration often requires the ability to deposit ultra-thin (< 10 nm) uniform high-κ dielectric layers on graphene. The high charge carrier and large maximum current density of graphene for example, make it a suitable channel material for graphene transistors where the zero band-gap of graphene is not a fundamental limitation [3]. To make top-gated radio-frequency graphene transistors the deposition of a high-κ dielectric layer on top of graphene is required for good electrostatic control of the channel, which increases device performance and improves device reliability [5,6]. The integration of graphene in lateral spin valves requires the deposition of ultra-thin dielectrics on the graphene to realize electrical spin injection [7,8], whereas for bilayer pseudospin transistors (BiSFETs) the deposition of thin dielectrics on graphene (acting as a tunnel barrier) is essential [9–11].

This review discusses the deposition of such ultra-thin dielectric layers on graphene by atomic layer deposition (ALD). ALD is a chemical vapor deposition (CVD) technique consisting of two self-limiting surface reactions, or half-cycles, in which the growth substrate is exposed to alternating pulses of precursor and co-reactant. These pulses are separated by pump or purge steps (Figure 2.1) [12]. Each ALD cycle a (sub)monolayer of material is deposited. The cyclic nature of the ALD process makes it possible to deposit high quality materials uniformly distributed over large areas, with precise control of the layer thickness. Apart from these benefits, ALD has an additional advantage for the deposition of dielectric materials on graphene compared to other deposition methods. The commonly used physical vapor deposition (PVD) techniques such as sputtering, pulsed laser deposition and e-beam evaporation easily damage the graphene during deposition, resulting in a reduction of the graphene charge carrier mobility that reduces device performance [13]. This damage can be avoided when thermal ALD is used. This is because the absence of energetic species and reactive species, such as ions and radicals during thermal ALD [12].

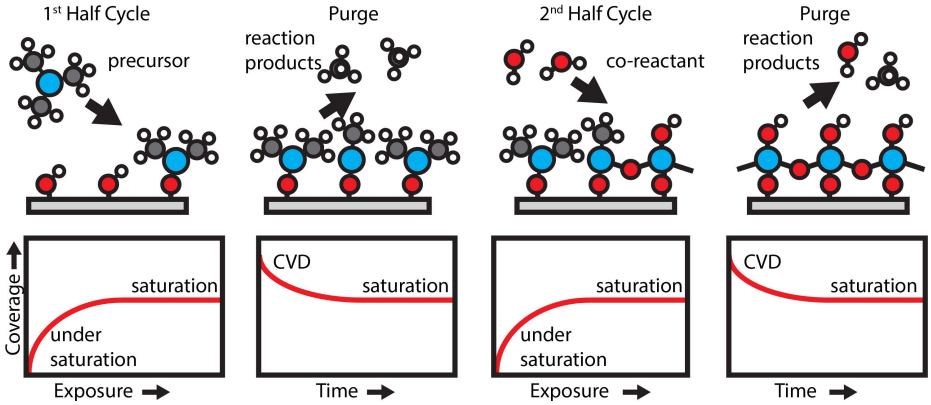


Figure 2.1: Schematic representation of an ALD process cycle, which consist of two half reactions. The reactants in the first half-cycle (precursor exposure) and second half-cycle (co-reactant exposure) are self-limiting, i.e. the process stops once all available surface sites have reacted. The precursor and co-reactant dose are separated by pump or purge steps to prevent unwanted gas phase reactions between the precursor and co-reactant. At the end of the second half-cycle a surface is obtained identical to the starting surface of the first half cycle. This makes it possible to obtain the desired film thickness by repeating the half-cycles in an ABAB fashion. The resulting coverage, or growth per cycle (GPC), as a function of the exposure and purge time is indicated as well. Care should be taken that the exposure steps and purge steps are sufficiently long such that saturated growth is obtained and the reaction between the precursor and the co-reactant in the gas phase is prevented (CVD growth).

The initiation of ALD growth on graphene however, is known to be a challenge [14]. This is because graphene consists of pure sp^2 bonded carbon and therefore lacks out-of-plane bonds or surface groups needed for the initiation of ALD growth [15,16]. To overcome these nucleation issues several different surface preparation techniques to initialize ALD on graphene have been explored over the years. Apart from the many articles published, several review papers discussing the possibilities these techniques offer for the uniform ALD of dielectrics on graphene have appeared [17–20], the most recent being from 2013. Most available reviews focus on ALD for carbon nanoelectronics in general and are device oriented [17,19,20]. So far a review focusing on the field from an ALD processing perspective has not appeared. Furthermore, since 2013, significant advances have been made in the field, especially in the understanding of the ALD process conditions and their influence on the deposition uniformity [21,22]. Also a shift in the type of graphene used has occurred. Initially, most of the work studying the growth of dielectrics by ALD on graphene focused on using exfoliated graphene flakes or highly ordered pyrolytic graphite (HOPG) as a substrate material

[14,23,24]. This was because these materials were readily available when graphene first attracted the interest of the research community and did not require additional experience in the synthesis of graphene. Only later when first epitaxial graphene and later CVD graphene became more commonly available, ALD was attempted on these graphene types [25,26]. For electronic and optical applications these last two are of significantly larger interest due to their scalability, but the work done on both exfoliated flakes and HOPG has served as an excellent starting point to better understand the nucleation of ALD growth on graphene.

ALD has also been performed on graphene which is synthesized by other methods than the ones mentioned above [27]. For example ALD was used on graphene nano-sheets or reduced graphene oxide (rGO), synthesized by chemical exfoliation [28]. Although these graphene types are of interest for electrochemical applications, the quality is too low for high end optical and electronic applications. Furthermore because the graphene created by these methods is defective and contains many functional surface groups or edges, ALD is relatively straightforward on these graphene types [28–30]. For this reason, these graphene types are not considered here unless these are used as a nucleation layer on high quality graphene to initiate ALD growth.

In this review paper, an overview of the different methods to achieve uniform deposition of ALD on graphene reported to date is presented. The advantages and disadvantages of each method are discussed from the perspective of ALD. Special emphasis is given to the recent advancements in the understanding of the ALD process conditions and their influence on the deposition uniformity on graphene. First the direct ALD of dielectrics on pristine (untreated) graphene is discussed in Section 2.2. In this section the influence of the graphene synthesis method on the ALD growth behavior is discussed, together with the influence of the ALD process parameters and the underlying substrate on the ability to deposit uniform ALD layers on graphene. Section 2.3 provides an overview of the different surface preparation techniques that can be used to initiate ALD growth on graphene; 1) the use of polymer seed-layers to initialize ALD growth, 2) the use of evaporated seed-layers and 3) the creation of functional groups on the graphene surface by plasma and ozone treatments. The review will end with a perspective for further research in Section 2.4.

2.2 ALD on Pristine Graphene

ALD on pristine graphene and HOPG is a challenge due to the lack of reactive surface sites or functional groups on graphene. As a result ALD on pristine graphene

often leads to non-uniform film coverage or even the absence of film growth (Figure 2.2) [14–21]. However, for graphene device integration the deposition of uniform layers on graphene is essential. Therefore approaches to carry out ALD of dielectric materials on graphene have been investigated thoroughly in literature since the discovery of its outstanding electronic properties by Geim and Noveselov in 2004 [31]. An overview of the literature investigating the ALD of dielectric materials grown on graphene is given in Table 1. The table provides a full overview of reports addressing ALD growth on HOPG, exfoliated graphene, epitaxial graphene and CVD graphene published until recently (February 2017). Also indicated in the table are the type of functionalization used to achieve (uniform) growth, the underlying substrate, temperature of the ALD process, minimum thickness for which a closed dielectric layer was reported and whether the graphene was damaged during the functionalization process or subsequent ALD deposition. It should be noted that almost all processes listed used a metal organic precursor combined with H_2O as the co-reactant. Only in a few cases the co-reactant was different, namely NO_2, O_3 or an O_2 plasma, indicated by an * in the table. This is because these alternative co-reactants can easily damage the graphene, unless special precautions are taken. This will be discussed in Section 2.3.

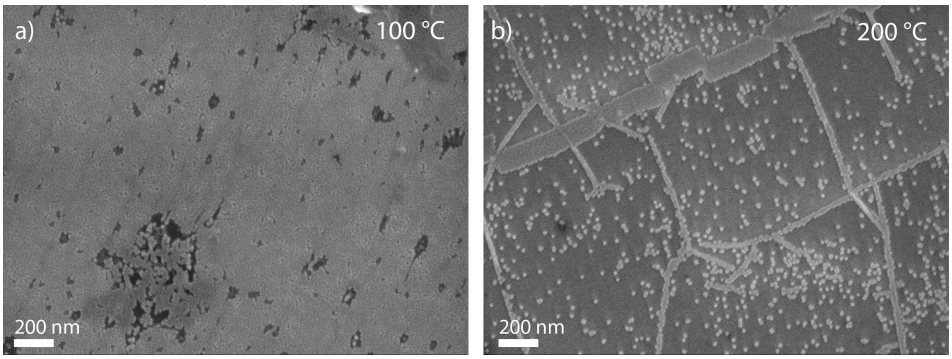


Figure 2.2: Scanning electron microscope (SEM) image of CVD graphene, transferred to a SiO_2 substrate, after 100 cycles of Al_2O_3 ALD. The Al_2O_3 was deposited at a) 100 °C and b) 200 °C. At 100°C pinholes are observed throughout the Al_2O_3 layer. At 200 °C the deposition becomes more selective towards the wrinkles, defects and grain boundaries of the graphene. The difference in nucleation density can be explained by the larger amount of physisorbed H_2O being present on the graphene at lower deposition temperatures. Adapted from Vervuurt *et al*. Copyright (2017) American Chemical Society [32].

Table 1: Overview of the literature that has appeared on ALD of dielectric materials on to graphene until February 2017. The different types of sp^2 materials considered are HOPG, exfoliated graphene, CVD graphene and epitaxial graphene. Listed are the type of functionalization used to achieve uniform growth, the dielectric material deposited, the graphene synthesis method, the substrate material, temperature of the ALD process, minimum thickness for which a closed layer is obtained and whether the graphene was damaged by the functionalization/ALD process. An * indicates that during the ALD process the H_2O as co-reactant is replaced by either NO_2, O_3 or O_2 plasma. A '-' means not known.

Functionalization	**Dielectric**	***sp²* Carbon Material**	**Substrate**	***T* (°C)**	**Thickness (nm)**	**Graphene Damage**	**Refs.**
None	Al_2O_3	HOPG	HOPG	RT-350	Not closed	-	[22–26]
	Al_2O_3	Exfoliated Graphene	SiO_2	100-200	Not closed	No	[14,33]
	Al_2O_3	CVD Graphene	SiO_2	80-200	Not closed	No	[26,34]
	Al_2O_3	CVD Graphene	Cu	80;200	10 (80°C)	No	[26]
	Al_2O_3	CVD Graphene	SiO_2	150	Not closed	Yes	[35]
	Al_2O_3	CVD Graphene	Ni-Au	80	10	No	[26]
	Al_2O_3	Epitaxial Graphene	SiC	200-350	Not closed	No	[25]
	HfO_2	HOPG	HOPG	200-300	Not closed	-	[23]
	HfO_2	Exfoliated Graphene	SiO_2	250	Not closed	-	[21]
	HfO_2	Exfoliated Graphene	SiO_2	110	30	No	[36]
	HfO_2	Exfoliated Graphene	SiO_2	90	5	No	[37]
	HfO_2	CVD Graphene	SiO_2	250	Not closed	No	[21]
	HfO_2	Epitaxial Graphene	SiC	110	>25	No	[38]
	ZnO	CVD Graphene	SiO_2	300	Not closed	No	[39]
	ZrO_2	CVD Graphene	QCM Sensor	190	-	Yes	[40]
Long precursor dose	Al_2O_3	HOPG	HOPG	200	Not closed	-	[22]
	Al_2O_3	CVD Graphene	SiO_2	200	Not closed	No	[22]
	Al_2O_3	CVD Graphene	Ge	200	Not closed	No	[22]
	Al_2O_3	CVD Graphene	Cu	200	1.2	No	[22]
	Al_2O_3	CVD Graphene	Al_2O_3	100:250	22	No	[41]
No purge steps	Al_2O_3	CVD Graphene	SiO_2	100	10	No	[42]

Functionalization	Dielectric	sp^2 Carbon Material	Substrate	T (°C)	Thickness (nm)	Graphene Damage	Refs.
SAM (PTCA)	Al_2O_3	Exfoliated Graphene	SiO_2	100	2.8 excluding SAM	-	[14]
	ZnO	CVD Graphene	SiO_2	120	60 excluding SAM	No	[43]
SAM (PTCDA)	Al_2O_3	Exfoliated Graphene	SiO_2	150	10	No	[6]
	Al_2O_3	Epitaxial Graphene	SiC	100	3	-	[44]
	Al_2O_3	Epitaxial Graphene	SiC	150	10	-	[6]
	HfO_2	Epitaxial Graphene	SiC	100	3	-	[44]
	HfO_2	Epitaxial Graphene	SiC	150	10	-	[6]
SAM (FDTS)	HfO_2	CVD Graphene	SiO_2	400	10	No	[45]
SAM (4MP)	ZnO	Exfoliated Graphene	SiO_2	80	2 excluding SAM	No	[46]
SAM (HMDS)	Al_2O_3	CVD Graphene	SiO_2	125	Not closed	No	[47]
SAM (HMDS) + Air Exposure	Al_2O_3	CVD Graphene	SiO_2	125	Not closed	No	[47]
SAM (TiOPc)	Al_2O_3	HOPG	SiO_2	100	4	-	[48]
	Al_2O_3	CVD Graphene	SiO_2	100	4	-	[48]
Polymer (PVP)	Al_2O_3	CVD Graphene	SiO_2	-	25 including polymer (5)	No	[5]
Polymer (NFC 1400-3CP)	HfO_2	Exfoliated Graphene	SiO_2	125	20 including polymer (10)	No	[49]
	HfO_2	Exfoliated Graphene	SiO_2	200	19 including polymer (9)	-	[2]
	HfO_2	Epitaxial Graphene	SiC	-	10 excluding polymer	No	[50]
Polymer (NMP)	HfO_2	CVD Graphene	SiO_2	200	Not closed	No	[51]
Polymer (PVA) + O_3	HfO_2	Exfoliated Graphene	SiO_2	150	7.5 including polymer (2.5)	-	[52]
Al e-beam	Al_2O_3	HOPG	HOPG	200	-	-	[53]
	Al_2O_3	Exfoliated Graphene	SiO_2	-	15	-	[10]
	Al_2O_3	Exfoliated	SiO_2	-	25	-	[54]

Functionalization	Dielectric	sp^2 Carbon Material	Substrate	*T* (°C)	Thickness (nm)	Graphene Damage	Refs.
		Graphene					
	Al_2O_3	Exfoliated Graphene	SiO_2	250	10	-	[55]
	Al_2O_3	CVD Graphene	SiO_2	150	90	No	[56]
	Al_2O_3	Epitaxial Graphene	SiC	300	30 excluding seed-layer (1)	No	[57]
	Al_2O_3	Epitaxial Graphene	SiC	120	27 including seed-layer (3)	-	[58]
	Al_2O_3	Epitaxial Graphene	SiC	300	~ 20	Yes	[59]
	HfO_2	Exfoliated Graphene	SiO_2	200	1.5 evaporated layer thickness	Yes	[60]
	HfO_2	Exfoliated Graphene	SiO_2	200	10	Yes	[49]
Ti e-beam	Al_2O_3	Exfoliated Graphene	SiO_2	250	2.6	-	[55]
	Al_2O_3	Epitaxial Graphene	SiC	300	~ 20	Yes	[38]
	TiO_2	Epitaxial Graphene	SiC	150;300	~ 20	No	[38]
Hf e-beam	HfO_2	HOPG	HOPG	200	-	-	[53]
	HfO_2	CVD Graphene	SiO_2	200	18.7 including seed-layer (3)	Yes	[51]
	HfO_2	Epitaxial Graphene	SiC	110	~ 20	No	[38]
Ta e-beam	Ta_2O_5	Epitaxial Graphene	SiC	120;250	~ 20	Yes	[38]
SiO_2 e-beam	Al_2O_3	CVD Graphene	SiO_2	-	20 including seed-layer (5)	Yes	[61]
	HfO_2	Epitaxial Graphene	SiC	250	12 including seed-layer (2)	Yes	[59]
Al_2O_3 e-beam	Al_2O_3	Epitaxial Graphene	SiC	300	10 including seed-layer (2)	No	[59]
	HfO_2	Epitaxial Graphene	SiC	250	10 including seed-layer (2)	No	[59]
HfO_2 e-beam	Al_2O_3	Epitaxial Graphene	SiC	300	10 including	No	[59]

Functionalization	Dielectric	sp^2 Carbon Material	Substrate	T (°C)	Thickness (nm)	Graphene Damage	Refs.
					seed-layer (2)		
	HfO_2	Epitaxial Graphene	SiC	250	10 including seed-layer (2)	No	[59]
Sputtered ZnO	HfO_2	CVD Graphene	SiO_2	200	17.1 including seed-layer (3)	Yes	[51]
O_3	Al_2O_3*	HOPG	HOPG	200	10	-	[24]
	Al_2O_3*	HOPG	HOPG	200	20	No	[62]
	Al_2O_3*	HOPG	HOPG	30; 200	Not closed	-	[63]
	Al_2O_3	HOPG	HOPG	225	Not closed	Yes	[64]
	Al_2O_3*	HOPG	HOPG	30; 200	Not closed	-	[65]
	Al_2O_3*	HOPG	HOPG	200-350	50	-	[25]
	Al_2O_3*	Exfoliated Graphene	SiO_2	25; 200	15	Temperature dependent	[66]
	Al_2O_3	Exfoliated Graphene	SiO_2	25; 150	4.5	Temperature dependent	[67]
	Al_2O_3*	CVD Graphene	Ni	80	0.6	No	[8]
	Al_2O_3	CVD Graphene	SiO_2	80;120	90	No	[68]
	Al_2O_3	Epitaxial Graphene	SiC	200-350	50	Yes	[25]
NO_2	Al_2O_3*	HOPG	HOPG	150	3	-	[69]
	Al_2O_3*	Exfoliated Graphene	SiO_2	250	12	Yes	[70]
	Al_2O_3*	Exfoliated Graphene	SiO_2	25; 225	30	-	[71]
	Al_2O_3*	Exfoliated Graphene	Free standing	180	2.8	-	[72]
	HfO_2*	Exfoliated Graphene	SiO_2	200	10	Yes	[49]
N_2 plasma	Al_2O_3	CVD Graphene	SiO_2	-	28	Yes	[73]
O_2 plasma	Al_2O_3*	CVD Graphene	SiO_2	100	9	Yes	[74]
	Al_2O_3*	CVD Graphene	SiO_2	250	5.5	Yes	[75]
	Al_2O_3	CVD Graphene	SiO_2	250	-	-	[76]
	Al_2O_3	CVD Graphene	SiO_2	150	4	No	[77]
	HfO_2	CVD Graphene	SiO_2	250	-	-	[76]

Functionalization	Dielectric	sp^2 Carbon Material	Substrate	*T* (°C)	Thickness (nm)	Graphene Damage	Refs.
	HfO_2*	CVD Graphene	SiO_2	250	5.9	Yes	[75]
H_2 plasma	Al_2O_3	CVD Graphene	SiO_2	100	8	No	[32]
GO	Al_2O_3	CVD Graphene	SiO_2	-	20	No	[78]
	Al_2O_3	Epitaxial Graphene	SiC	280	4 excluding GO (1.5)	No	[79]
	HfO_2	Epitaxial Graphene	SiC	175	4 excluding GO (1.5)	No	[79]
	TiO_2	Epitaxial Graphene	SiC	300	6 excluding GO (1.5)	No	[79]
Atomic oxygen	ZnO*	Epitaxial Graphene	SiC	25;100	Not closed	No	[80]
XeF_2	Al_2O_3	Epitaxial Graphene	SiC	225	15	No	[81]
H_2O soaking	Al_2O_3	Exfoliated Graphene	SiO_2	200	10	No	[33]
	Al_2O_3	CVD Graphene	SiO_2	200	10	No	[33]
H_2O pulsing	Al_2O_3	CVD Graphene	SiO_2	100	9	No	[82,83]
	Al_2O_3	CVD Graphene	SiO_2	120	90	No	[68]
	HfO_2	CVD Graphene	SiO_2	100	9	No	[83]
	ZnO	CVD Graphene	Cu	100	>10	No	[84]
Wet chemistry	Al_2O_3	Epitaxial Graphene	SiC	200	~ 25	No	[85]
Air exposure	Al_2O_3	CVD Graphene	SiO_2	125	Not closed	No	[47]

SAM: self-assembled monolayer, PTCA: 3,4,9,10-perylene tetracarboxylic acid, PTCDA: perylene-3,4,9,10-tetracarboxylic dianhydride, TiOPc: titanyl phthalocyanine, NFC 1400-3CP: polyhydroxystyrene derivative, 4MP: 4-mercaptophenol, GO: graphene oxide and FDTS: perfluorodecyltrichlorosilane, PVP: poly(4-vinylphenol), PVA: poly(vinyl alcohol), NMP: N-methyl-2-pyrrolidone and HDMS: hexamethyldisilazane

H_2O-based ALD processes on HOPG and graphene result most of the time in the preferential growth of the material on the defects sites, grain boundaries and wrinkles present in the graphene, as illustrated in Figure 2.2 for the deposition of Al_2O_3 on CVD graphene [32]. The preferential deposition on defect sites, grain boundaries and graphene wrinkles is a result of the lack of functionalized dangling bonds on the graphene basal plane. Only on defect sites and grain boundaries where functional

groups are present ALD nucleation is possible [14–16,23,24]. Density functional theory (DFT) calculations have shown that various ALD precursors tend to physisorb on the graphene basal plane [15,16,21]. Chemisorption of precursor molecules on the graphene is unlikely due to the high activation barriers, typically several eV, which makes ALD nucleation difficult. Grain boundaries on the other hand often contain heptagon-pentagon or octagon-pentagon units on which precursor chemisorption is possible (see Figure 2.3) [16]. The C-C bonds in these grain boundaries are strained making them more reactive towards ALD precursor adsorption. Similarly defect sites, for example mono and divacancies, are also more reactive as are defects containing epoxy or hydroxyl groups [16]. Wrinkles on the other hand do not contain additional defects or functional groups but consist of folded graphene layers. The C-C bonds present in these wrinkles are strained, which makes them more reactive [86,87]. Furthermore, photoresist residues left over from the graphene transfer process could gather at wrinkles, which could also act as a nucleation site for the subsequent ALD process. ALD growth therefore preferentially starts at defects, grain boundaries and wrinkles, whereas the pristine basal plane remains unreactive during ALD growth.

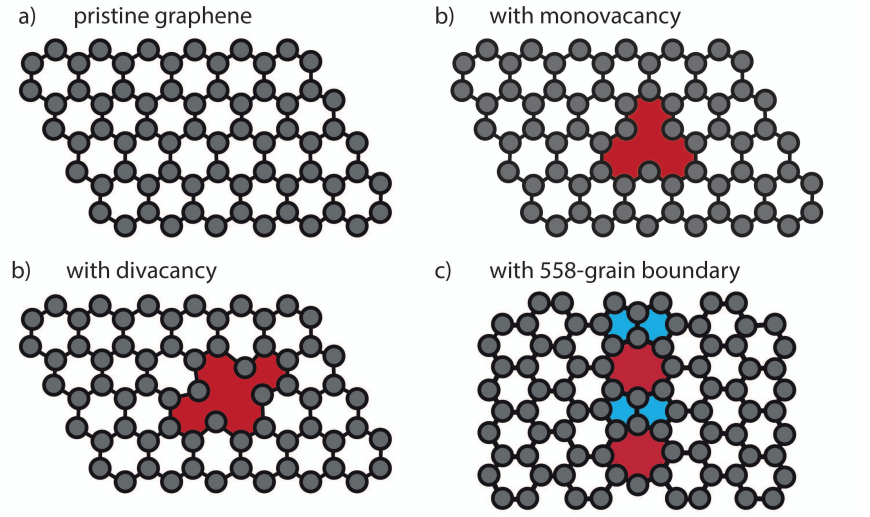


Figure 2.3: Top view of a) pristine graphene and b), c), d) typical graphene defects such as monovacancies, divacancies and grain boundaries. At the defects sites dangling bonds or other functional groups are present which enables the adsorption of ALD precursor molecules on these sites [16].

Experimentally non-uniform ALD growth is observed for all types of graphene; HOPG [22–26], exfoliated graphene [14,33], CVD graphene [26,34] and epitaxial graphene [25]. The selectivity of the ALD process towards the defect sites and grain

boundaries however, does depend on the type of graphene and on the ALD process conditions, such as substrate temperature, the type of precursor used and the precursor dose and purge times. Each of these aspects will be discussed in more detail in the following sections.

2.2.1 Influence of the Graphene Synthesis and Transfer Method

The synthesis method of the sp^2 carbon material is of importance for the ALD nucleation and can result in different nucleation behaviors being observed. Oh *et al.* showed that HfO_2 nucleates much faster on CVD graphene compared to exfoliated graphene, due to the higher amount of defects and wrinkles being present for CVD graphene [21]. Apart from the higher amount of defects, CVD graphene is typically also less clean compared to exfoliated graphene, which is a result of the CVD synthesis and transfer method. CVD graphene is typically grown on a metal substrate (Cu or Ni) and transferred to the desired substrate using poly(methyl methacrylate) (PMMA) as a support layer. It is difficult to fully remove the PMMA from the graphene surface, typically some residues are left behind [88]. These residues can enhance the nucleation of the ALD process on graphene, but blocking the ALD growth is also possible. The Pt ALD precursor methylcyclopentadienyltrimethyl-platinum ($MeCpPtMe_3$) for example does not nucleate on PMMA [15,89] and therefore might make the nucleation on graphene with PMMA residues more difficult.

The surface cleanliness thus can lead to differences observed between the nucleation of ALD on the different graphene types, but differences are possible also between graphene samples synthesized by the same method. Prikle *et al*. studied the effect of the HOPG surface cleanliness on the uniformity of the ALD deposition of Al_2O_3 [65]. HOPG samples were annealed before ALD to remove contaminants and adsorbates from the HOPG surface. This resulted in a much lower nucleation density compared to a freshly exfoliated or H_2O rinsed HOPG surface. A difference was observed for deposition temperatures up to 200 °C, which indicates that even at high temperatures adsorbates can remain on the graphene surface and influence the ALD nucleation. Similarly, Kim *et al*. observed nucleation differences for CVD transferred to SiO_2 using different methods, a cleaner the transfer method resulted in a lower the ALD nucleation density [35]. The quality of the graphene and surface cleanliness should therefore always be taken into account when comparing ALD on different graphene types. Exfoliated graphene and HOPG are generally cleaner than epitaxial and CVD graphene. Additionally the exposure of the graphene to air leads to the adsorption of impurities on

the graphene surface, which can influence the ALD nucleation. Jeon *et al*. obtained a more uniform nucleation of Al_2O_3 on graphene if the sample was taken out of the ALD system and exposed to air every 17 cycles for a total of 69 cycles instead of growing 69 continuous cycles of Al_2O_3 on graphene [47]. This shows the adsorbed impurities from the air can enhance the ALD nucleation. Also other processing steps such as photo or electron beam lithography might result in additional residues on graphene, which can influence the ALD nucleation. Some of these steps might be difficult to avoid, but possible effects on the ALD nucleation should be taken into account. To increase reproducibility, procedures such as cleaning the graphene with a high temperature anneal (e.g. 400 °C) to reduce the amount of contaminants can be considered.

2.2.2 Influence of the ALD Deposition Temperature

The deposition temperature also plays an important role on the ALD nucleation on graphene. Physisorbed species tend to desorb at higher processing temperatures, whereas chemisorbed species are stable over a much wider temperature range. In the case of H_2O based ALD recipes, lower deposition temperatures (~ 100 °C) generally result in a more uniform ALD nucleation on graphene [26]. This is also shown in Figure 2.2, where 100 cycles of Al_2O_3 was deposited on graphene at a temperature of 100 °C and 200 °C. A higher Al_2O_3 surface coverage is obtained for the lower deposition temperature. H_2O tends to physisorb on graphene at these lower temperatures, making it more difficult to remove in the subsequent purge or pump steps. The physisorbed H_2O layer reacts in the subsequent ALD cycle with the trimethylaluminum (TMA) precursor, resulting in a more uniform deposition. The use of a lower deposition temperature and sufficient ALD cycles to achieve uniform ALD growth on graphene was studied by Zou *et al*. and Robinson *et al*. who both showed that for depositing HfO_2 on either exfoliated or epitaxial graphene at 110 °C a closed layer can be obtained after the deposition of approximately 30 nm of material [36,38]. Layers thinner than 30 nm, however, did not show uniform HfO_2 coverage.

Despite the advantage a lower deposition temperatures offers, the deposition temperature cannot be lowered indefinitely. This is because also the quality of the deposited high-κ dielectric is of importance, While there are also other limitations, such as the ALD growth window. A lower deposition temperature often leads to the incorporation of impurities and an increase of the hydrogen content in the form of hydroxyl groups, due to the lower reactivity of the H_2O. This reduces the dielectric constant of the material deposited [90]. Furthermore, at temperatures below 100°C H_2O

is generally difficult to remove from the ALD system, requiring long purge times to avoid unwanted CVD reactions.

In some cases the uniformity of the ALD deposition can increase with deposition temperature, depending on the reactivity of the precursor molecules. Xuan *et al*. for example, showed that the deposition uniformity of Al_2O_3 and HfO_2 on HOPG can be increased by using a higher deposition temperature (Figure 2.4) [23]. Films deposited at 200 °C still resulted in the selective deposition on the step edges of the HOPG for both Al_2O_3 and HfO_2 ALD, while on the basal plane no growth was obtained. However, when the deposition temperature was increased to 250 °C very rough, but closed HfO_2 films were deposited over the entire HOPG surface. For Al_2O_3 ALD this occurred at a temperature of 300 °C. The increase in the uniformity is caused by the reaction of one or more of the precursor molecules ($HfCl_4$, TMA or H_2O) with the sp^2 basal plane of the graphene [38]. This was confirmed using X-ray photoelectron spectroscopy (XPS) for HfO_2 ALD, which showed the formation of Hf-C bonds, at the interface between the HfO_2 and HOPG [53]. Similarly the TMA is likely to react with the HOPG surface at 300 °C. Despite the higher nucleation density obtained, the deposition of HfO_2 at these high temperatures has been shown to severely damage the graphene [38]. In the ideal case one would therefore like to deposit the dielectric on the graphene at a temperature at which the best properties are obtained for the material being deposited, while still obtaining uniform ALD growth on graphene and keeping the graphene intact.

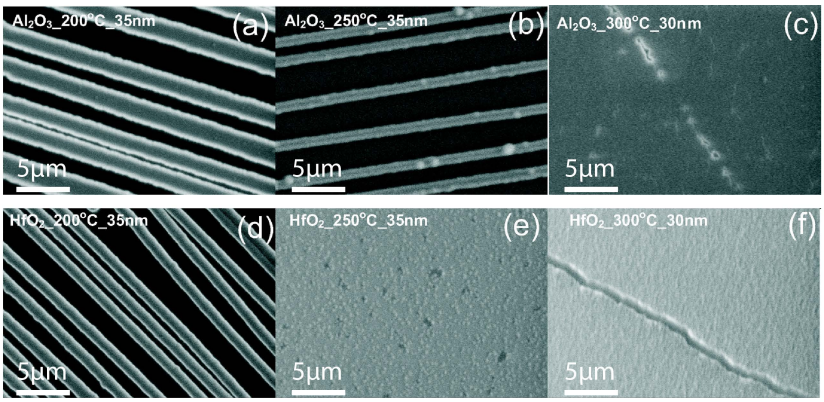


Figure 2.4: SEM images of Al_2O_3 ALD on HOPG deposited at a) 200 °C, b) 250 °C and c) 300 °C and HfO_2 ALD on HOPG deposited at d) 200 °C, e) 250 °C and f) 300 °C. For both HfO_2 and Al_2O_3 a more uniform growth is obtained at higher temperatures as a result of a reaction of the sp^2 bonded carbon with the ALD precursor molecules. The films however, are very rough and contain pinholes and cracks. Adapted from Xuan *et al*. with the permission of AIP Publishing [23].

2.2.3 Influence of the ALD Precursor Chemistry

The reactivity of grain boundaries, defects, wrinkles and the graphene basal plane towards ALD nucleation depends on the precursor used. The Pt precursor $MeCpPtMe_3$, for example, is much more reactive towards grain boundaries than the Al_2O_3 TMA ($Al(CH_3)_3$) precursor [15]. The presence of certain ligands in the precursor can increase the adsorption energies significantly. Aromatic acetylacetonate (acac, $C_5H_7O_2$) ligands have been shown to increase the physisorption of $Pt(acac)_2$ compared to $MeCpPtMe_3$ on graphene, likely due to π–stacking interactions between the graphene and the acac ligand [16]. Evidently, it is important to consider the precursor ligands when choosing a precursor for ALD on graphene.

The influence of the precursor chemistry on the nucleation behavior of HfO_2 was also investigated by Oh *et al*. [21]. Both $HfCl_4$ and tetrakis(dimethylamino)hafnium (TDMAH, $((CH_3)_2N)_4Hf$) were used to deposit HfO_2 films on exfoliated and CVD graphene using H_2O as the co-reactant at a substrate temperature of 250 °C. After 90 ALD cycles, HfO_2 covered 75% of the graphene surface when $HfCl_4$ was used as the Hf precursor, whereas only 35% of the surface was covered when TDMAH was used. DFT modeling showed that the physisorption of $HfCl_4$ on graphene is stronger compared to TDMAH, leading to an enhanced nucleation for $HfCl_4$. The results of Oh *et al*. indicate that the precursor chemistry plays an important role in the nucleation of ALD on graphene. Despite the advantages that a different precursor molecule might add, the number of types of precursors (for the same material) that have been tested in the literature is limited. This is because, apart from an advantageous adsorption on graphene, the precursor must satisfy many other requirements to be suitable for ALD processing, such as a high vapor pressure, good thermal stability and low cost, which limits the number of precursors available. In the case of Al_2O_3 for example, in all work published ALD on graphene TMA was used as the precursor. The robustness of the TMA-based ALD recipe and low cost of the precursor hamper the development and availability of alternative Al precursors that might be more suited for ALD on graphene.

2.2.4 Influence of the ALD dose and purge times

The lack of reactive surface groups on the graphene plane means that ALD precursor adsorption mostly relies on physisorption of the precursor molecules and co-reactant. Work by McDonnel *et al*. showed that increasing the precursor purge time from 30 s to 300 s the amount of Al_2O_3 deposited on HOPG was decreased significantly, while no

change was observed for a Si witness sample [63]. The difference between the different samples and purge times, was attributed to the physisorption of the precursor and reactant on the HOPG surface. When a longer purge time is used more of the precursor desorbs from the graphene surface, resulting in less material being deposited. A similar effect was observed by Aria *et al*. who instead of changing the purge times, increased the TMA precursor dose times (> 2 s) while keeping the purge times constant [22]. Longer dose times resulted in more uniform nucleation on HOPG and CVD graphene. The longer exposure to the precursor most likely resulted in an increase of the physisorbed species on the graphene surface. Because the purge times were kept constant, more molecules remained on the graphene after the purge step with increasing dose times, leading to an enhanced nucleation density and the deposition of a closed graphene layer after 12 cycles for the optimized conditions (i.e. by also exploiting the influence of the underlying graphene substrate on the ALD nucleation, which will be discussed in Section 2.2.5). Park *et al*. removed the purge times during the first few ALD cycles [42]. A closed Al_2O_3 layer of approximately 10 nm was deposited in this case. The complete removal of the purge times from the ALD process however, also results in unwanted CVD reactions occurring in the gas phase, which could lead to the deposition of non-uniform films.

The use of longer precursor doses does not necessarily lead to a more uniform deposition. An example of this is shown in Figure 2.5. The figure shows the deposition of Pt by ALD on CVD graphene grown on Cu foil. The Pt was deposited using $MeCpPtMe_3$ precursor and O_2 gas as co-reactant at a temperature of 300 °C [91]. Increasing the pressure of the co-reactant (effectively increasing the O_2 dose) results in a more selective deposition towards the wrinkles and grain boundaries of the graphene, most likely due to the diffusion of Pt. Pt is known to diffuse on surfaces by a process called ripening, which is dependent on the O_2 pressure [92,93]. At higher oxygen doses, increasing amounts of the Pt surface species are converted to PtO_x which have a higher diffusion rate [93,94]. This leads to an increased Pt diffusion over the graphene surface for larger O_2 doses allowing the Pt to diffuse to grain boundaries and wrinkles of graphene, which are energetically more favorable adsorption sites compared to the graphene basal plane [16]. The diffusivity of the precursor molecules on graphene can therefore strongly influence the ALD nucleation behavior. A similar effect has been observed for the deposition of Al_2O_3 using an Al or Ti seed-layer (see Section 3.2).

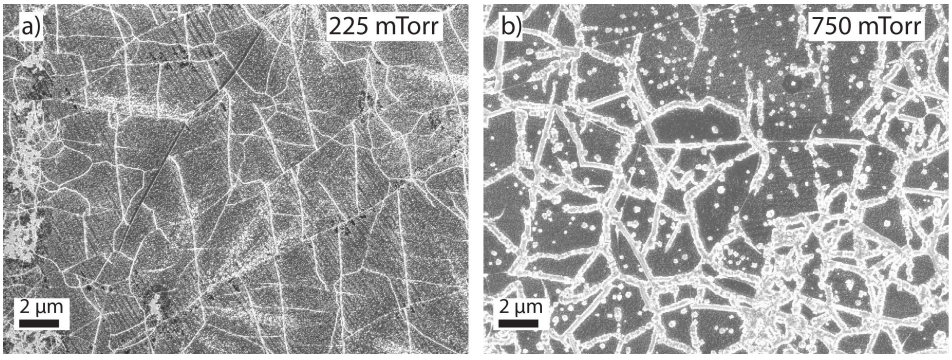


Figure 2.5: SEM micrograph of graphene grown on Cu foil after 500 cycles of Pt ALD at 300 °C. The Pt was deposited using $MeCpPtMe_3$ precursor and O_2 gas as co-reactant. The O_2 pressure was varied a) 225 mTorr and b) 750 mTorr. A more uniform Pt deposition can be observed for the lower O_2 pressure (the density of Pt particles in-between the grain boundaries and wrinkles goes is reduced with increasing O_2 pressure).

2.2.5 Influence of the Underlying Substrate

Apart from the ALD process parameters and the cleanliness of the graphene surface the underlying substrate also plays an important role in the nucleation of ALD films on graphene, as was shown by Dublak *et al*. [26]. The deposition of 100 cycles of Al_2O_3 on HOPG and CVD graphene transferred to SiO_2 without any pretreatment did not result in the growth of a uniform layer, see Figure 2.6a. However, when the CVD graphene was present on a Cu substrate, uniform deposition of Al_2O_3 on graphene was obtained (Figure 2.6b). Similarly, using Ni-Au as the underlying substrate led to a uniform film of Al_2O_3 on graphene [26]. However, when multi-layer graphene was used on the same substrates the growth was similar to that on the HOPG and SiO_2 substrates. The enhanced nucleation when a metallic substrate was used, was ascribed to the formation of polar traps on the graphene surface due to the interaction of the metal with the graphene. The adsorption of H_2O molecules was increased due to the presence of these polar traps resulting in the uniform nucleation of Al_2O_3 on graphene.

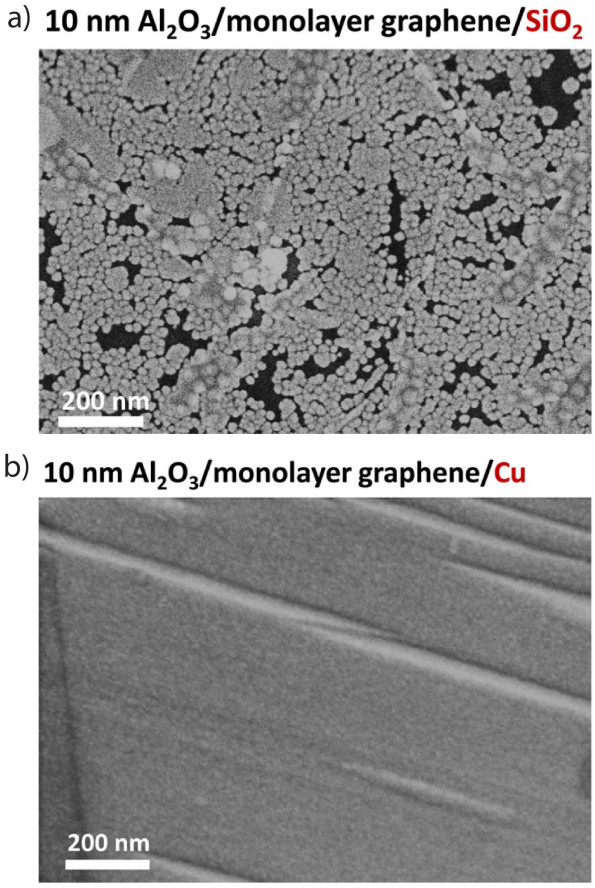


Figure 2.6: SEM image of the ALD growth of 10 nm Al_2O_3 at 80 °C on graphene using a) SiO_2 as the underlying substrate and b) Cu as the underlying substrate. The use of SiO_2 as the underlying substrate does not result in uniform Al_2O_3 growth on graphene, However, when Cu is used as the underlying substrate uniform ALD of Al_2O_3 deposition is observed. Adapted from Dlubak *et al.* with the permission of AIP Publishing [26].

For non-H_2O processes the underlying substrate can also be of importance for the nucleation, as is demonstrated in Figure 2.7, which demonstrates the deposition of Pt on graphene supported by Si nano pillars and free-standing graphene, in the gap between the pillars. A higher Pt nucleation density is observed for the graphene supported by the Si pillars compared to the free standing graphene. Although the precise cause for this enhanced nucleation behavior is not yet fully understood, it shows that the interaction between the graphene and the substrate can strongly influence the ALD nucleation. The appropriate choice of substrate thus makes it possible to obtain closed layers that are

significantly thinner than when the standard silicon oxide substrate is used. This can also be observed in Table 1: For semiconductor and metal substrates generally a closed layer is obtained at lower thicknesses compared to an oxide substrate using the same functionalization process. For many applications, however, the choice in substrates is limited and this effect can therefore not always be exploited.

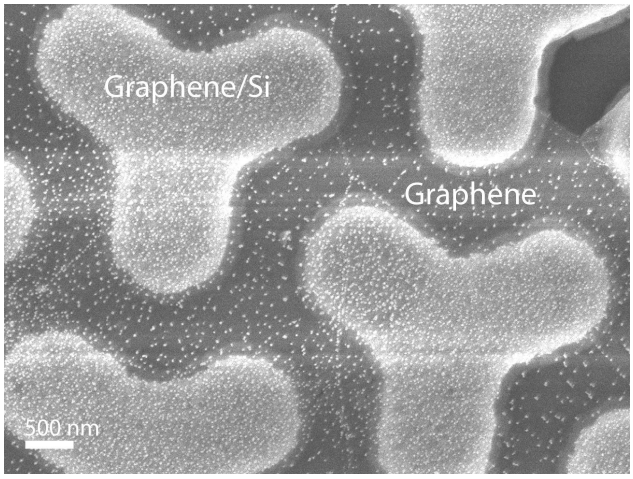


Figure 2.7: 500 cycles of Pt ALD on graphene transferred to Si pillars. The graphene in between the nano pillars is free-standing, i.e. not supported by a substrate. An increased nucleation density can be observed on the Graphene/Si nano pillars compared to the free standing graphene.

Summarizing, the direct deposition of dielectric layers and metals on graphene by ALD does not result in uniform film growth, but in the selective deposition on the graphene grain boundaries, defects and wrinkles. The selective growth is a result of the lack of out of-plane bonds on the graphene, due to its sp^2 C configuration. Because the precursor molecules physisorb on the graphene instead of chemically bonding to the graphene, the ALD process conditions such as substrate temperature, pump times, purge times and the precursor chemistry strongly affect the deposition uniformity. The appropriate choice of precursor and substrate, as well as increasing the dose times, shortening the purge times and lowering the deposition temperature can increase the nucleation uniformity. Despite numerous efforts to optimize the process conditions, obtaining closed dielectric layers < 10 nm is still troublesome and for many applications changing the substrate is not an option. Furthermore, the strong dependence on process conditions does not provide the best solution when reproducible results are required. To this extent the creation of functional groups on the graphene surface to enhance the

nucleation of ALD on graphene has been studied extensively throughout literature and will be discussed in the next section.

2.3 Uniform ALD on Graphene Through Surface Preparation

To enable uniform ALD on graphene the creation of functional groups on graphene has appeared to be essential. The functional groups provide adsorption sites on which the precursor molecules can chemisorb resulting in ALD of uniform films on the graphene surface. The functional groups can be created directly on the graphene itself or by the deposition of a seed-layer on the graphene. The creation of functional groups directly on the graphene can be achieved by, for example, an O_2 plasma treatment. The plasma treatment converts part of the sp^2 bonds to out-of-plane sp^3 bonds and leads to the attachment of oxygen containing surface groups. The disruption of the sp^2 backbone of the graphene by these treatments, however, results in the deterioration of the electrical properties of the graphene, such as the charge carrier mobility. The use of seed-layers avoids changing the sp^2 structure of the graphene. However, in this case one faces other challenges such as a lower dielectric material quality or an increase in the equivalent oxide thickness (EOT) due to the low dielectric constant of the seed-layer.

The various methods used to initialize ALD growth on graphene, shown in Table 1, can be roughly be divided into four categories: 1) the deposition of polymer seed-layers on the graphene such as self-assembled monolayers (SAMs), 2) the evaporation of metal or metal-oxide seed-layers on the graphene, 3) the creation of functional groups directly on the graphene by plasma or reactive gas functionalization, and 4) the use of wet-chemical treatments such as RCA cleaning or dipping the graphene in H_2O before processing. Each of these methods will be discussed in more detail below.

2.3.1 Polymer Seed-layers

The use of polymer seed-layers to achieve uniform growth on graphene was first investigated by Wang *et al*. who used 3,4,9,10-perylene tetracarboxylic acid (PTCA), a SAM, to obtain uniform Al_2O_3 layers (2.8 nm thick) on graphene, as shown in Figure 2.8 [14]. To cover the graphene with PTCA, graphene flakes were immersed in a PTCA solution for approximately half an hour. The PTCA contains carboxylate terminated groups which served as adsorption sites for the TMA precursor. Although not investigated, it is suggested that damage to the graphene is prevented by the non-

covalent bonding of the PTCA to the graphene. Along with PTCA several other SAMs have been used to obtain uniform Al_2O_3, HfO_2 and ZnO layers on graphene such as perylene-3,4,9,10-tetracarboxylicdianhydride (PTCDA) [6,44], perfluorodecyltrichlorosilane (FDTS) [45] and 4-mercaptophenol (4MP) [51]. The use of Hexamethyldisilazane (HMDS) as a seed-layer led to the deposition of non-uniform Al_2O_3 films[47], possibly because of the hydrophobic nature of the functional groups, which decreased the adsorption of H_2O on the HDMS treated graphene surface.

Polymer seed-layers are typically deposited on the graphene by spin coating and are typically between 5 – 10 nm thick. Farmer *et al*. used the polymer NFC 1400-3CP (a polyhydroxystyrene derivative) to initiate the ALD growth of uniform 10 nm thick layers of HfO_2 on graphene [49]. After ALD, top gated field effect transistors (FETs) where made. The FET devices showed that the charge carrier mobility of the graphene decreased ~ 15% after polymer deposition and subsequent HfO_2 ALD. Further analysis showed that additional phonon scattering introduced by the polymer layer was the most likely cause for the observed reduction of the mobility. Apart from a small reduction in the carrier mobility the polymer buffer layer also lead to strong p-doping of the graphene. This resulted in a 42.5 V shift in the Dirac voltage which decreased to 13.3 V after HfO_2 ALD. The doping of the graphene by the polymer buffer layer can be reduced by the appropriate choice of the polymer layer, as was shown by Shin *et al*. who used poly(4-vinylphenol) to obtain uniform (25 nm thick) Al_2O_3 layers on graphene, which reduced the Dirac point shift to ~ 1.5 V. Both Sangwan *et al*. [6] and Shin *et al*. [78] showed that the use of a polymer seed-layer or SAM also enhances the reproducibility of devices made compared to devices where no seed-layer is used. The increased device reproducibility is likely caused by the more uniform ALD on the seed-layer as compared to the non-functionalized graphene devices. Device reliability test by Sangwan *et al*. showed that using Al_2O_3 as a buffer layer between the HfO_2 gate and polymer resulted in superior performance compared to devices that only used HfO_2 as a gate dielectric. Further analysis showed that the PTCDA seeded the Al_2O_3 growth more effectively than the HfO_2 growth.

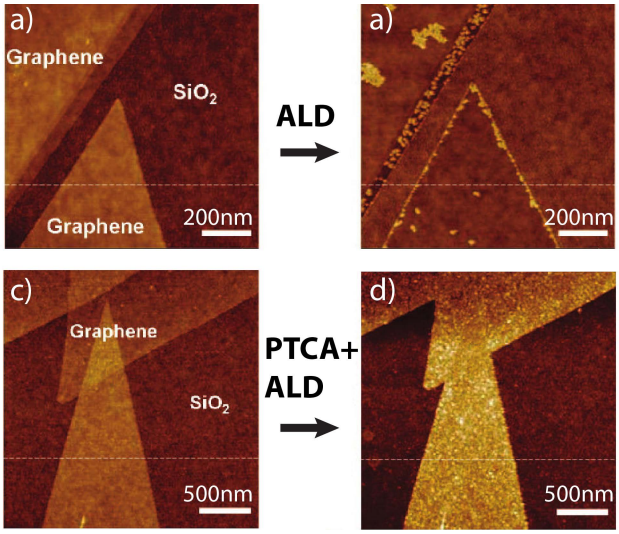


Figure 2.8: Atomic force microscope (AFM) images of pristine graphene a) before and b) after Al_2O_3 ALD and of PTCA functionalized graphene c) before and d) after PTCA treatment and ALD. Adapted with permission from Wang *et al*. Copyright (2008) American Chemical Society [14].

All reported SAMs and other polymeric seed-layers have a limited influence on the graphene properties. Furthermore, fabricated devices show good reproducibility and therefore are a promising method to achieve uniform dielectric layers on graphene. However, there are some hurdles that need to be overcome to make polymer buffer layers or SAMs suited for future device integration. The tested SAMs and other polymers all have a relatively low dielectric constant, which together with the relatively large thickness of the films limits the minimum EOT of the gate dielectric. For example a 9 nm NFC 1400-3CP seed-layer has a dielectric constant of ~ 2.5 resulting in a EOT of 14 nm for the polymer layer alone. Reducing the EOT thickness is essential for the further improvement of graphene devices. Meric *et al*. have shown that by using poly-vinyl alcohol (PVA), a polymer with a relatively high dielectric constant (~ 6), the EOT can be reduced significantly [52]. The use of a 2.5 nm PVA layer was sufficient to obtain a closed HfO_2 layer after only 50 ALD cycles (~ 5 nm). To initiate the HfO_2 ALD growth on the PVA, an ozone pre-treatment was required. As will be discussed in Section 2.3.3, ozone treatments can also be used to functionalize the graphene directly without the need of a polymer seed-layer, allowing for an even better EOT scaling of the gate dielectric. Despite the potential of polymer seed-layers to obtain uniform ALD growth on graphene without damage, other functionalization approaches offer better opportunities to scale down the dielectric thickness.

2.3.2 Evaporated Metal and Metal-oxide Seed-layers

The relatively low EOT of the polymer buffer layers has led to the exploration of metal and metal-oxide seeding layers to initiate the ALD growth on graphene. The metal and metal-oxide layers can be deposited using e-beam evaporation at room temperature. In the case of using metal seeding-layers these can be oxidized by the exposure of the samples to air after seed-layer deposition [10,60] or by the use of O_2 as a background gas during evaporation [55]. The method was introduced by Kim *et al*. who used a thin Al seed-layer, oxidized in air during transfer to the ALD chamber, after which 15 nm of Al_2O_3 was deposited by ALD on top [10]. To ensure the Al seed-layer was fully oxidized the sample was exposed to a H_2O step in the ALD chamber at an elevated temperature. FET devices fabricated from the sample showed mobility values up to 8600 cm^2/Vs and a Dirac voltage of 0.08 V, indicating that doping of the graphene can be avoided when a metal seed-layer is used. The dielectric constant of the deposited Al_2O_3, however, was relatively low (6.0 instead of 8-9), indicating that further optimization is possible. Despite that the mobility of the graphene devices without the Al_2O_3 seed-layer was not determined, this work shows the potential of using a evaporated metal seed-layer to initiate ALD growth.

The deposition of an Al seed-layer might still damage the graphene despite the good mobility values reported by Kim *et al*. [10] For example, Fallahazad *et al*. used an Al seed-layer to initialize the ALD growth of HfO_2 on mono and bi-layer graphene [60]. A strong decrease in the mobility of the graphene was observed after Al evaporation and the deposition of the first 2-4 nm of oxide, as shown in Figure 2.9. The decrease of the mobility was attributed to charged impurities being introduced after seed-layer and dielectric deposition. These were most likely oxygen vacancies present in the deposited Al or HfO_2 films a result of the incomplete oxidation of these layers.

Later work by Fallahazad *et al*. showed that the Al seed-layer on graphene is also relatively rough when compared to using an Ti seed-layer. This is caused by a higher surface mobility of Al atoms on graphene. The low surface mobility of Ti atoms allowed for the deposition of seed-layers down to 0.6 nm in thickness compared to 2.6 nm for Al. Furthermore the oxidized Ti seed-layers had a higher dielectric constant 12.7 versus 5.5, making further downscaling of the EOT possible.

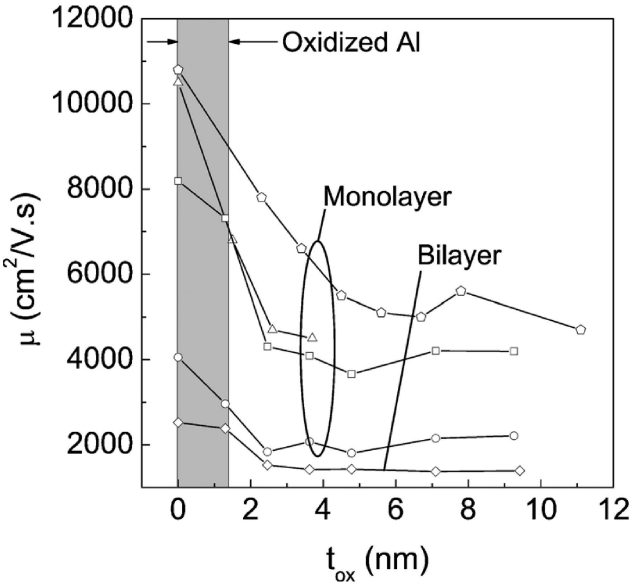


Figure 2.9: Mobility μ plotted versus the oxide thickness t_{ox} for monolayer and bilayer graphene devices prepared using a e-beam evaporated Al seed-layer and an ALD HfO_2 film. A sharp mobility decrease can be observed for the deposition of the first 2-4 nm of oxide, which remains approximately constant for thicker dielectric films. Adapted from Fallahazad *et al*. with the permission of AIP Publishing [60].

Robinson *et al*. deposited several materials (Al_2O_3, HfO_2, Ta_2O_5 and TiO_2) by ALD on epitaxial graphene. The evaporated metal counterpart of the oxide was used as a seed-layer [38]. Full oxidation of the metal seed-layer was ensured by pulsing H_2O (10 pulses 10 s each) before deposition of the ALD layer. A uniform ALD film could be obtained for all oxides although the ALD deposition temperature strongly affected the coverage. For example, Al_2O_3 deposited at 150 °C was rough and contained pin holes, whereas depositing Al_2O_3 at 300 °C led to the deposition of a more uniform film. In the case of Ta_2O_5 closed layers could be obtained, but the resulting films were very rough independent of the deposition temperature. Raman measurements indicated that the deposition of a Ta seed-layer also led to damage to the graphene film, which was in agreement with a strong reduction of the carrier mobility observed by the hall measurements. The use of an Al seed-layer resulted in a reduction of the mobility similar in magnitude as observed by Fallahazad and Farmer *et al*. [49,60]. For HfO_2 a slight increase in the mobility of graphene was observed after ALD and a significant increase for TiO_2. The increase observed after deposition of a Ti seed-layer and subsequent ALD is possibly caused by the charge compensation of the substrate

induced doping, often observed for SiC substrates. This observation was supported by an approximately twofold decrease in the charge carrier concentration of graphene after ALD.

The use of metal-oxide seed-layers to initiate the ALD growth on graphene was investigated first by Hsu *et al*. who e-beam evaporated 5 nm of SiO_2 on graphene followed by ALD of 15 nm of Al_2O_3 for the fabrication of RF transistors [61]. The mobility of the fabricated devices reduced from 2000 ± 500 cm^2/Vs before dielectric deposition to ~ 500 cm^2/Vs after e-beam evaporation and ALD, the SiO_2 seed-layer being the most likely cause for the significant degradation of the graphene. Such a significant degradation of the carrier mobility after SiO_2 e-beam evaporation was also observed by Hollander *et al*. who used it to initiate the ALD growth of HfO_2 on graphene, as illustrated in Figure 2.10. Part of the mobility reduction could be due to the relatively low dielectric constant of the SiO_2 seed-layer, which is known to enhance the impurity scattering in the graphene [95].

Beside SiO_2 seed-layers also Al_2O_3 and HfO_2 seed-layers were investigated by Hollander *et al*. Both the Al_2O_3 and HfO_2 seed-layers, ~ 2 nm thick, showed an improvement of the mobility irrespective of whether Al_2O_3 or HfO_2 was deposited on the seed-layers. Raman spectroscopy confirmed that the graphene was indeed not damaged by the seed-layer deposition. The use of a HfO_2 seed-layer increased the mobility further compared to Al_2O_3 (see Figure 2.10). This is a result of the higher dielectric constant of HfO_2, which helps to reduce the charged impurity scattering through dielectric screening [96]. Although both the heterogeneous material stack (Al_2O_3/HfO_2 or HfO_2/Al_2O_3) and homogeneous stacks (Al_2O_3/Al_2O_3 or HfO_2/HfO_2) improved the graphene properties, the dielectric performance of the homogenous material stacks was superior to the heterogeneous stacks. The larger roughness of the heterogeneous stacks combined with the trapping of charges at the interface between the two different dielectrics being the most likely cause for the lower performance. Despite the good properties obtained for the homogenous stacks, still a hysteresis of 0.5 to 0.7 V was observed in the measured transfer curves, indicating that even for these devices trapped charges remain present in the deposited oxide layer. These trapped charges limit the improvement of the graphene devices after dielectric deposition.

The quality of both the graphene and the dielectric deposited thus strongly depend on the type of metal or metal-oxide seed-layer deposited by e-beam evaporation. The use of Ti as a seed-layer shows the most promise due to the reduced roughness of the e-beam evaporated films and higher dielectric constant compared to for example Al, Ta and SiO_2 e-beam evaporated films, furthermore the Ti seed-layer did not damage the

graphene. Hf seed-layers are also an option, but care should be taken that the deposition temperature of the ALD process is low enough to prevent the formation of Hf-C bonds which disrupt the sp^2 C backbone of graphene and deteriorate its electrical properties, as discussed in Section 2.2.2.

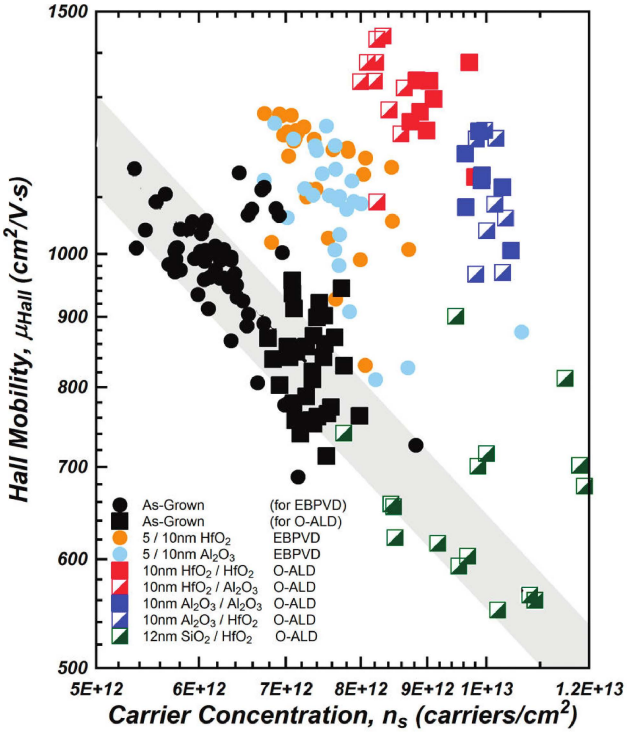


Figure 2.10: Evaluation of the Hall mobility μ_{Hall} as a function of the carrier concentration n_s for graphene devices fabricated on SiC. The results indicate that the deposition of a high-κ dielectric on the epitaxial graphene by either oxide seeded ALD (O-ALD) or e-beam evaporation (EBPVD) leads to a mobility improvement. Furthermore, the ALD seeded devices outperform the devices fully prepared by EBPVD. Adapted with permission from Hollander *et al*. Copyright (2011) American Chemical Society [59].

Apart from e-beam evaporated metal or metal-oxide seed-layers almost no other deposition techniques have been investigated to achieve uniform ALD nucleation. This is because other PVD techniques easily damage the graphene [13]. Jeong *et al*., for example, tried to use sputtered ZnO as a seed-layer to achieve uniform HfO_2 growth on graphene [51]. Although uniform HfO_2 layers of ~ 17 nm could be deposited on the sputtered ZnO, Raman analysis showed that the graphene was completely etched after

the ZnO deposition, due to sputtering induced plasma damage. Since this plasma damage is intrinsic to the sputtering technique, it is not suited for the deposition of ALD nucleation layers on graphene.

Consequently, the combination of PVD techniques, such as e-beam evaporation, sputtering or pulsed laser deposition with ALD to obtain uniform dielectric layers on graphene is a compromise. On one side the material quality and thickness control of ALD is superior to those of the PVD techniques and it prevents damaging the graphene, but the inert nature of the graphene makes nucleation difficult. PVD techniques on the other hand make deposition on the graphene possible but suffer from low material quality, limited thickness control and damage to the graphene [13]. Combining PVD with ALD therefore limits the exposure time of graphene to reactive species, such as ions, which are inherent to PVD techniques, and could damage it significantly. Therefore, completely avoiding this damage remains difficult. The deposition of uniform layers with ALD directly on graphene would avoid these issues, which will be discussed in the next section.

2.3.3 Surface Functionalization

The use of polymer seed-layers to initialize ALD growth on graphene makes it difficult to achieve good EOT scaling, but avoids damaging the graphene. Metal and metal-oxide seed-layers on the other hand easily damage the graphene, but provide good EOT scaling. To circumvent the tradeoff between these two approaches the direct ALD on graphene using surface functionalization treatments has been investigated extensively in literature, for example, by using ozone or O_2 and N_2 plasma treatments. The treatments create oxygen and nitrogen functional groups on the graphene on which the ALD precursor molecules can adsorb, ideally allowing for the deposition of a uniform ALD layer.

The use of O_3 pre-treatments, or the replacement of the H_2O co-reactant by O_3 was investigated first. This is because plasma treatments are generally considered more aggressive and are expected to easily damage the graphene, whereas O_3 treatments are relatively mild. Lee *et al*. studied the deposition of Al_2O_3 on HOPG, comparing the normal H_2O Al_2O_3 ALD process with a process where the H_2O pulse was replaced by O_3 exposure [24]. For the H_2O-based process only ALD growth on the step edges of the HOPG was observed, whereas for the O_3 ALD process a more random nucleation was obtained. However, for both processes no uniform deposition of Al_2O_3 was obtained after 50 ALD cycles at 200 °C. To obtain uniform deposition of Al_2O_3 on the HOPG an

additional ozone pretreatment was required. The ozone pretreatment followed by the O_3 ALD process resulted in the deposition of closed Al_2O_3 layers down to 9.5 nm thick. XPS analysis showed that the O_3 pretreatment created epoxide (C-O) carbonyl (C=O) and carboxyl (O-C=O) containing surface groups on the HOPG surface, which enhanced the ALD nucleation but also indicated a change of sp^2 C to sp^3 C which is likely to deteriorate graphene device performance. Similar observations were made by Prikle *et al*. who showed that an O_3 ALD process increases the nucleation density of the Al_2O_3 on HOPG, but who also found that achieving a closed layer remains difficult when no O_3 pretreatment is used [65]. However, because HOPG is not suited for device fabrication the influence of the O_3 treatment on the properties of the graphene remained unclear.

The importance of the O_3 pretreatment before ALD was investigated further by McDonnel *et al*. who changed the pulse order during ALD (i.e TMA first or O_3 first) and its effect on the nucleation, see Figure 2.11 [63]. First dosing TMA lead to an almost uniformly deposited Al_2O_3 films after 6 ALD cycles. O_3 first, however, lead to the selective nucleation of Al_2O_3 growth on the HOPG step edges. XPS measurements of the HOPG surface indicated that short O_3 exposures, as typically used during ALD processing, clean the surface of contaminants and therefore remove possible precursor binding sites. These possible binding sites remain for a TMA first process and thus explain the higher nucleation density compared to the O_3 first process. Long doses of O_3, like the pretreatments used by Lee *et al*., first clean the graphene and subsequently create functional groups on the graphene surface. The duration of the O_3 pretreatment therefore plays an important role in tuning the nucleation density.

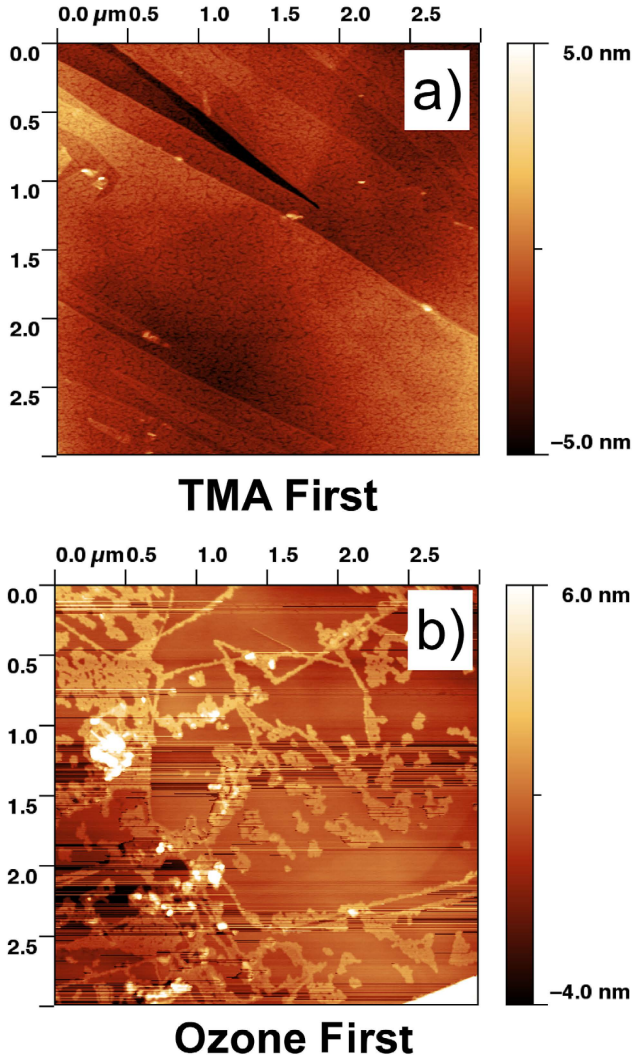


Figure 2.11: AFM image of Al_2O_3 deposited on HOPG by starting with a) the TMA pulse and b) an O_3 pulse. The difference in coverage illustrates the importance of the ALD pulse sequence on uniformity on ALD Al_2O_3. For the TMA first process an almost uniform layer is obtained whereas for the O_3 first process preferential deposition on the step edges is obtained. Adapted from McDonnel *et al*. with the permission of AIP Publishing [63].

When similar work was done on CVD and exfoliated graphene it was discovered that the O_3 pretreatments at high temperatures (> 150° C) severely damaged the graphene [66,67], which agrees with the change from sp^2 C to sp^3 C observed by XPS, as discussed above. Lee *et al*., however, showed that at low temperature (25 °C) damage

to the graphene can be prevented. This was later confirmed by Jandhyala *et al*. who showed, using *ab inito* calculations, that at temperatures > 150 °C the O_3 chemisorbs on the graphene changing the sp^2 carbon backbone to sp^3 carbon [67]. At 25 °C, however, the O_3 physisorbed on the graphene, leaving the sp^2 backbone intact. During the subsequent TMA pulse the physisorbed O_3 reacted with the TMA forming a Al_2O_3 nucleation layer. The quality of the Al_2O_3 deposited at 25 °C is, however, not optimal. To improve this the temperature was increased after 4 TMA/H_2O cycles at 25 °C to 150 °C where an additional 32 cycles of TMA/ H_2O ALD were performed, obtaining a uniform Al_2O_3 layer of 4.5 nm thick. Fabricated FETs showed an significant increase of the mobility after Al_2O_3 deposition with a maximum of ~ 19.000 cm^2/Vs. The increase in the mobility was attributed to the removal of surface contaminants by the ozone treatments, such as resist residues left over from the graphene transfer process, the barrier properties of the Al_2O_3 preventing impurities, such as O_2 and H_2O, adsorbing on the graphene and the charge screening of the Al_2O_3 dielectric.

A combination of O_3 ALD and the substrate enhanced nucleation of Ni (Section 2.2.5) was used by Martin *et al*. to deposit Al_2O_3 layers on graphene for the integration of graphene in a spin selective membrane in magnetic tunnel junctions (MTJ). A closed layer was obtained after only 6 ALD cycles, corresponding to a thickness of 0.6 nm. These are the thinnest uniform Al_2O_3 layers on graphene reported to date. The ALD layers are thinner than any of the polymer, metal or metal-oxide seed-layers discussed in Sections 2.3.1 and 2.3.2. Despite that not always a metal substrate can be used to enhance nucleation, this shows the promise of O_3 functionalization to deposit ultra-thin dielectrics on graphene.

Apart from O_3 functionalization also NO_2 has been extensively investigated in literature as a replacement for the H_2O step in the ALD process. The method was introduced by Farmer *et al*. for the deposition of Al_2O_3 on single wall carbon nanotubes [97] and later adapted for the nucleation of Al_2O_3 on graphene by Williams *et al*. who used 50 NO_2/TMA ALD cycles at room temperature followed by 305 cycles of H_2O/TMA at 225 °C to deposit ~ 30 nm thick continuous Al_2O_3 films on graphene [71]. The NO_2 adsorbs non-covalently on the graphene surface, most likely through a charge transfer mechanism [69]. In the subsequent TMA exposure the NO_2 reacts with the TMA forming Al_2O_3 islands. Because the NO_2 does not adsorb on Al_2O_3 the reaction stops when the entire graphene surface is covered by Al_2O_3, at a thickness of ~ 8.0 nm. The relatively large thickness required before growth stops, could indicate that even with NO_2 the nucleation on graphene is not completely uniform. Later work by Farmer *et al*. showed that the use of NO_2 as a reactant gas instead of H_2O lead to a strong

mobility decrease of the graphene [49]. This was later confirmed by Lin *et al*. who attributed the mobility decrease to the charged impurity scattering of the NO_2 grown Al_2O_3 nucleation layer. The severe deterioration of the graphene's electrical properties, make NO_2 treatments to initialize ALD growth unsuited for device applications. Other applications, however, where the quality of the graphene is not important, NO_2 functionalization can still be used. An example is the fabrication of thin oxide membranes. In this case the graphene is only used as a growth support and etched after ALD processing, which makes it possible to fabricate of 2.8 nm thick freestanding Al_2O_3 membranes [72].

Wheeler *et al*. investigated the exposure of graphene to XeF_2 gas to enhance ALD of Al_2O_3 on graphene [81]. Graphene was exposed to XeF_2 for various exposure times. The XeF_2 dissociates on the graphene at room temperature forming C-F functional groups. The amount of C-F groups created increased as a function of the XeF_2 exposure time. An optimum was found for a C-F group coverage of approximately 6-7%, where a uniform Al_2O_3 layer was deposited on the graphene after ~ 15 nm. Lower coverages did not result in a closed graphene layer, higher coverages of C–F could not be obtained due to the formation of $C\text{-}F_2$ which decreased the total density of reactive surface sites. Hall measurements showed a ~ 10-15% increase in the mobility after Al_2O_3 ALD. This mobility increase is smaller than normally observed after Al_2O_3 ALD [59,67], possibly due to charged impurity scattering at the graphene/Al_2O_3 interface.

The use of plasma treatments to obtain the uniform nucleation of ALD on graphene was first reported by Nayfeh *et al*. who replaced the H_2O co-reactant dose by a O_2 plasma step, for the deposition of Al_2O_3 on graphene [74]. Fabricated devices containing the plasma deposited Al_2O_3 as a gate dielectric were compared to devices with a SiO_2 e-beam evaporated dielectric. The plasma prepared Al_2O_3 devices performed significantly better, but this is most likely due to the poor quality of the SiO_2 devices (as discussed in Section 2.3.2). Furthermore the dielectric constant of SiO_2 is significantly lower compared to that of Al_2O_3, which could also explain the difference in performance. Raman measurements of both the plasma deposited Al_2O_3 and the SiO_2 e-beam reference samples revealed defects, indicating that the graphene is indeed damaged by the O_2 plasma. Later work by Lim *et al*. showed that N_2 plasma pre-treatments can also be used for the uniform deposition of Al_2O_3 on graphene [73]. It was suggested that the N_2 plasma creates defects in the graphene, which act as nucleation sites for the TMA or H_2O precursor and co-reactant. The nature of the defects sites created was not investigated, but these are most likely nitrogen containing surface groups, which react with the TMA, similarly as observed for the NO_2/TMA process.

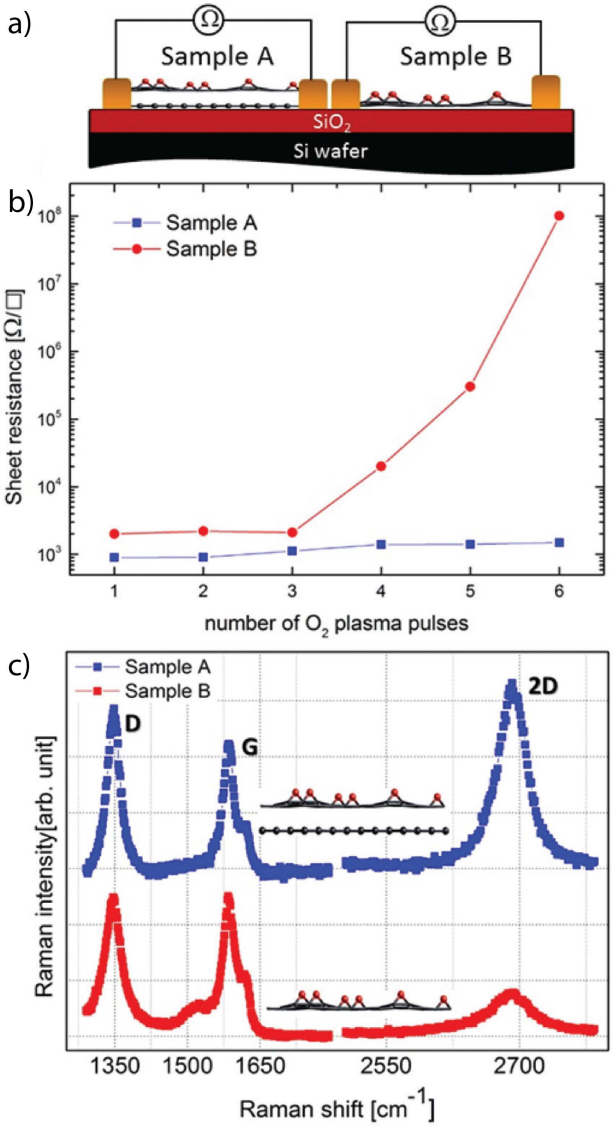


Figure 2.12: a) Schematic diagram of the method employed by Nourbakhsh *et al*. For sample A the underlying graphene is protected by a sacrificial graphene layer. An unprotected graphene layer is used as a reference, sample B. b) Relationship between the sheet resistance and the number of O_2 plasma pulses for the protected and unprotected sample. c) Raman spectra of the protected and unprotected sample after 6 O_2 plasma pulses. Adapted from Nourbakhsh *et al*. with permission of The Royal Society of Chemistry [77].

To circumvent the damaging of the graphene by an O_2 plasma treatment Shin *et al*. performed the O_2 plasma treatment on a sacrificial graphene layer [39]. The O_2 plasma treatment created epoxide and carboxyl groups on the graphene, converting it to graphene oxide (GO). This GO was transferred on top of an untreated graphene layer. Next 22.3 nm of Al_2O_3 was deposited on the graphene /GO stack. The deposition of a smooth and continuous Al_2O_3 film, was confirmed by Atomic force microscopy (AFM). Nourbakhsh *et al*. also performed O_2 plasma treatments on a sacrificial graphene layer which was, transferred on top of the graphene channel before the plasma treatment, as illustrated in Figure 2.12 [77]. The top layer of graphene was oxidized by the O_2 plasma exposure and at the same time protected the underlying graphene layer. With this method uniform Al_2O_3 layers down to 4 nm could be deposited. FET devices fabricated with the abovementioned processes preformed similarly to back-gated graphene-FETs and showed an improved gate capacitance over Al e-beam seeded Al_2O_3 FETs [77,78]. A disadvantage of using a sacrificial graphene layer is the requirement of an additional graphene transfer step. This makes the functionalization process time consuming. Furthermore, the extra transfer step, could trap polymer residues left over from the previous transfer procedure in between the graphene layers. To avoid the need for an additional transfer step Nath *et al*. spin-coated GO flakes prepared by chemical exfoliation on top of epitaxial graphene [79]. The GO layer (~ 1.5 nm thick) acted as a seed-layer for the subsequent ALD growth of Al_2O_3, HfO_2 and TiO_2. The GO was stable up to 400 °C, which made it possible to deposit the films at the optimal ALD process conditions, without damaging the epitaxial graphene. The dielectric constants of the deposited films were identical to those deposited on a Si witness sample and close to their ideal values [79].

Vervuurt *et al.* developed a plasma functionalization method which avoids the use of a sacrificial graphene or GO layer altogether [32]. In this case the graphene was functionalized by a H_2 plasma treatment. The H_2 plasma treatment created C-H functional groups on the graphene surface, enhancing the adsorption of the TMA precursor molecules, allowing for the deposition of uniform Al_2O_3 films down to 8 nm in thickness on graphene. As for O_2 plasma treatments, the H_2 plasma treatment initially led to the sp^3 hybridization of graphene, which resulted in a drastic reduction of the graphene charge carrier mobility. Contrary to O_2 plasma functionalized graphene however, this reduction in charge carrier mobility was fully recovered upon Al_2O_3 ALD. Subsequent annealing at 400 ºC further improved the mobility. Density functional theory calculations showed that this is caused by the abstraction of hydrogen functional

groups from the graphene upon Al_2O_3 precursor adsorption, which recovered the sp^2 hybridization of the graphene (see Figure 2.13).

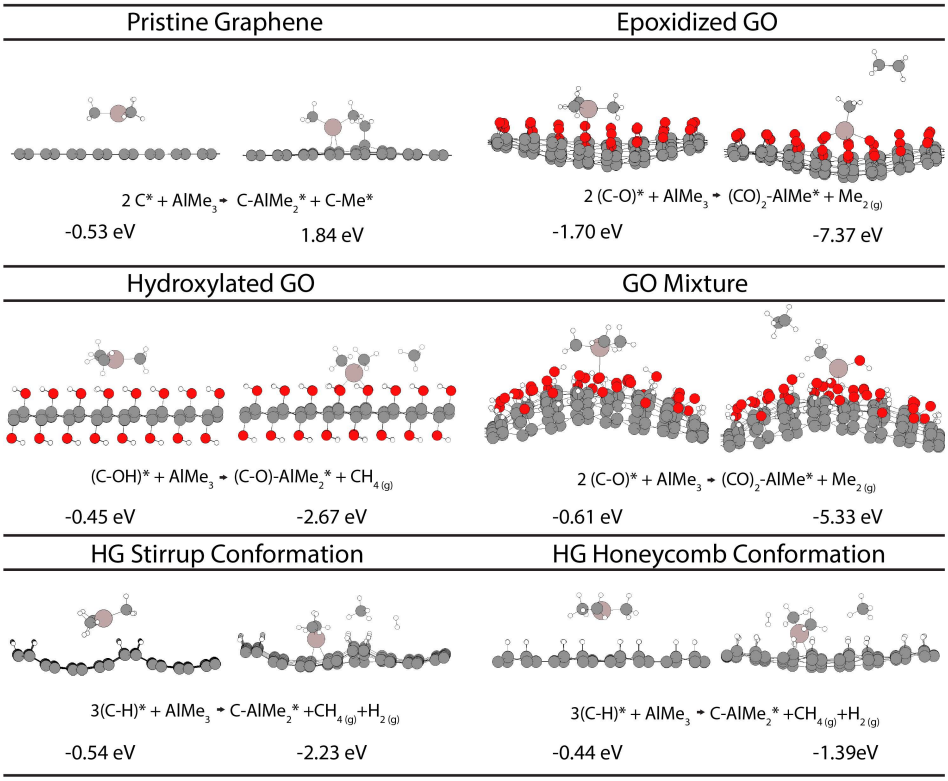


Figure 2.13: DFT-predicted structures and related relative energies of the lowest-energy (left) physisorbed and (right) chemisorbed species on pristine graphene, oxygenated graphene (i.e. graphene oxide, GO) and hydrogenated graphene (HG). For GO and HG the two most likely configurations are given. The adsorption of TMA on hydrogenated graphene is accompanied by the release of H_2 from the graphene surface, restoring the graphene to its pristine sp^2 C state. Adapted from Vervuurt *et al.* Copyright (2017) American Chemical Society [32].

Johns *et al*. replaced the H_2O pulse with atomic oxygen, created by flowing O_2 along a heated tungsten filament, for the growth of ZnO on epitaxial graphene [80]. The exposure of graphene to atomic oxygen led to the formation of epoxide groups on the graphene surface. The subsequent exposure to the diethyl zinc precursor (DEZ) abstracted these oxygen groups from the graphene surface, creating mobile metal oxide clusters no longer bonded to the graphene [98]. AFM images showed the uniform nucleation of ZnO on the graphene, while Raman analysis indicated that no defects

where created in the graphene after the atomic oxygen and DEZ exposure. No closed layers were grown, however, probably because the atomic oxygen exposure and DEZ exposure were performed at room temperature, whereas for the removal of reaction products and other physisorbed species the sample needed to be heated to 200 °C at the end of each ALD cycle, making the process time consuming.

The use of different surface functionalization techniques, such as O_3, NO_2 and plasma treatments, make it possible to deposit uniform dielectric layers by ALD on graphene without the need for thick nucleation layers. When the treatments are performed at a sufficiently low temperature, the reaction with the sp^2 basal plane of graphene can be avoided and the deterioration of the graphene's electrical properties can be minimized or prevented all together. The downside is that the low deposition temperatures generally lead to dielectrics of lower quality being deposited. Performing a few cycles at low temperature to initialize the nucleation on the graphene followed by depositing the remaining material at higher temperatures is an option, but also makes the process time consuming due to the need to cool-down and heat the ALD system between two deposition runs. The need for a low processing temperature can be avoided by the use of a sacrificial functionalized graphene layer, such as GO [79]. Additionally certain precursor chemistries or functionalization methods recover the pristine graphene sp^2 hybridization during ALD, making it possible to directly deposit materials on graphene at elevated temperatures without damage [32]. Moreover, when compared with other graphene surface preparation methods, the surface functionalization techniques have the advantage that they can be done in the same system without breaking the vacuum as is the case for most other deposited seed-layers. This could help to improve the quality of the seed-layer/dielectric interface, since the contamination of the samples with adventitious carbon, due to the exposure to air, is avoided.

2.3.4 Wet Chemistry

Apart from the dry functionalization approaches discussed in the previous section, also wet chemical functionalization has been explored to obtain uniform ALD growth on graphene. Cao *et al.* soaked the graphene in H_2O for approximately 4 h before Al_2O_3 ALD growth. It was found that the Al_2O_3 was uniformly deposited on the graphene, a result attributed to the presence of physisorbed water at the graphene surface. The Al_2O_3 was deposited at a temperature of 200 °C, well above the desorption temperature of H_2O. This would suggest that if the Al_2O_3 deposition is not started quickly the H_2O will desorb from the graphene, which will result in the deposition of discontinuous ALD

films. A similar approach has been used by Zheng *et al*. who exposed the graphene to several H_2O pulses before starting the ALD process at 100 °C [82]. Uniform Al_2O_3 deposition was obtained after ~ 4 nm of Al_2O_3 deposition. Despite the dependence of H_2O pre-treatments on deposition temperature and dwell-time it might have some advantages over, for example, O_3 functionalization. Work by Webber *et al*. indicated that the amount of trapped charges in Al_2O_3 deposited by ALD is reduced for H_2O pretreatments combined with the thermal ALD of Al_2O_3 compared to the O_3 based ALD process [68]. The better performance of the thermal process was attributed to the higher deposition temperature (120 °C vs. 80 °C) leading to a more dense film being deposited. Furthermore, Al_2O_3 prepared using O_3 is known to be oxygen rich due to the incorporation of carbonate groups from incomplete surface reactions. These can possibly act as charge traps.

Garces *et al*. investigated the use of cleaning epitaxial graphene in a HF and/or NH_4OH:H_2O_2 solution to achieve a higher nucleation density of Al_2O_3 on graphene [85]. The HF solution was intended to remove any possible oxides and other impurities from the graphene surface, while the NH_4OH:H_2O_2 treatment created hydroxyl terminated functional groups on the graphene, as confirmed by XPS. The combination of the two treatments led to the uniform deposition of ~ 30 nm Al_2O_3. Hall mobility measurements showed no change in mobility after functionalization and ALD. The dielectric constant of the Al_2O_3 was confirmed to be 7.6, which is lower than on the Si witness samples for which a dielectric constant of 9 was measured. The lower dielectric constant obtained for the Al_2O_3 deposited on graphene was attributed to possible hydroxide and carbide impurities trapped in the film.

The number of wet chemistry approaches investigated to functionalize graphene is limited. Part of this is because the created reactive species on the graphene are physisorbed rather than chemisorbed. Chemisorbed species are more stable but also disrupt the graphene sp^2 configuration, deteriorating its electronic properties. For this reason most wet chemical based approaches rely on increasing the amount of physisorbed species. This makes these methods such as H_2O soaking and H_2O pulsing heavily dependent on the time until ALD is performed and the substrate temperature used during the ALD process. The reproducibility is therefore an important issue for these functionalization methods. However, in the available literature this is rarely discussed. Furthermore, in the case of CVD graphene the adhesion to the underlying substrate is not very good. Submerging graphene in H_2O can therefore lead to the delamination of the graphene from the substrate due to the intercalation of H_2O. The

simplicity of the H_2O treatment methods might still be a viable alternative, but the reproducibility of the method needs further investigation.

2.4 Summary & Prospects

The integration of graphene in optical and electronic devices, often requires the deposition of high-κ dielectrics on graphene. ALD is the method of choice due to its precise thickness control, low deposition temperature and ability to deposit high quality materials uniformly over a large area. The direct ALD on graphene typically results in selective growth on grain boundaries wrinkles and defect sites, caused by a lack of reactive surface sites on graphene's basal plane on which precursors molecules can adsorb. ALD precursor molecules tend to physisorb on graphene instead of forming a chemical bond. The graphene cleanliness and ALD process conditions such as substrate temperature, pump times, purge times and the precursor chemistry strongly affect the deposition uniformity. The appropriate choice of precursor, dose and purge times as well as a low deposition temperature and suitable underlying substrate (e.g. Cu) can increase the ALD nucleation on pristine graphene. However, for many applications the substrate material is a given, and the choice of precursors molecules is often limited. Decreasing the substrate temperature likely also decreases the quality of the material being deposited and thus a tradeoff must be made. Furthermore, the strong dependence on process conditions might affect process reproducibility. To avoid making this compromise and increase process reproducibility seed-layers or surface functionalization can be used for ALD of uniform films on graphene.

Polymer, metal and metal-oxide seed-layers make it possible to deposit uniform films by ALD on graphene. Polymer buffer layers avoid damage to the graphene but can unintentionally dope it, shifting the charge neutrality point far beyond realistic device operating regimes. Furthermore, the low dielectric constant of the polymers used and relative high thickness of the polymer/dielectric stack make dielectric scaling difficult. The deposition of metal and metal-oxide seed-layers often deteriorate graphene's electrical properties due to deposition induced damage. In addition scattering of charge carriers in the graphene can be increased due to the incomplete oxidation of the metal seed-layer, leading to a decrease in charge carrier mobility.

The use of surface functionalization techniques makes it possible to deposit uniform dielectrics on graphene by ALD. The functional groups act as ALD precursor adsorption sites, increasing the deposition uniformity. The creation of these groups can lead to the conversion of sp^2 carbon bonds to sp^3 carbon, disrupting the graphene basal

plane and deteriorating its properties. However, when the functionalization temperature is sufficiently low, the disruption of the sp^2 carbon bonds of the graphene can be avoided because the functionalization proceeds via physisorption instead of chemisorption. This means that the ALD temperature needs to be kept low as well to avoid the desorption of the physisorbed functional groups. The lower deposition temperature conversely results in dielectrics of lower quality being deposited. Increasing the deposition temperature after the first few cycles is an option, but makes the process elaborate. Similarly, the wet chemistry functionalization approaches enhance the ALD nucleation by increasing the amount of physisorbed species on the graphene. Physisorbed species are, however, less stable on the graphene surface compared to chemisorbed ones. Reproducibility can therefore be an issue.

The use of a sacrificial graphene layer that protects the underlying graphene during functionalization might also be an option. In this case the conversion of sp^2 to sp^3 bonds only takes place on the top layer and ALD can be performed at higher temperatures. Reversible H_2 plasma functionalization provides a satisfactory compromise in which the graphene is functionalized directly but the sp^2 hybridization of graphene is recovered after ALD due to the abstraction of the functional groups during the ALD process.

The overview given in this chapter indicates that there are many possibilities to grow dielectrics on graphene by ALD uniformly, each methods having its advantages and disadvantages. In the ideal case one would like to have a method that enables direct uniform ALD growth on graphene without damage to the graphene at a sufficiently high temperature to produce a high quality dielectric. The functionalization of graphene by a reversible plasma treatment or the like and/or increasing the ALD precursor dose times offer the best opportunities from an experimental point of view. These are relatively easy to implement and many ALD systems are equipped with a plasma source. The use of a sacrificial layer also works well but is relatively time consuming due to the additional graphene transfer step. In all three cases the functionalization and further ALD processing can be done in the same system at a constant temperature, without the need for additional equipment or breaking the vacuum in-between functionalization and dielectric deposition.

Apart from the deposition of high-κ dielectric materials by ALD, the uniform deposition of metals on graphene is also of interest, for example for the fabrication of metal-graphene contacts by ALD. In this case the damage to the graphene observed for plasma functionalization or other functionalization methods to initialize the growth might be beneficial. It has been shown for evaporated contacts that plasma treatments can improve the metal-graphene interaction [99–101]. So both uniform ALD nucleation

and a better metal-graphene contact might be achievable when combining plasma functionalization with metal ALD. Recently, Thissen *et al*. have shown that using an e-beam induced deposited (EBID) seed-layer of Pt, a film of Pt can be grown uniformly on graphene. Fabricated devices with EBID-ALD deposited contacts showed high quality Pt-graphene contacts, likely due to the improved Pt-graphene interaction achieved by the EBID Pt seed-layer [102]. Despite the significant advances in ALD materials on graphene over the past few years further improvements and innovations are still required. Especially increasing the dielectric layer quality while maintaining uniform ALD growth will prove essential to the further improvement of device performance and the reduction of EOT. A better understanding of the chemistry behind the functionalization and subsequent ALD process will be vital to achieve this.

Acknowledgements

This work is part of the research program (Projektruimte: 12PR3101) of the Foundation for Fundamental Research on Matter (FOM), which is part of the Netherlands Organization for Scientific Research (NWO).

References

1. Geim, A.K., and Novoselov, K.S. (2007) The rise of graphene. *Nat. Mater.*, **6** (3), 183–191.

2. Xia, F., Farmer, D.B., Lin, Y., and Avouris, P. (2010) Graphene Field-Effect Transistors with High On/Off Current Ratio and Large Transport Band Gap at Room Temperature. *Nano Lett.*, **10** (2), 715–718.

3. Schwierz, F. (2010) Graphene transistors. *Nat. Nanotechnol.*, **5** (7), 487–496.

4. Smith, W.F., and Hashemi, J. (2005) *Foundations of materials science and engineering*, McGraw-Hill, Boston.

5. Cheol Shin, W., Yong Kim, T., Sul, O., and Jin Cho, B. (2012) Seeding atomic layer deposition of high-κ dielectric on graphene with ultrathin poly(4-vinylphenol) layer for enhanced device performance and reliability. *Appl. Phys. Lett.*, **101** (3), 33507.

6. Sangwan, V.K., Jariwala, D., Filippone, S.A., et al. (2013) Quantitatively Enhanced Reliability and Uniformity of High-κ Dielectrics on Graphene Enabled by Self-Assembled Seeding Layers. *Nano Lett.*, **13** (3), 1162–1167.

7. Popinciuc, M., Józsa, C., Zomer, P.J., et al. (2009) Electronic spin transport in graphene field-effect transistors. *Phys. Rev. B*, **80** (21), 214427.

8. Martin, M.-B., Dlubak, B., Weatherup, R.S., et al. (2014) Sub-nanometer Atomic Layer Deposition for Spintronics in Magnetic Tunnel Junctions Based on Graphene Spin-Filtering Membranes. *ACS Nano*, **8** (8), 7890–7895.

9. Banerjee, S., Register, L., Tutuc, E., et al. (2009) Bilayer PseudoSpin Field-Effect Transistor (BiSFET): A Proposed New Logic Device. *IEEE Electron Device Lett.*, **30** (2), 158–160.

10. Kim, S., Nah, J., Jo, I., et al. (2009) Realization of a high mobility dual-gated graphene field-effect transistor with Al_2O_3 dielectric. *Appl. Phys. Lett.*, **94** (6), 62107.

11. Lemme, M.C., Li, L., Palacios, T., and Schwierz, F. (2014) Two-dimensional materials for electronic applications. *MRS Bull.*, **39** (8), 711–718.

12. Pakkala, A., and Putkonen, M. (2010) Atomic Layer Deposition, in *Handbook of Deposition Technologies for Films and Coatings*, Elsevier, pp. 364–391.

13. Ni, Z.H., Wang, H.M., Ma, Y., et al. (2008) Tunable Stress and Controlled

Thickness Modification in Graphene by Annealing. *ACS Nano*, **2** (5), 1033–1039.

14. Wang, X., Tabakman, S.M., and Dai, H. (2008) Atomic Layer Deposition of Metal Oxides on Pristine and Functionalized Graphene. *J. Am. Chem. Soc.*, **130** (26), 8152–8153.

15. Kim, K., Lee, H.-B.-R., Johnson, R.W., et al. (2014) Selective metal deposition at graphene line defects by atomic layer deposition. *Nat. Commun.*, **5**, 4781.

16. Karasulu, B., Vervuurt, R.H.J., Kessels, W.M.M., and Bol, A.A. (2016) Continuous and ultrathin platinum films on graphene using atomic layer deposition: a combined computational and experimental study. *Nanoscale*, **8** (47), 19829–19845.

17. Liao, L., and Duan, X. (2010) Graphene–dielectric integration for graphene transistors. *Mater. Sci. Eng. R Reports*, **70** (3–6), 354–370.

18. Garces, N.Y., Wheeler, V.D., and Gaskill, D.K. (2012) Graphene functionalization and seeding for dielectric deposition and device integration. *J. Vac. Sci. Technol. B Microelectron. Nanom. Struct.*, **30** (3), 30801.

19. Kim, J., and Jandhyala, S. (2013) Atomic layer deposition of dielectrics for carbon-based electronics. *Thin Solid Films*, **546**, 85–93.

20. Marichy, C., and Pinna, N. (2013) Carbon-nanostructures coated/decorated by atomic layer deposition: Growth and applications. *Coord. Chem. Rev.*, **257** (23–24), 3232–3253.

21. Oh, I.-K., Tanskanen, J., Jung, H., et al. (2015) Nucleation and Growth of the HfO_2 Dielectric Layer for Graphene-Based Devices. *Chem. Mater.*, **27** (17), 5868–5877.

22. Aria, A.I., Nakanishi, K., Xiao, L., et al. (2016) Parameter Space of Atomic Layer Deposition of Ultrathin Oxides on Graphene. *ACS Appl. Mater. Interfaces*, **8** (44), 30564–30575.

23. Xuan, Y., Wu, Y.Q., Shen, T., et al. (2008) Atomic-layer-deposited nanostructures for graphene-based nanoelectronics. *Appl. Phys. Lett.*, **92** (1), 13101.

24. Lee, B., Park, S., Kim, H.-C., et al. (2008) Conformal Al_2O_3 dielectric layer deposited by atomic layer deposition for graphene-based nanoelectronics. *Appl. Phys. Lett.*, **92** (20), 203102.

25. Speck, F., Ostler, M., Röhrl, J., et al. (2010) Atomic layer deposited aluminum

oxide films on graphite and graphene studied by XPS and AFM. *Phys. status solidi*, **7** (2), 398–401.

26. Dlubak, B., Kidambi, P.R., Weatherup, R.S., et al. (2012) Substrate-assisted nucleation of ultra-thin dielectric layers on graphene by atomic layer deposition. *Appl. Phys. Lett.*, **100** (17), 173113.

27. Edwards, R.S., and Coleman, K.S. (2013) Graphene synthesis: relationship to applications. *Nanoscale*, **5** (1), 38–51.

28. Li, X., Meng, X., Liu, J., et al. (2012) Tin Oxide with Controlled Morphology and Crystallinity by Atomic Layer Deposition onto Graphene Nanosheets for Enhanced Lithium Storage. *Adv. Funct. Mater.*, **22** (8), 1647–1654.

29. Ban, C., Xie, M., Sun, X., et al. (2013) Atomic layer deposition of amorphous TiO_2 on graphene as an anode for Li-ion batteries. *Nanotechnology*, **24** (42), 424002.

30. Yu, M., Wang, A., Wang, Y., et al. (2014) An alumina stabilized ZnO–graphene anode for lithium ion batteries via atomic layer deposition. *Nanoscale*, **6** (19), 11419–11424.

31. Novoselov, K.S., Geim, A.K., Morozov, S. V., et al. (2004) Electric Field Effect in Atomically Thin Carbon Films. *Science*, **306** (5696), 666–669.

32. Vervuurt, R.H.J., Karasulu, B., Verheijen, M.A., et al. (2017) Uniform Atomic Layer Deposition of Al_2O_3 on Graphene by Reversible Hydrogen Plasma Functionalization. *Chem. Mater.*, **29** (5), 2090–2100.

33. Cao, Y.-Q., Cao, Z.-Y., Li, X., et al. (2014) A facile way to deposit conformal Al_2O_3 thin film on pristine graphene by atomic layer deposition. *Appl. Surf. Sci.*, **291**, 78–82.

34. Van Lam, D., Kim, S.-M., Cho, Y., et al. (2014) Healing defective CVD-graphene through vapor phase treatment. *Nanoscale*, **6** (11), 5639.

35. Kim, J., Kim, S., and Jung, W. (2016) Selective atomic layer deposition onto directly transferred monolayer graphene. *Mater. Lett.*, **165**, 45–49.

36. Zou, K., Hong, X., Keefer, D., and Zhu, J. (2010) Deposition of High-Quality HfO_2 on Graphene and the Effect of Remote Oxide Phonon Scattering. *Phys. Rev. Lett.*, **105** (12), 126601.

37. Meric, I., Han, M.Y., Young, A.F., et al. (2008) Current saturation in zero-bandgap, top-gated graphene field-effect transistors. *Nat. Nanotechnol.*, **3** (11), 654–659.

38. Robinson, J.A., LaBella, M., Trumbull, K.A., et al. (2010) Epitaxial Graphene Materials Integration: Effects of Dielectric Overlayers on Structural and Electronic Properties. *ACS Nano*, **4** (5), 2667–2672.

39. Park, K.S., Kim, S., Kim, H., et al. (2015) Wafer-scale single-domain-like graphene by defect-selective atomic layer deposition of hexagonal ZnO. *Nanoscale*, **7** (42), 17702–17709.

40. Tamm, A., Kozlova, J., Aarik, L., et al. (2014) Atomic layer deposition of ZrO_2 for graphene-based multilayer structures: In situ and ex situ characterization of growth process. *Phys. Status Solidi a-Applications Mater. Sci.*, **211** (2), 397–402.

41. Fisichella, G., Schilirò, E., Di Franco, S., et al. (2017) Interface Electrical Properties of Al_2O_3 Thin Films on Graphene Obtained by Atomic Layer Deposition with an in Situ Seedlike Layer. *ACS Appl. Mater. Interfaces*, acsami.6b15190.

42. Park, Y.H., Kim, M.H., Kim, S. Bin, et al. (2016) Enhanced Nucleation of High-κ Dielectrics on Graphene by Atomic Layer Deposition. *Chem. Mater.*, **28** (20), 7268–7275.

43. Liu, R., Peng, M., Zhang, H., et al. (2016) Atomic layer deposition of ZnO on graphene for thin film transistor. *Mater. Sci. Semicond. Process.*, **56** (July), 324–328.

44. Alaboson, J.M.P., Wang, Q.H., Emery, J.D., et al. (2011) Seeding Atomic Layer Deposition of High-κ Dielectrics on Epitaxial Graphene with Organic Self-Assembled Monolayers. *ACS Nano*, **5** (6), 5223–5232.

45. Kitzmann, J., Göritz, A., Fraschke, M., et al. (2016) Perfluorodecyltrichlorosilane-based seed-layer for improved chemical vapour deposition of ultrathin hafnium dioxide films on graphene. *Sci. Rep.*, **6** (April), 29223.

46. Han, K.S., Kalode, P.Y., Koo Lee, Y.-E., et al. (2016) A non-destructive n-doping method for graphene with precise control of electronic properties via atomic layer deposition. *Nanoscale*, **8** (9), 5000–5005.

47. Jeon, J.H., Jerng, S.-K., Akbar, K., and Chun, S.-H. (2016) Hydrophobic Surface Treatment and Interrupted Atomic Layer Deposition for Highly Resistive Al_2O_3 Films on Graphene. *ACS Appl. Mater. Interfaces*, **8** (43), 29637–29641.

48. Park, J.H., Movva, H.C.P., Chagarov, E., et al. (2015) In Situ Observation of Initial Stage in Dielectric Growth and Deposition of Ultrahigh Nucleation

Density Dielectric on Two-Dimensional Surfaces. *Nano Lett.*, **15** (10), 6626–6633.

49. Farmer, D.B., Chiu, H.-Y., Lin, Y.-M., et al. (2009) Utilization of a Buffered Dielectric to Achieve High Field-Effect Carrier Mobility in Graphene Transistors. *Nano Lett.*, **9** (12), 4474–4478.

50. Lin, Y.-M., Dimitrakopoulos, C., Jenkins, K.A., et al. (2010) 100-GHz Transistors from Wafer-Scale Epitaxial Graphene. *Science*, **327** (5966), 734–734.

51. Jeong, S.-J., Gu, Y., Heo, J., et al. (2016) Thickness scaling of atomic-layer-deposited HfO_2 films and their application to wafer-scale graphene tunnelling transistors. *Sci. Rep.*, **6** (January), 20907.

52. Meric, I., Dean, C.R., Young, A.F., et al. (2011) Channel Length Scaling in Graphene Field-Effect Transistors Studied with Pulsed Current−Voltage Measurements. *Nano Lett.*, **11** (3), 1093–1097.

53. Pirkle, A., Wallace, R.M., and Colombo, L. (2009) In situ studies of Al_2O_3 and HfO_2 dielectrics on graphite. *Appl. Phys. Lett.*, **95** (13), 133106.

54. Farmer, D.B., Lin, Y.-M., and Avouris, P. (2010) Graphene field-effect transistors with self-aligned gates. *Appl. Phys. Lett.*, **97** (1), 13103.

55. Fallahazad, B., Lee, K., Lian, G., et al. (2012) Scaling of Al_2O_3 dielectric for graphene field-effect transistors. *Appl. Phys. Lett.*, **100** (9), 93112.

56. Sagade, A.A., Neumaier, D., Schall, D., et al. (2015) Highly air stable passivation of graphene based field effect devices. *Nanoscale*, **7** (8), 3558–3564.

57. Shen, T., Gu, J.J., Xu, M., et al. (2009) Observation of quantum-Hall effect in gated epitaxial graphene grown on SiC (0001). *Appl. Phys. Lett.*, **95** (17), 172105.

58. Hopf, T., Vassilevski, K. V., Escobedo-Cousin, E., et al. (2014) Dirac point and transconductance of top-gated graphene field-effect transistors operating at elevated temperature. *J. Appl. Phys.*, **116** (15), 154504.

59. Hollander, M.J., LaBella, M., Hughes, Z.R., et al. (2011) Enhanced Transport and Transistor Performance with Oxide Seeded High-κ Gate Dielectrics on Wafer-Scale Epitaxial Graphene. *Nano Lett.*, **11** (9), 3601–3607.

60. Fallahazad, B., Kim, S., Colombo, L., and Tutuc, E. (2010) Dielectric thickness dependence of carrier mobility in graphene with HfO_2 top dielectric. *Appl. Phys.*

Lett., **97** (12), 123105.

61. Hsu, A., Wang, H., Kim, K.K., et al. (2011) High Frequency Performance of Graphene Transistors Grown by Chemical Vapor Deposition for Mixed Signal Applications. *Jpn. J. Appl. Phys.*, **50** (7), 70114.

62. Lee, B., Mordi, G., Park, T., et al. (2009) Atomic-Layer-Deposited Al_2O_3 as Gate Dielectrics for Graphene-Based Devices. *ECS Trans.*, **94** (21), 225–230.

63. McDonnell, S., Pirkle, A., Kim, J., et al. (2012) Trimethyl-aluminum and ozone interactions with graphite in atomic layer deposition of Al_2O_3. *J. Appl. Phys.*, **112** (10), 104110.

64. Lee, G., Lee, B., Kim, J., and Cho, K. (2009) Ozone Adsorption on Graphene: Ab Initio Study and Experimental Validation. *J. Phys. Chem. C*, **113** (32), 14225–14229.

65. Pirkle, A., McDonnell, S., Lee, B., et al. (2010) The effect of graphite surface condition on the composition of Al_2O_3 by atomic layer deposition. *Appl. Phys. Lett.*, **97** (8), 3–6.

66. Lee, B., Mordi, G., Kim, M.J., et al. (2010) Characteristics of high-κ Al_2O_3 dielectric using ozone-based atomic layer deposition for dual-gated graphene devices. *Appl. Phys. Lett.*, **97** (4), 43107.

67. Jandhyala, S., Mordi, G., Lee, B., et al. (2012) Atomic Layer Deposition of Dielectrics on Graphene Using Reversibly Physisorbed Ozone. *ACS Nano*, **6** (3), 2722–2730.

68. Alexander-Webber, J.A., Sagade, A.A., Aria, A.I., et al. (2016) Encapsulation of graphene transistors and vertical device integration by interface engineering with atomic layer deposited oxide. *2D Mater.*, **4** (1), 11008.

69. Young, M.J., Musgrave, C.B., and George, S.M. (2015) Growth and Characterization of Al_2O_3 Atomic Layer Deposition Films on sp^2 -Graphitic Carbon Substrates Using NO_2 /Trimethylaluminum Pretreatment. *ACS Appl. Mater. Interfaces*, **7** (22), 12030–12037.

70. Lin, Y.-M., Jenkins, K.A., Valdes-Garcia, A., et al. (2009) Operation of Graphene Transistors at Gigahertz Frequencies. *Nano Lett.*, **9** (1), 422–426.

71. Williams, J.R., DiCarlo, L., and Marcus, C.M. (2007) Quantum Hall Effect in a Gate-Controlled p-n Junction of Graphene. *Science*, **317** (5838), 638–641.

72. Wang, L., Travis, J.J., Cavanagh, A.S., et al. (2012) Ultrathin Oxide Films by Atomic Layer Deposition on Graphene. *Nano Lett.*, **12** (7), 3706–3710.

73. Lim, T., Kim, D., and Ju, S. (2013) Direct deposition of aluminum oxide gate dielectric on graphene channel using nitrogen plasma treatment. *Appl. Phys. Lett.*, **103** (1), 13107.

74. Nayfeh, O.M., Marr, T., and Dubey, M. (2011) Impact of Plasma-Assisted Atomic-Layer-Deposited Gate Dielectric on Graphene Transistors. *IEEE Electron Device Lett.*, **32** (4), 473–475.

75. Tang, X., Reckinger, N., Poncelet, O., et al. (2015) Damage evaluation in graphene underlying atomic layer deposition dielectrics. *Sci. Rep.*, **5**, 13523.

76. Tang, X., Reckinger, N., Poncelet, O., et al. (2014) Using top graphene layer as sacrificial protection during dielectric atomic layer deposition. *arXiv.org, e-Print Arch. Condens. Matter*, 1–15, arXiv:1403.3787v1 [cond–mtrl-sci].

77. Nourbakhsh, A., Adelmann, C., Song, Y., et al. (2015) Graphene oxide monolayers as atomically thin seeding layers for atomic layer deposition of metal oxides. *Nanoscale*, **7** (24), 10781–10789.

78. Shin, W.C., Bong, J.H., Choi, S.-Y., and Cho, B.J. (2013) Functionalized Graphene as an Ultrathin Seed Layer for the Atomic Layer Deposition of Conformal High-k Dielectrics on Graphene. *ACS Appl. Mater. Interfaces*, **5** (22), 11515–11519.

79. Nath, A., Kong, B.D., Koehler, A.D., et al. (2017) Universal conformal ultrathin dielectrics on epitaxial graphene enabled by a graphene oxide seed layer. *Appl. Phys. Lett.*, **110** (1), 13106.

80. Johns, J.E., Alaboson, J.M.P., Patwardhan, S., et al. (2013) Metal Oxide Nanoparticle Growth on Graphene via Chemical Activation with Atomic Oxygen. *J. Am. Chem. Soc.*, **135** (48), 18121–18125.

81. Wheeler, V., Garces, N., Nyakiti, L., et al. (2012) Fluorine functionalization of epitaxial graphene for uniform deposition of thin high-κ dielectrics. *Carbon N. Y.*, **50** (6), 2307–2314.

82. Zheng, L., Cheng, X., Cao, D., et al. (2014) Improvement of Al_2O_3 Films on Graphene Grown by Atomic Layer Deposition with Pre-H_2O Treatment. *ACS Appl. Mater. Interfaces*, **6** (10), 7014–7019.

83. Zheng, L., Cheng, X., Yu, Y., et al. (2015) Controlled direct growth of Al_2O_3 - doped HfO_2 films on graphene by H_2O-based atomic layer deposition. *Phys. Chem. Chem. Phys.*, **17** (5), 3179–3185.

84. Jiao, K., Wu, X., Duan, C., et al. (2015) Novel ALD-assisted growth of ZnO nanorods on graphene and its $Cu_2ZnSn(S_xSe_{1-x})_4$ solar cell application. *Phys.*

Chem. Chem. Phys., **17** (6), 4757–4762.

85. Garces, N.Y., Wheeler, V.D., Hite, J.K., et al. (2011) Epitaxial graphene surface preparation for atomic layer deposition of Al2O3. *J. Appl. Phys.*, **109** (12), 124304.

86. Zhang, Y., Fu, Q., Cui, Y., et al. (2013) Enhanced reactivity of graphene wrinkles and their function as nanosized gas inlets for reactions under graphene. *Phys. Chem. Chem. Phys.*, **15** (43), 19042.

87. Wu, Q., Wu, Y., Hao, Y., et al. (2013) Selective surface functionalization at regions of high local curvature in graphene. *Chem. Commun.*, **49** (7), 677–679.

88. Lin, Y.-C., Lu, C.-C., Yeh, C.-H., et al. (2012) Graphene Annealing: How Clean Can It Be? *Nano Lett.*, **12** (1), 414–419.

89. Färm, E., Kemell, M., Ritala, M., and Leskelä, M. (2008) Selective-Area Atomic Layer Deposition Using Poly(methyl methacrylate) Films as Mask Layers. *J. Phys. Chem. C*, **112** (40), 15791–15795.

90. Dingemans, G., Einsele, F., Beyer, W., et al. (2012) Influence of annealing and Al_2O_3 properties on the hydrogen-induced passivation of the Si/SiO_2 interface. *J. Appl. Phys.*, **111** (9), 93713.

91. Vervuurt, R.H.J., Sharma, A., Jiao, Y., et al. (2016) Area-selective atomic layer deposition of platinum using photosensitive polyimide. *Nanotechnology*, **27** (40), 405302.

92. Zhou, Y., Muhich, C.L., Neltner, B.T., et al. (2012) Growth of Pt Particles on the Anatase TiO_2 (101) Surface. *J. Phys. Chem. C*, **116** (22), 12114–12123.

93. Wynblatt, P., and Gjostein, N.A. (1976) Particle growth in model supported metal catalysts—I. Theory. *Acta Metall.*, **24** (12), 1165–1174.

94. Mackus, A.J.M., Verheijen, M.A., Leick, N., et al. (2013) Influence of Oxygen Exposure on the Nucleation of Platinum Atomic Layer Deposition: Consequences for Film Growth, Nanopatterning, and Nanoparticle Synthesis. *Chem. Mater.*, **25** (9), 1905–1911.

95. Konar, A., Fang, T., and Jena, D. (2010) Effect of high-κ gate dielectrics on charge transport in graphene-based field effect transistors. *Phys. Rev. B*, **82** (11), 115452.

96. Ponomarenko, L.A., Yang, R., Mohiuddin, T.M., et al. (2009) Effect of a High-κ Environment on Charge Carrier Mobility in Graphene. *Phys. Rev. Lett.*, **102** (20), 206603.

97. Farmer, D.B., and Gordon, R.G. (2006) Atomic Layer Deposition on Suspended Single-Walled Carbon Nanotubes via Gas-Phase Noncovalent Functionalization. *Nano Lett.*, **6** (4), 699–703.

98. Tainter, C.J., and Schatz, G.C. (2016) Reactive Force Field Modeling of Zinc Oxide Nanoparticle Formation. *J. Phys. Chem. C*, **120** (5), 2950–2961.

99. Robinson, J.A., LaBella, M., Zhu, M., et al. (2011) Contacting graphene. *Appl. Phys. Lett.*, **98** (5), 53103.

100. Foley, B.M., Hernández, S.C., Duda, J.C., et al. (2015) Modifying Surface Energy of Graphene via Plasma-Based Chemical Functionalization to Tune Thermal and Electrical Transport at Metal Interfaces. *Nano Lett.*, **15** (8), 4876–4882.

101. Yue, D.W., Ra, C.H., Liu, X.C., et al. (2015) Edge contacts of graphene formed by using a controlled plasma treatment. *Nanoscale*, **7** (2), 825–831.

102. Thissen, N.F.W., Vervuurt, R.H.J., Mackus, A.J.M., et al. (2017) Graphene devices with bottom-up contacts by area-selective atomic layer deposition. *2D Mater.*, **4** (2), 25046.

Chapter 3

Uniform Atomic Layer Deposition of Al_2O_3 on Graphene by Reversible Hydrogen Plasma Functionalization*

Abstract

A novel method to form ultrathin, uniform Al_2O_3 layers on graphene using reversible hydrogen plasma functionalization followed by atomic layer deposition (ALD) is presented. ALD on pristine graphene is known to be a challenge due to the absence of dangling bonds, leading to non-uniform film coverage. We show that hydrogen plasma functionalization of graphene leads to uniform ALD of closed Al_2O_3 films down to 8 nm in thickness. Hall measurements and Raman spectroscopy reveal that the hydrogen plasma functionalization is reversible upon Al_2O_3 ALD and subsequent annealing at 400 °C, and in this way does not deteriorate the graphene's charge carrier mobility. This is in contrast with oxygen plasma functionalization, which can lead to a uniform 5 nm thick closed film, but which is not reversible and leads to a reduction of the charge carrier mobility.

Density functional theory (DFT) calculations attribute the uniform growth on both H_2 and O_2 plasma functionalized graphene to the enhanced adsorption of Trimethylaluminum (TMA) on these surfaces. A DFT analysis of the possible reaction pathways for TMA precursor adsorption on hydrogenated graphene predicts a binding mechanism that cleans off the hydrogen functionalities from the surface, which explains the observed reversibility of the hydrogen plasma functionalization upon Al_2O_3 ALD.

*R.H.J. Vervuurt, B. Karasulu, M.A. Verheijen, W.M.M. Kessels & A.A. Bol, *Chemistry of Materials* **29** (2017) 2090.

3.1 Introduction

Graphene is a two-dimensional (2D) material that has attracted significant interest in the scientific community due to its interesting electronic, optical and thermal properties. The high carrier mobility of graphene and large maximum current density make it a promising candidate for post-silicon electronics [1]. The deposition of thin high-κ dielectric films on graphene is required for many of these electronic applications. For example, radio-frequency transistors require the deposition of dielectric layers on top of the graphene for good electrostatic control of the channel and better device reliability [2,3], while lateral spin valves require ultra-thin dielectrics on the graphene as a tunnel barrier [4].

Atomic layer deposition (ALD) is the preferred method to deposit dielectric layers on graphene, due to its ability to deposit high quality and uniform materials with precise control of the layer thickness. However, the initiation of ALD growth on graphene is known to be a challenge due to the lack of out-of-plane bonds and surface hydrophobicity. ALD growth of dielectrics on pristine graphene therefore only occurs on defect sites or grain boundaries where dangling bonds or functional groups are present [5,6]. To overcome this issue different surface preparation techniques to initialize ALD growth on graphene have been investigated in the literature [5–22]. In general these techniques can be divided into three categories: 1) the use of seed-layers, such as self-assembled monolayers, polymers, evaporated metals (which are oxidized in air before ALD) and layers deposited by chemical vapor deposition (CVD) [5,10,22], 2) the creation of functional groups on the graphene surface by for example ozone[11] and plasma [12] treatments and 3) tuning the underlying substrate to enhance the nucleation [13].

The use of polymer seed-layers results in the conformal coverage of ALD oxide without damaging the graphene [5,14,15]. However, the polymer interlayer that is used has a low-κ value, leading to a higher equivalent oxide thickness for the deposited polymer/oxide stack. Furthermore, the used polymers can dope the graphene, which results in a large Dirac-point shift of the created devices [14]. Oxidized metal seed-layers avoid these issues, but trap charges at the graphene-dielectric interface. This deteriorates the mobility of graphene layers and reduces device performance [10]. The use of CVD layers to initialize growth does not affect the graphene properties but no longer offers the advantages of ALD in terms of thickness control, resulting in the deposition of thick layers (> 10 nm) [22].

Degradation of the electrical properties of graphene is also observed for most covalent functionalization methods. This is because these methods rely on the conversion of sp^2 C bonds to sp^3 bonds, disrupting the 2D nature of graphene [11,12,16,17]. For example, ozone functionalization at 200 °C creates epoxy surface groups that enhance the nucleation of Al_2O_3 on graphene, yielding uniform Al_2O_3 growth on the graphene [11]. At the same time, however, these groups enhance the scattering of charge carriers in graphene, resulting in decreased carrier mobilities. To avoid this problem the ozone functionalization can be performed at lower temperatures. At temperatures below 50 °C, ozone is physisorbed on graphene leaving the sp^2 bonding intact. This prevents damaging the graphene and can even provide an improvement in the electrical properties of graphene following Al_2O_3 ALD [18,19]. The limited stability of physisorbed ozone on the graphene surface however, also requires Al_2O_3 deposition at these low temperatures, decreasing the quality of the deposited films [23].

The use of O_2 and N_2 plasmas to functionalize the graphene causes severe damage to the graphene, degrading its electrical properties [12,16]. To avoid this Shin et al. and Nourbakhsh et al. performed an O_2 plasma treatment on a sacrificial graphene layer [20,21]. This layer served as a nucleation layer for Al_2O_3 ALD that was either transferred onto a pristine graphene layer after the plasma exposure [20], or protected the underlying graphene during the plasma exposure [21]. With this method uniform Al_2O_3 layers down to 4 nm in thickness could be deposited without damaging the graphene. The requirement of an additional graphene transfer step, however, makes the process time consuming and could trap polymer residues left over from the transfer procedure in between the layers.

To date H_2 plasmas have not been studied for the uniform growth of dielectric layers by ALD on graphene. The use of H_2 plasmas to initialize growth on graphene might be of interest because the H_2 plasma treatment (hydrogenation) has shown to be reversible [24,25]. The pristine graphene properties can be recovered after annealing the hydrogenated graphene in an Ar atmosphere at 400 °C. This might make it possible to directly grow ALD layers on hydrogen functionalized graphene, without the need for sacrificial layers or damaging the graphene, since the pristine graphene properties might be recovered after processing by an annealing step.

To this extent H_2 plasma pretreatments are investigated in this work to initialize Al_2O_3 ALD growth directly on graphene without the use of a sacrificial layer. The ability of the H_2 plasma pretreatment to obtain uniform ALD growth on graphene is compared to O_2 plasma pretreatments and pristine graphene. The type of functional group created by the H_2 and O_2 plasma treatments is studied by X-ray photoelectron

spectroscopy (XPS). The effects of the plasma treatments on the structural and electrical properties of the functionalized graphene is investigated by Raman and Hall measurements, before and after plasma treatment, after Al_2O_3 ALD, and after an anneal at 400 °C. Furthermore, the underlying reaction mechanism of the Al_2O_3 precursor adsorption on the functionalized graphene is investigated using *ab inito* calculations.

3.2 Methodology

3.2.1 Experimental Methods

Graphene samples (1x1 cm^2) were synthesized by CVD on Cu foil (Alfa Aesar 99.8%, No. 13382) of 25 μm. Before growth the Cu foil was cleaned using acetone, methanol and a 30 s 1.0 M nitric acid (HNO_3) etch to remove the surface oxide. After rinsing in deionized water the Cu foil was dried and loaded into a tube furnace. The Cu foil was heated to 1050 °C under an Ar/H_2 (500/10 sccm) flow at a pressure of 0.4 Torr. After annealing the sample for 30 min, the H_2 flow was reduced to 6 sccm and 100 sccm CH_4 was added to the gas flow for 20 min, resulting in a monolayer coverage of graphene on the Cu foil. The sample was cooled down to room temperature in 15 min while leaving the gas flows on.

The graphene on Cu was transferred to 90 nm SiO_2/Si (100) wafers by wet chemistry using poly(methyl methacrylate) (PMMA) A4 950k (Micro Chem.) as a support layer. Ferric chloride ($FeCl_3$ 0.1 M) was used to etch the Cu. After transfer the PMMA was removed using acetone with a final rinse in methanol. The samples were subsequently annealed at 400 °C in an Ar/H_2 atmosphere for 2 h, to minimize any PMMA residue remaining after PMMA lift-off.

The O_2 and H_2 plasma functionalization of the graphene was performed in an Oxford Instruments FlexAl reactor using a 100 W 50 mTorr plasma at 50 °C and a gas flow of 50 sccm O_2 or H_2, respectively. ALD was performed in the same reactor at 100 °C using trimethylaluminum (TMA) and H_2O. The timing sequence was as follows: (0.03 s, 4 s, 0.2 s, 10 s), (TMA, purge, H_2O, purge). After ALD one set of samples was annealed at 400 ºC in an Ar/H_2 atmosphere for 2 h in a tube furnace.

The quality and electrical properties of the graphene samples were characterized before and after plasma treatment following ALD and after annealing with a Renishaw Invia Raman microscope (514.5 nm) and an Ecopia HMS-5300 Hall Effect Measurement System. The graphene samples used for the Hall-measurements were approximately 1x1 cm^2 in size. Ohmic contact to the graphene was obtained by applying

conductive silver paste at the corners of the graphene samples. The silver paint was applied before annealing the pristine graphene samples at 400 °C to exclude the influence of the annealing process on the contact formation. The formation of an Ohmic contact was confirmed by *I-V* measurements, which showed Ohmic behavior over the full measured range (-100-100 μA). The Hall measurements were performed at 25 °C under N_2 ambient. Prior to the measurements the samples were annealed at 150 °C for 10 min to remove any adsorbed H_2O from the graphene. Information on the surface groups created after plasma treatment was determined by a Thermo Scientific K-Alpha KA 1066 X-ray photon spectroscope (XPS). The uniformity of the deposited Al_2O_3 films was determined with a JEOL 7500 FA scanning electron microscope (SEM), a NT-MDT Solver P47 atomic force microscope (AFM), and a JEOL ARM 200 probe corrected transmission electron microscope (TEM), operated at 200 kV. A cross-sectional TEM sample from a Al_2O_3/graphene stack on a 90 nm SiO_2/Si wafer was prepared using the FIB lift-out method using a FEI Helios 650 DualBeam system. The thickness of the Al_2O_3 layer was determined by a J.A. Woollam M-2000D variable angle spectroscopic ellipsometer (SE).

3.2.2 Computational Methods

The binding energies of TMA on pristine, O_2 and H_2 plasma functionalized graphene were calculated by *ab initio* density functional theory (DFT). The calculations were performed using the projector augmented wavefunction (PAW) [26,27] as implemented in Vienna Ab Initio Simulation Package (*VASP* v.5.3.5) [28–31]. The generalized gradient approximation (GGA) to DFT [32,33] was used with a plane-wave basis. The Perdew−Burke−Ernzerhof (PBE) exchange correlation functional [34,35] was used along with the DFT(PBE)-D3 method including the Becke-Jonson damping [36] to account for van der Waals interactions on an empirical basis. Eq. 3.1 was used for computing the TMA adsorption (or, equivalently, binding) energies through physisorption (ΔE_p) or chemisorption (ΔE_c) on a given graphene surface:

$$\Delta E_{p/c} = E_{PG} - E_P - E_G \tag{3.1}$$

where E_{PG} is the total energy of the physisorbed/chemisorbed complex of the TMA precursor with graphene, E_P and E_G are the (gas phase) total energies of the isolated precursor and the graphene surface under consideration. Relevantly, the (reaction) energies ($\Delta E_r = \Delta E_c - \Delta E_p$) required for converting the corresponding physisorbed species

into chemisorbed ones, e.g. via dissociation of the given precursor on the given surface, are also presented. Gibbs free energy changes ($\Delta G = \Delta(\underline{E}_{elec} + E_{ZPE})$-$T\Delta S$) associated with TMA adsorption were estimated in the ideal gas limit at the typical ALD conditions (T = 100 °C and P = 100 mTorr), accounting for the translational, rotational and vibrational contributions to the enthalpy and entropy terms. All-atom vibrational analyses were performed using the finite differences method implemented in *VASP*. Further details about the computational calculations can be found elsewhere [37,38].

3.3 Results and Discussion

3.3.1 Surface Species Analysis by XPS

First the effect of the O_2 and H_2 plasma functionalization on graphene was studied by XPS to analyze the surface groups created during the plasma exposure. Before plasma exposure, the pristine graphene samples were annealed at 400 °C for 2 h in Ar/H_2 (5%) atmosphere for 2 h. This was done to minimize any polymer residues left on the surface after transfer, and ensure the cleanest graphene possible. In the case of the O_2 plasma treatment an exposure time of 30 s was chosen, while for the H_2 plasma 35 s was used, both at a pressure of 50 mTorr and plasma power of 100 W. These are the optimal exposure times; longer exposures resulted in irreversibly damaging the graphene as confirmed by Raman spectroscopy, whereas shorter exposures did not result in a closed Al_2O_3 layer (see Appendix A).

The XPS measurements of the C 1s spectra of graphene after 30 s O_2 plasma treatment and 35 s H_2 plasma treatment are shown in Figure 3.1. As a reference the spectrum of pristine graphene after transfer to 90 nm SiO_2 and 400 °C anneal is also shown in Figure 3.1. The main peak contributing to the C 1s spectrum of pristine graphene (Figure 3.1a) is located at 284.4 eV and originates from the sp^2 bonding of the carbon atoms. The weak peak at 286.4 eV corresponds to C-O bonding. These C-O bonds are commonly seen on the graphene basal plane, and originate from grain boundaries or defects sites [39,40] or are the result of polymer residues remaining on the graphene after its transfer to SiO_2 and annealing [41]. In addition, two plasmon loss features observed at 290.4 eV and 293.2 eV are caused by the interaction of the photoelectron with free electrons present in the graphene [42].

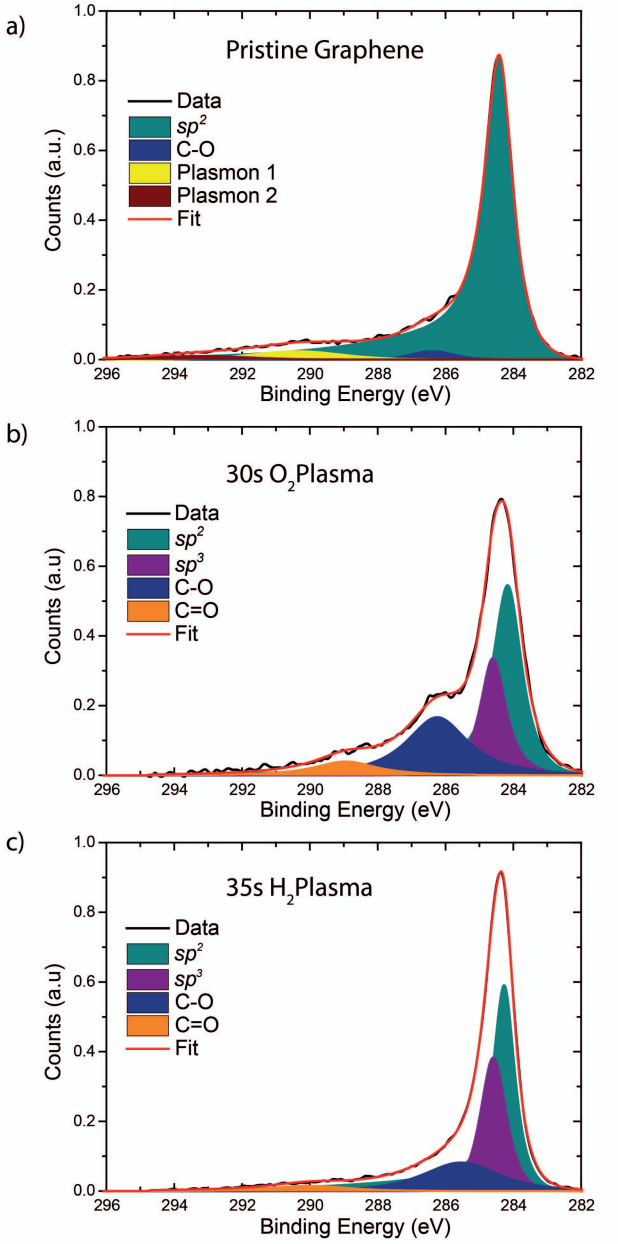


Figure 3.1: XPS spectra of the core level C 1s of a) pristine graphene (after transfer to SiO_2), b) graphene after 30 s O_2 plasma treatment and c) graphene after 35 s H_2 plasma treatment at a pressure of 50 mTorr and a plasma power of 100 W.

After a 30 s O_2 plasma treatment (Figure 3.1b) the amount of C-O bonds increases, indicating the creation of epoxide groups (C-O-C) or hydroxide (C-OH) containing surface groups on the graphene. Two additional peaks appear in the spectrum compared to that of pristine graphene. The peak at 284.6 eV is related to sp^3 bonding of the carbon atoms. This is combined with a decrease in sp^2 bonding, which indicates that the O_2 plasma treatment indeed disrupts the sp^2 structure of the graphene [42]. The second peak appears at 289.0 eV and is related to the creation of C=O bonds, possibly in the form of carbonyl groups. Since carbonyl groups can only be formed in-plane due to their sp^2 carbon constituent, these are most likely located at defects or edge sites of the graphene basal plane. The plasmon loss features can no longer be observed after the O_2 plasma treatment. This is likely due to the deterioration of the electrical properties of the graphene after the plasma exposure. The O 1s spectra of the graphene samples did not provide any additional information on the C-O and C=O bonding due to the dominating contribution from the SiO_2 substrate to the O 1s signal.

After a 35 s H_2 plasma treatment (Figure 3.1c) the graphene shows a strong increase in the sp^3 bonding, combined with a decrease in the sp^2 bonding. This is most likely related to the formation of C-H bonds (hydrogenated graphene) [24], which cannot be observed by XPS. A distinct hallmark of hydrogenated graphene is the reversibility of hydrogenation upon annealing at 400 °C [25]. This reversibility can be confirmed by Raman spectroscopy [24,25]. After hydrogenation the Raman D-band at 1350 cm^{-1}, which is related to defects or sp^3 bonding of the carbon atoms, can be observed. This band disappears after annealing at 400 °C in Ar atmosphere, indicating that hydrogen atoms desorb form the graphene surface at this temperature and the original graphene sp^2 configuration is restored. This reversibility of the D-band is also observed for the 35 s H_2 plasma treated sample in this work (see below), indicating that the graphene is indeed hydrogenated upon H_2 plasma exposure.

Apart from a change from sp^2 to sp^3 bonding the XPS also shows an increase in the C-O bonding after the H_2 plasma treatment. This could be due to the formation of hydroxyl groups upon H_2 plasma exposure or adventitious carbon. The hydroxyl groups could be formed by residual water desorbing from the reactor walls and dissociating in the plasma, whereas the adventitious carbon could be formed due to carbon containing molecules present in the air adsorbing on the sample during transfer to the XPS system. Summarizing, the XPS results indicate that an O_2 plasma creates a combination of epoxide, hydroxide, and carbonyl groups on the graphene surface. A hydrogen plasma most likely results in the creation of C-H groups with some hydroxyl impurities.

3.3.2 Al_2O_3 ALD Growth on Functionalized Graphene

To investigate the effect of the created functional groups on the uniformity of the Al_2O_3 nucleation, 100 ALD cycles were performed on the plasma treated samples. A pristine graphene sample was added to the deposition as a reference. The uniformity of the Al_2O_3 after deposition, determined by SEM and AFM, is shown in Figure 3.2. On the pristine graphene reference sample no uniform growth is obtained (Figure 3.2a,d). Small holes and a granular Al_2O_3 structure are visible in both the AFM and SEM images. The roughness, determined from an average of three AFM scans (2x2 μm^2), is 1.9 ± 0.1 nm for the pristine graphene sample after Al_2O_3 ALD. Both the 30 s O_2 plasma (Figure 3.2b,e) and the 35 s H_2 plasma (Figure 3.2c,f) treated graphene show uniform deposition of Al_2O_3. No pinholes are visible and the roughness is considerably lower, 0.39 ± 0.05 nm and 0.45 ± 0.05 nm for the O_2 and H_2 plasma, respectively, indicating that a closed Al_2O_3 layer is obtained. The surface groups created on the graphene with the O_2 and H_2 plasma pretreatments thus sufficiently increase the ALD precursor adsorption on graphene, enhancing the nucleation of Al_2O_3 ALD and enabling uniform Al_2O_3 growth on graphene.

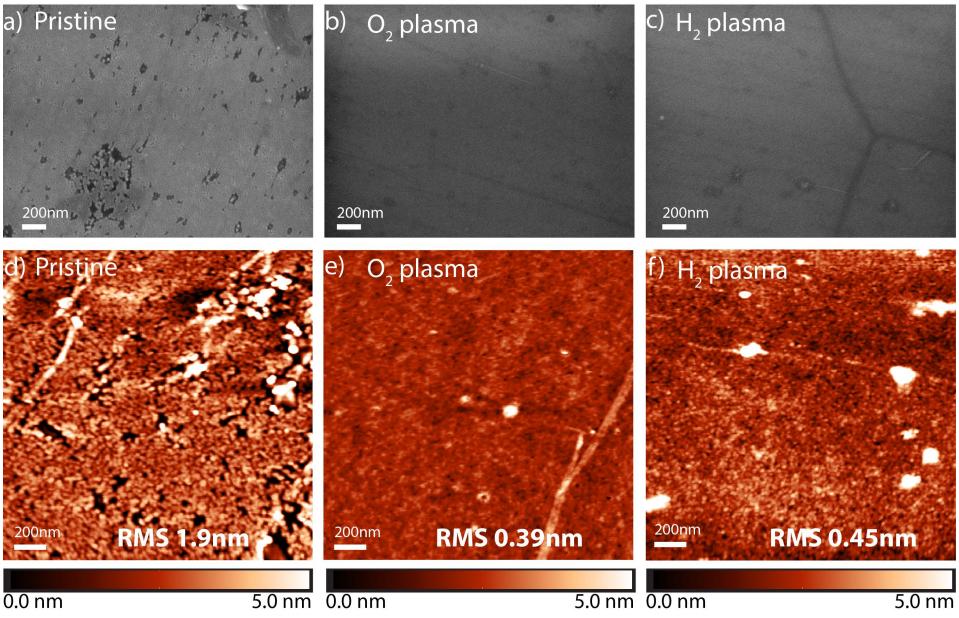


Figure 3.2: SEM and AFM images showing the Al_2O_3 coverage on graphene after 100 cycles of Al_2O_3 ALD at 100 ºC for a,d) pristine, b,e) 30 s O_2 plasma and c,f) 35 s H_2 plasma treated graphene. The root mean square (RMS) roughness determined from the AFM measurements is indicated as well.

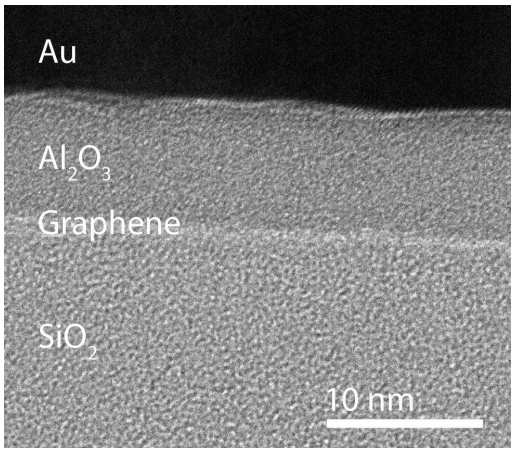


Figure 3.3: Cross-sectional TEM image of 100 cycles of Al_2O_3 deposited on graphene treated with 35 s H_2 plasma. The Al_2O_3 layer is 7.8 ± 0.4 nm thick and pinhole-free.

The thicknesses and optical properties of the Al_2O_3 layers deposited on the O_2 and H_2 plasma treated graphene have been determined with spectroscopic ellipsometry (SE) to be 11 ± 1 nm and 9 ± 1 nm, respectively. The refractive index of the Al_2O_3 films was 1.55 and 1.56 (at 633 nm) respectively, comparable to the ALD of Al_2O_3 on other substrates at 100 ºC [43]. The higher thickness of the Al_2O_3 on the O_2 plasma treated sample indicates a shorter nucleation delay of the Al_2O_3 when an O_2 plasma treatment is used. This is most likely caused by a more favored adsorption of TMA precursor molecules on epoxide (C-O-C) and hydroxyl (C-OH) groups compared to hydrogen groups (C-H). This will be discussed in more detail in the DFT section of this paper. The shorter nucleation delay on O_2 plasma treated graphene also makes it possible to deposit thinner uniform Al_2O_3 layers on the O_2 treated samples. In the case of the O_2 plasma treated graphene the Al_2O_3 layer was already closed after 50 cycles, corresponding to a layer thickness of approximately 5 nm. Considering the H_2 plasma treated samples, pinholes were still present in the layer after 75 ALD cycles. This indicates that 100 ALD cycles is the minimum required for a closed Al_2O_3 layer using H_2 plasma functionalization with the current plasma settings and exposure time. Increasing the H_2 plasma exposure time could help to increase the coverage at lower ALD cycles numbers, but can also irreversibly damage the graphene (see Appendix A).

To confirm that the Al_2O_3 layer after a H_2 plasma treatment and 100 cycles Al_2O_3 ALD is indeed closed, a TEM cross-section was made (see Figure 3.3). The cross-

section shows a uniform Al_2O_3 layer with a thickness of 7.8 ± 0.4 nm, which is in agreement with the Al_2O_3 thickness obtained from the SE measurements.

3.3.3 Quality of the Graphene: Raman Characterization

The above results show that uniform Al_2O_3 deposition on graphene can be obtained by using an O_2 and H_2 plasma pretreatment. However, it is generally observed that graphene is damaged by such treatments [12,16,20,21]. This is also indicated by the XPS data in Figure 3.1, which show the conversion of sp^2 bonds to sp^3 bonds. In this regard, the quality of the graphene was studied before the plasma treatment, after the plasma treatment, after ALD and after annealing at 400 °C using Raman spectroscopy and Hall measurements (next section). The Raman measurements performed after each processing step for the different graphene samples are shown in Figure 3.4. The Raman D-band (~ 1350 cm^{-1}) is related to defects in the graphene or to the functionalization of graphene by covalent bonding [44]. Pristine graphene (Figure 3.4a) shows no D-band indicating that the graphene is of high quality. Subsequent Al_2O_3 ALD on the pristine graphene does not create any defects in the graphene, but also does not result in the formation of a closed Al_2O_3 layer. Annealing the pristine graphene with Al_2O_3 at 400 ºC for 2h in a 50:1 Ar/H_2 mixture results in the formation of a small D-band and an α-Carbon background (~ 1200-1500 cm^{-1}), which could be due to the dehydrogenation of the polymer residues present at the graphene surface. These residues are a result of the graphene transfer process [41]. Even though the graphene was annealed before ALD to minimize the residues, it has appeared impossible to remove them completely [41].

Treating the graphene with a 30 s O_2 plasma creates a significant D-band (Figure 3.4b) as a result of the conversion of sp^2 to sp^3 carbon (also shown by XPS) and possibly by the creation of defects due to ion bombardment. After Al_2O_3 ALD the magnitude of the D-band decreases considerably, indicating that the ALD process is able to partially heal the defects introduced by the plasma pretreatment or remove functional groups present on the graphene. This could be due to a reaction of the ALD precursor molecules with the functional groups or the passivation of defects by Al_2O_3 [45]. In an attempt to further reduce the D-band the sample was annealed at 400 ºC under the same conditions as the pristine graphene. Although this reduced the D-band further, it could not be completely removed. Possibly, the species in the O_2 plasma irreversibly damaged the graphene or part of the functional groups remains on the graphene.

In the case of a 35 s H_2 plasma treatment a similar trend as for the O_2 plasma treated sample can be observed by Raman spectroscopy (Figure 3.4c). Similar to the O_2 plasma the H_2 plasma results in the appearance of a D-band in the Raman spectrum. The D-band after H_2 plasma treatment is lower compared to the D-band created after O_2 plasma treatment. Subsequent Al_2O_3 ALD leads to a reduction of these defects or removal of the C-H functional groups from the surface. Annealing the H_2 plasma treated sample with Al_2O_3 at 400 ºC results in the complete annihilation of the D-band. The Raman spectrum obtained after annealing is similar to the pristine graphene spectrum obtained after transfer to the SiO_2 substrate. This points in the direction that the D-band is indeed related to C-H bonds, which can be removed after annealing at 400 ºC, as defects are not likely to be annealed at this temperature [24]. It should be noted that for hydrogenated graphene also a weak D'-band (~ 1620 cm^{-1}) should be present [44]. This peak is, however, not distinguishable in Figure 3.4c, because the G-band (~ 1600 cm^{-1}) is significantly broadened upon annealing the pristine graphene to remove the PMMA residue, thus introducing overlap with the D' band. This broadening is related to the formation of small amounts of amorphous carbon during the anneal on top of the graphene [46]. Direct H_2 plasma exposure of pristine graphene (without annealing) does result in the formation of a distinguishable D'-band (see chapter 5).

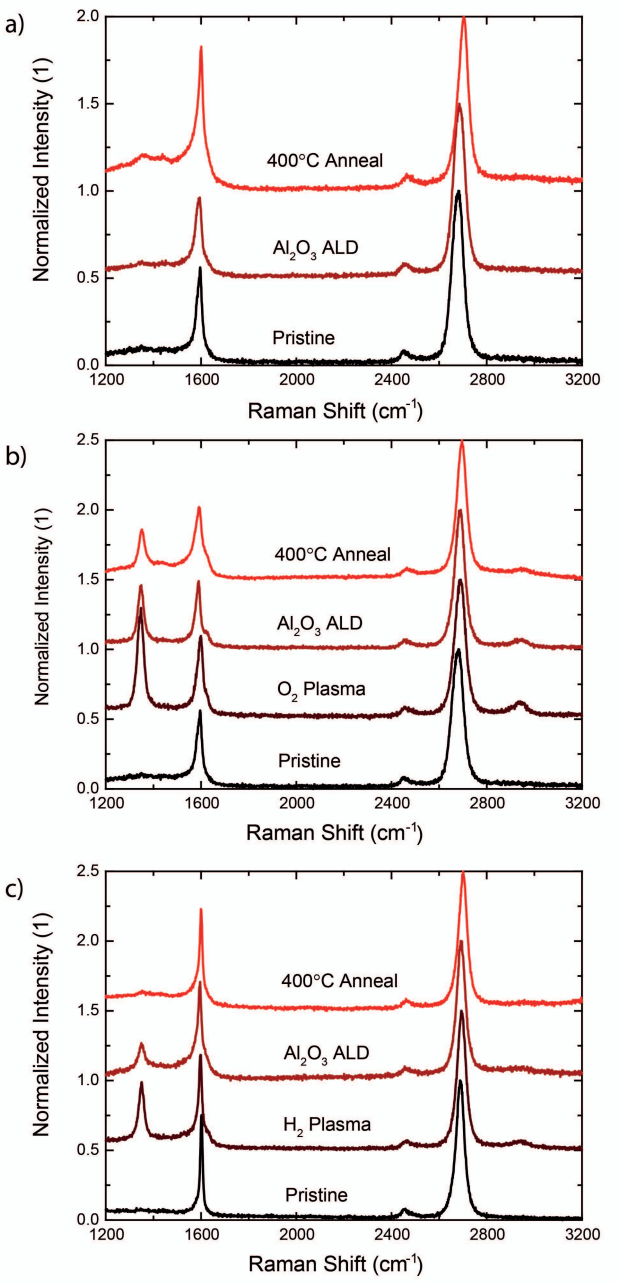


Figure 3.4: Raman spectra of the different graphene samples after each processing step: transfer, plasma treatment, 100 cycles Al_2O_3 ALD, and 400 ºC anneal for a) untreated graphene, b) 30 s O_2 plasma treated graphene, and c) 35 s H_2 plasma treated graphene. The spectra are normalized to the 2D band and are offset for clarity.

3.3.4 Quality of the Graphene: Hall Mobility Characterization

Hall mobility measurements were performed to investigate the effect of the O_2 and H_2 plasma treatments on the electrical properties of graphene (Figure 3.5). The mobility values of the pristine graphene samples used in this study range between 1300-1800 $cm^2/(V \cdot s)$ (indicated by the black bars in Figure 3.5) which is typical for large area (1x1 cm^2) CVD graphene [3,47,48]. The deposition of Al_2O_3 on pristine graphene results in a mobility increase to 117% of its initial value (1520 $cm^2/(V \cdot s)$). This increase could be caused by several effects: (1) Al_2O_3 can passivate defects present in the graphene [49], (2) Al_2O_3 can act as a barrier preventing H_2O and O_2 reaching the graphene surface which would otherwise degrade the carrier mobility of graphene [50] and, (3) The Al_2O_3 layer can also help to screen charged impurities, present in the SiO_2 substrate, which would normally act as scattering centers for the electrons and holes in the graphene [51]. Charge screening could also explain why the mobility is further increased to 140% of its initial value (1860 $cm^2/(V \cdot s)$) after the sample is annealed at 400 ºC. This is because annealing Al_2O_3 at 400 ºC generally gives the highest Al_2O_3 built-in charge [52], resulting in maximum passivation and an increased mobility of the graphene after annealing. It should be noted though that the Al_2O_3 layer on pristine graphene is not closed and therefore not suited for applications, for example, as a gate dielectric.

Figure 3.5 also shows that both the O_2 and H_2 plasma treatments reduce the charge carrier mobility of graphene, as expected. After O_2 plasma the mobility is reduced to 195 $cm^2/(V \cdot s)$ (11% of its initial value), whereas after a H_2 plasma the mobility is decreased to 467 $cm^2/(V \cdot s)$ (32% of its initial value). This is in line with the XPS and Raman data which show the conversion of sp^2 to sp^3 carbon. The out-of-plane bonds act as scattering centers for the electrons and holes in the graphene and therefore lower the mobility.

Al_2O_3 ALD on the O_2 plasma treated sample causes a partial recovery of the mobility to 78% of its initial value (1390 $cm^2/(V \cdot s)$), most likely due to passivation and barrier properties of Al_2O_3, as was discussed for ALD on pristine graphene above. Additionally, part of the functional groups or defects might be removed from the surface by the precursor molecules during Al_2O_3 ALD. This hypothesis is further strengthened by the observed decrease of the D-band in the Raman spectrum after Al_2O_3 ALD (Figure 3.4b). The DFT section of this paper will elaborate further on this hypothesis. The charge carrier mobility of the O_2 plasma treated graphene sample with Al_2O_3 can be recovered to 91% of its original value (1630 $cm^2/(V \cdot s)$) by annealing at 400 ºC. The recovery is most likely a result of the improved passivation properties of the Al_2O_3, as

observed for the pristine sample. Additionally, some functional groups on the graphene desorb during the annealing, indicated by a further decrease in the Raman D-band (Figure 3.4b). The functional groups removed could be primarily hydroxyl groups, which have limited stability on graphene (see discussion in the DFT section). The incomplete recovery of the mobility after annealing indicates that some defects or functional groups remain on the O_2 plasma treated sample, which is confirmed by the still observable D-band in the Raman spectra.

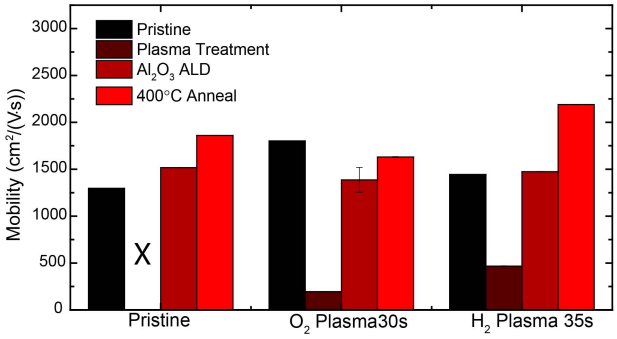


Figure 3.5: Mobility of graphene determined by Hall-measurements, after transfer, after plasma treatment, after 100 cycles Al_2O_3 ALD, and after 400 ºC anneal for pristine, O_2, and H_2 plasma treated graphene.

Al_2O_3 ALD on the H_2 plasma treated graphene results in a large mobility improvement from 32% (467 $cm^2/(V \cdot s)$, after the H_2 plasma treatment) to 102% of its initial value (1470 cm^2/Vs, after 100 ALD cycles). As for the O_2 plasma treatment, this recovery is most likely caused by a combination of the passivation and barrier properties of Al_2O_3 and a partial removal of the surface groups. Likewise, the removal of surface groups is supported by the decrease of the D-band in the Raman spectrum after Al_2O_3 ALD (Figure 3.4c). Compared to the O_2 plasma treatment, the D-band is considerably weaker for the H_2 plasma treatment after ALD, indicating that the groups created by the H_2 plasma treatment can be more easily removed, which explains the higher mobility recovery. Annealing the sample at 400 °C further improves the mobility to 152% of its original value (2190 $cm^2/(V \cdot s)$). The absence of a D-band in the Raman spectrum after annealing the H_2 plasma treated samples explains the larger increase of the mobility compared to the O_2 treatment. This also shows that the H_2 plasma treatment is fully reversible and that the functional groups created by the plasma treatment can be removed by a 400 °C anneal.

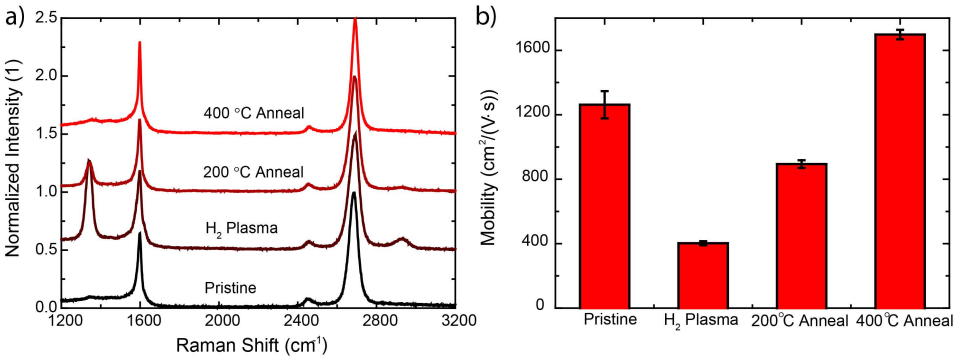


Figure 3.6: Hydrogen plasma reversibility for a graphene sample exposed for 35 s to H_2 plasma and annealed at 200 and 400 ºC . a) Raman spectra and b) mobility determined from Hall measurements after the different processing steps. The pristine graphene sample was annealed at 400 °C before the Hall measurement to exclude the influence of annealing effects on the mobility.

The additional improvement of the mobility observed after Al_2O_3 ALD and annealing for the H_2 treated sample compared to the pristine graphene sample (152% vs. 140%) could be caused by the removal of polymer residues from the graphene surface during the plasma exposure. To investigate this possible cleaning effect, a graphene sample, which was first annealed at 400 °C, was hydrogenated and subsequently annealed at 200 ºC for 2 h and 400 ºC for 2 h without performing Al_2O_3 ALD (Figure 3.6). Raman spectroscopy (Figure 3.6a) shows that after annealing at 400 ºC the graphene is recovered to its original state without functionalization. Figure 3.6b shows that this is accompanied by an increase in the mobility to 134% of its original value. This indicates that the H_2 plasma indeed removes polymer residuals from the surface and explains the additional improvement observed compared to pristine graphene.

The removal of polymer residues possibly also occurs during the O_2 plasma treatment [19]. However, no mobility improvement is observed for the O_2 plasma sample. Most likely, the mobility decrease due to the remaining functional groups is larger than the mobility increase due to polymer residue removal.

3.3.5 DFT Simulations

To further understand the enhanced Al_2O_3 nucleation on O_2 and H_2 plasma treated graphene first-principles (*ab initio*) DFT simulations were performed. To this end, models of pristine, oxygenated graphene (graphene oxide) and hydrogenated graphene were created (Figure 3.7). In principle functional groups can be attached to one or both

facets of graphene, leading to single-sided or double-sided functionalization. However, one should note that graphene is placed on a Si/SiO_2 substrate during the O_2/H_2 plasma pretreatments, and the functionalities will therefore be predominantly attached to the accessible side rather than both sides. In view of this, the current DFT analysis is limited to the single-sided varieties (unless stated otherwise). Besides, the SiO_2 substrate is shown to only have a very limited effect on the TMA precursor adsorption (see Appendix B). Considering this and the concomitant computational efforts, the SiO_2 substrate was not included in the simulation models used for the further analysis.

Pristine graphene (PG) was modeled by an 8x8 graphene supercell. For graphene oxide (GO) several models were considered accounting for the different oxygen-containing surface groups observed by XPS (Figure 3.1). Unlike epoxidized graphene, it turned out that single-sided hydroxylated graphene was not stable upon TMA binding due to the detaching –OH groups, as evident from molecular dynamics simulations at finite temperature (data not shown). Therefore, double-sided hydroxylated graphene was used to simulate the TMA binding on hydroxylated graphene. In contrast, the hydroxyl groups were stable on the single-sided GO mixture, containing non-ordered decoration of epoxy, hydroxyl and hydrogen. For hydrogenated graphene (HG), the two most-likely configurations of the single-sided HG were modeled. A detailed discussion regarding the choice of these models can be found elsewhere (PG and GO) [37,38].

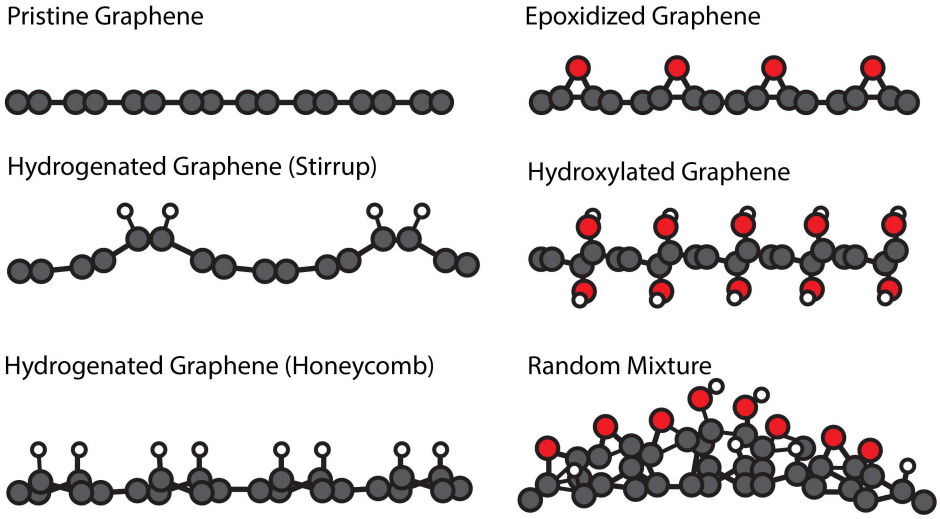


Figure 3.7: Side view of the ball and stick representation of the models used for simulating oxygenated and hydrogenated graphene in the DFT calculations. Carbon (grey), Oxygen (red) and hydrogen (white).

The TMA precursor physisorption (ΔE_p), chemisorption (ΔE_c) and reaction energies ($\Delta E_r=\Delta E_c-\Delta E_p$) were calculated for each of the model systems. For computing the chemisorption energies, several reaction pathways were considered:

$$2X^* + AlMe_{3\,(g)} \rightarrow X–AlMe_2^* + X–Me^* \quad (3.2a)$$

$$2X^* + AlMe_{3\,(g)} \rightarrow X_2–AlMe^* + Me_{2\,(g)} \quad (3.2b)$$

$$2X^* + AlMe_{3\,(g)} \rightarrow X_2–AlMe\text{-}CH_2^* + CH_{4\,(g)} \quad (3.2c)$$

$$(X–H)^* + AlMe_{3\,(g)} \rightarrow X–AlMe_2^* + CH_{4\,(g)} \quad (3.3a)$$

$$2(C\text{-}H)^* \rightarrow (C\text{-}C)^* + H_{2\,(g)} \quad (3.3b)$$

$$3(X–H)^* + AlMe_{3\,(g)} \rightarrow X–AlMe_2^* + 2X^* + CH_{4\,(g)} + H_{2\,(g)} \quad (3.3c)$$

$$2(X–H)^* + AlMe_{3\,(g)} \rightarrow X_2–AlMe^* + Me_{2\,(g)} + H_{2\,(g)} \quad (3.3d)$$

where X represents either C or O, depending on the functionalization type (pristine or oxygenated). In addition, X–H denotes that the surface site is H-terminated and an asterisk refers to a surface group, whereas Me stands for a methyl ($-CH_3$) group. Other reaction pathways are possible depending on the ALD temperature, simultaneous binding of multiple precursors, and lingering co-reactants/contaminants, etc. However, the approach used here provides sufficient information for a qualitative comparison of the binding energies, and is commonly used for studying ALD processes on graphene [37,53,54] and other substrates [55,56].

The results of TMA physisorption and chemisorption on the different graphene model systems are compiled in Table 3.1, whereas the corresponding minimum-energy structures of the physisorbed and chemisorbed species for the most relevant pathways are shown in Figure 3.8. A complete overview of all considered reaction pathways can be found in reference [38].

Table 3.1: Computed (PBE-D3 level) physisorption (ΔE_p), chemisorption (ΔE_c) and reaction (ΔE_r=ΔE_c-ΔE_p) energies (in eV) of TMA on bare and functionalized graphenes. Corresponding Gibbs energy changes (ΔG) are given in brackets. ΔE_c values are only reported for the lowest-energy chemisorbed species, as identified by "Type" (see Eq. 3.2-3.3 for definitions). The coverage is defined as the relative ratio of the number of H and/or O adatoms to the carbon atoms on graphene.

System	Coverage	ΔE_p	ΔE_c	ΔE_r	Type
Pristine Graphene (PG)	0%	-0.53 [-0.23]	1.84 [2.29]	2.37 [2.52]	Me transfer (3.1a)
Graphene Oxide (GO)					
GO – Epoxidized (single-sided)	25%	-1.70 [-1.04]	-7.37 [-6.82]	-5.67 [-5.78]	Me_2 release (3.1b)
			-5.69 [-5.15]	-3.99 [-4.11]	Me transfer (3.1a)
GO– Hydroxylated (double sided)[a]	50%	-0.45 [-0.34]	-2.67 [-2.56]	-2.22 [-2.22]	CH_4 release (3.2a)
GO– Random mixture (single-sided) (epoxy + hydroxyl + hydrogen groups)	33%	-0.61 [-0.16]	-5.33 [-4.76]		Me_2 release (3.1b)
				-4.72 [-4.60]	
			-3.52 [-3.21]	-2.91 [-3.05]	CH_4 release (3.2a)
Hydrogenated graphene (HG)					
HG – stirrup (single-sided)	25%	-0.54 [-0.11]	-0.54 [0.01]	0.00 [0.12]	CH_4 release (3.2a)
			-1.29 [-1.20]	-0.75 [-1.09]	H_2 release (3.2b)
			-2.23 [-2.20]	-1.69 [-2.09]	H_2 + CH_4 release (3.2c)
			-0.38 [-0.19]	0.16 [-0.08]	H_2 + Me_2 release (3.2d)
HG – honeycomb (single-sided)	25%	-0.44 [-0.07]	0.12 [0.42]	0.56 [0.49]	CH_4 release (3.2a)
			-1.00 [-0.93]	-0.56 [-0.86]	H_2 release (3.2b)
			-1.39 [-1.48]	-0.95 [-1.41]	H_2 + CH_4 release (3.2c)
			0.25 [0.13]	0.69 [0.20]	H_2 + Me_2 release (3.2d)

[a] The single-sided hydroxylated graphene oxide is not stable upon TMA binding (i.e. the –OH groups leave the surface) and thus not included in this table.

Pristine graphene has a high chemical stability due to the sp^2-carbon configuration. This results in a rather weak TMA physisorption (ΔE_p = -0.53 eV) accompanied by an unfavorable (endothermic) chemical binding of TMA (ΔE_c = 1.84 eV). The dissociative TMA binding preferably proceeds via a methyl transfer mechanism (Eq. 3.2a), which involves a high activation energy (ΔE_a = 3.60 eV, see Figure 3.9 for the minimum-energy path). The other investigated reaction pathways do not lead to Al bonding on the graphene which is required for proper Al_2O_3 nucleation. This indicates that TMA adsorption on PG is kinetically and thermodynamically unfavorable, which is in agreement with the SEM and AFM results (Figure 3.2a,d), showing a non-uniform coverage of Al_2O_3 on pristine graphene. Nucleation probably starts at defect sites and grain boundaries with enhanced chemical reactivity, while no growth occurs on the pristine graphene. This results in the observed island-like growth instead of a uniform smooth Al_2O_3 layer due to the unfavorable TMA adsorption on the graphene plane.

Graphene oxide, however, can facilitate uniform nucleation and growth for Al_2O_3 ALD (Figure 3.2b,e and also elsewhere [20,21]). In line with this, the DFT calculations indicate a stronger TMA adsorption on all considered GO surfaces, compared to PG (Table 3.1, Figure 3.7). Stronger TMA adsorption on GO can be attributed to the availability of p-orbitals of the surface oxygen that interact with those of TMA aluminum. Among the different models, GO with ordered epoxy groups provides the strongest adsorption of TMA, due to having the highest free-electron density. High binding affinities are obtained for epoxidized GO, as evident from the physisorption and chemisorption energies (ΔE_p = -1.70 eV and ΔE_c = -7.37 eV). Compared to epoxidized GO, hydroxylated GO provides a weaker TMA adsorption (ΔE_p = -0.45 eV and ΔE_c = -2.67 eV), likely due to the H-passivation effect (i.e. reduced availability of free-electrons) of the oxygen. Likewise, a mixture of these two oxygen-containing functionalities provides an intermediate TMA binding strength (ΔE_p = -0.61 eV and ΔE_c = -5.33 eV). Considering the DFT calculations, it becomes clear that O_2 plasma pretreatments enable an improved ALD nucleation by predominantly attaching epoxy groups which have a strong binding affinity towards TMA.

From the analysis of the energetically most plausible pathways predicted for the TMA chemisorption on the GO surfaces (Table 3.1, Figure 3.8), a variation depending on the surface functionalization can be observed. On single-side epoxidized GO, TMA preferably chemisorbs trifunctionally (through three surface epoxys) while releasing a volatile ethane (Me_2 or C_2H_6) product (Eq. 3.2b, Figure 3.8). The latter proceeds with a negligible barrier (ΔE_a = 0.04 eV, Figure 3.9), while gaining substantial energy in return (ΔE_c = -7.37 eV). The methyl transfer mechanism (Eq. 3.2a, Figure 3.7) for binding

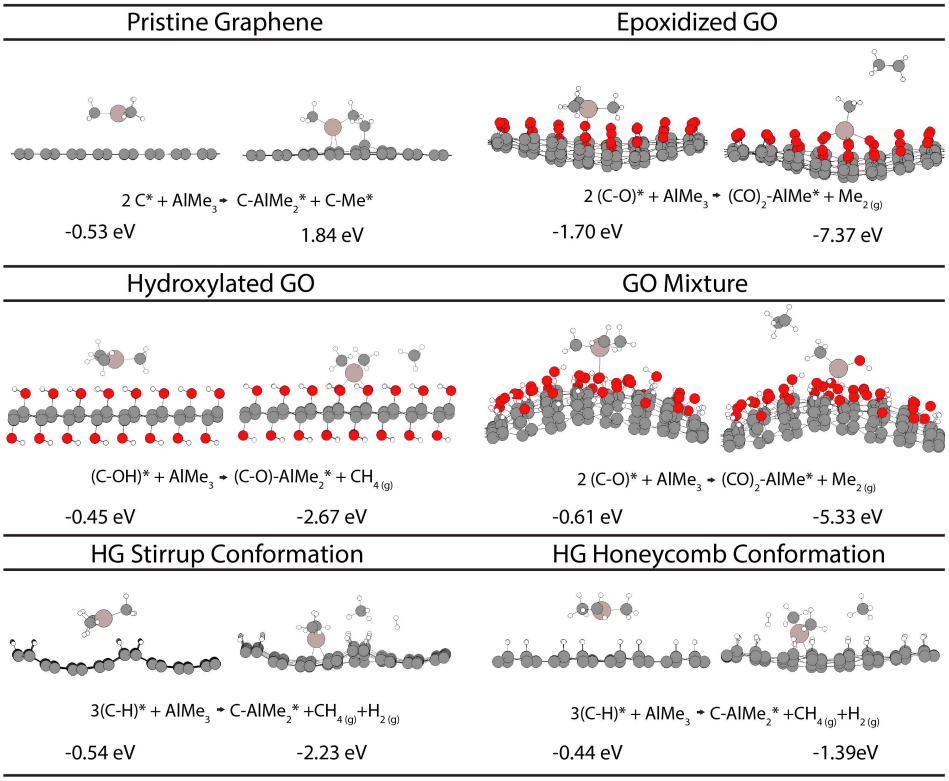


Figure 3.8: DFT-predicted structures of the lowest-energy (left) physisorbed and (right) chemisorbed species and their relative energies from the TMA adsorption on pristine graphene, oxygenated graphene (i.e. graphene oxide, GO) and hydrogenated graphene (HG).

TMA on epoxidized GO is energetically less favorable (ΔE_c = -5.67 eV), making it less probable than the ethane release mechanism. TMA chemisorption on hydroxylated GO is predicted to proceed via the methane (CH_4) release pathway (Eq. 3.3a), in agreement with other -OH terminated substrates such as SiO_2, Al_2O_3, and TiO_2 [57]. This reaction proceeds via a low barrier as well (ΔE_a = 0.09 eV, Figure 3.9) and produces a sizeable energy gain (ΔE_r = -2.22 eV), rendering it accessible from both the kinetic and thermodynamic aspect. Dissociative TMA adsorption on the GO surface with a mixture of epoxy and hydroxyl groups, will undergo either the methane- and ethane-release mechanism, depending on the actual surface composition. For the mixture model considered here (with 33% coverage) the ethane release mechanism is more likely to occur (ΔE_r = -4.72 vs. -2.91 eV).

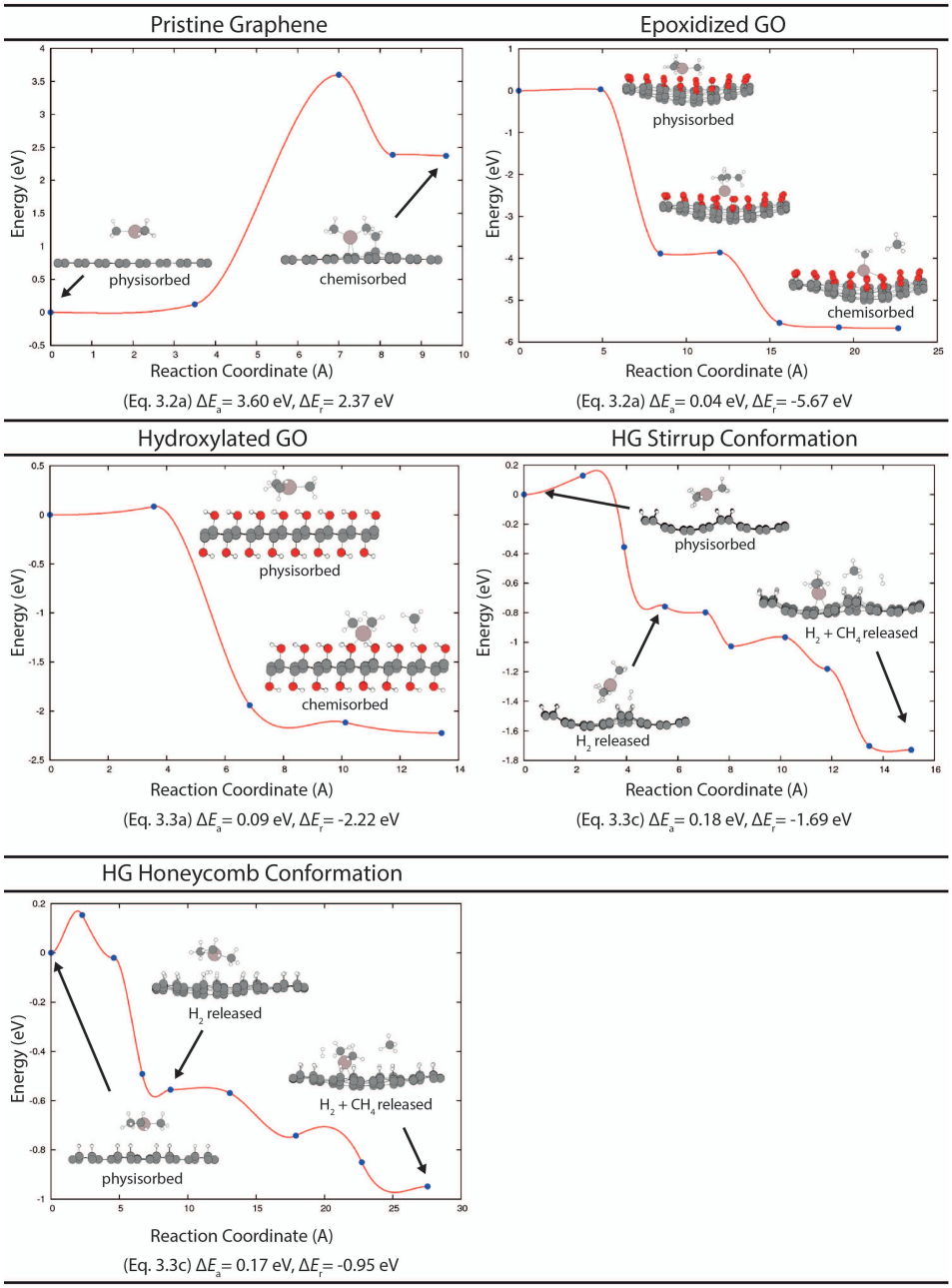


Figure 3.9: PBE-D3 level minimum energy paths corresponding to the different reaction pathways for TMA precursor binding on pristine graphene, GO and HG. First and last points on the reaction coordinate correspond to the physisorbed and chemisorbed species, respectively.

DFT calculations indicate a weaker TMA binding for the hydrogenated graphene (HG), compared to GO, but the binding is still stronger than for PG (Table 3.1). TMA physisorption on honeycomb and stirrup HG is of average strength (ΔE_p = -0.54 eV vs -0.44 eV). The dissociative binding of TMA is energetically favorable on both surfaces, whereas the stirrup configuration affords a somewhat stronger binding (ΔE_c = -2.23 eV vs. -1.39 eV). The DFT results indicate that chemisorption proceeds most likely via the CH_4-release mechanism, as for the hydroxylated GO surface. However, different from the hydroxylated GO, dissociative binding of TMA (i.e. CH_4 formation) is preceded by a release of gaseous H_2 in order to facilitate the binding (Eq. 3.3c-d). This two-step chemisorption scheme is thermodynamically and kinetically accessible on both single-sided HG surfaces by being energetically downhill (ΔE_r = -1.69 eV and -0.95 eV) and having low activation barriers (ΔE_a = 0.18 eV and 0.17 eV, on stirrup and honeycomb respectively, see Figure 3.9). However, compared to the various GO (see above), TMA chemisorption on HG surfaces is kinetically and thermodynamically less favorable, slowing down the TMA adsorption. This finding falls in line with the longer nucleation delay on HG in comparison to GO observed experimentally.

All the discussions are so far based on the zero-temperature gas-phase energies. To check the temperature and pressure effects on the reaction pathways, Gibbs energy changes are also computed (Table 3.1), mimicking the typical ALD conditions during the precursor pulse (T = 100 ^{o}C and P = 13.3 Pa). As evident from the Gibbs energies, higher temperatures are expected to cause an overall weaker TMA physisorption (on all studied surfaces), most likely due to the decrease in the translational and rotational entropies of gaseous precursor molecules. This in turn would enhance the TMA desorption rate with increasing temperatures, however, this can be compensated by the simultaneous adsorption of multiple precursor molecules (as previously shown for TMA binding on Al_2O_3 [58]). Besides, with more destabilized physisorbed species, the reaction energies are in general more negative at elevated temperatures (Table 3.1), rendering these reactions thermodynamically even more favored. It should also be noted that the energetically most feasible pathway for each considered surface remains the same as in the zero-temperature case, when temperature and pressure effects are also considered.

Considering the variety in the reaction mechanisms employed for the dissociative binding of TMA on diverse graphene surfaces, an overview is given in Figure 3.10. The most plausible pathway for hydrogenated graphene that combines H_2 and CH_4 release mechanisms is predicted to clean the hydrogen functionalities off the surface (typically three hydrogens per bound TMA molecule). In contrast, on the GO surfaces, the oxygen

adatoms are predicted to stay on the graphene surface on all feasible pathways. This is the likely reason for the observed reversibility of the H_2 plasma treatment after Al_2O_3 ALD as opposed to O_2 plasma treaded graphene (see Figure 3.4).

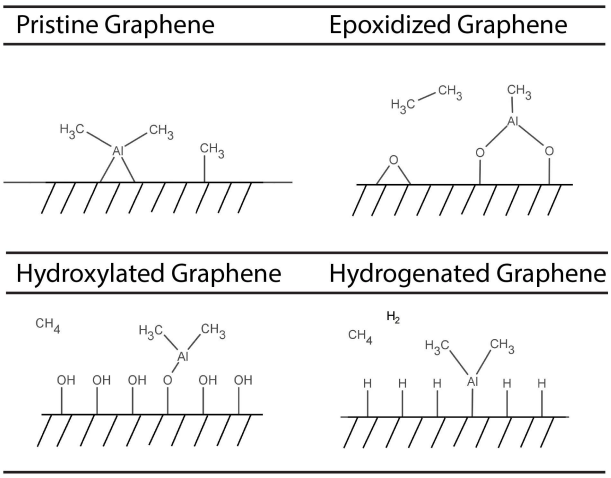


Figure 3.10: Schematic overview of the energetically most favorable TMA chemisorption mechanisms on pristine and functionalized graphene based on the PBE-D3-level calculations.

3.4 Conclusions

In conclusion, uniform Al_2O_3 ALD growth on graphene was obtained by functionalizing graphene with a reversible H_2 plasma treatment without deteriorating the graphene's electrical properties. The creation of C-H groups on the graphene surface during plasma treatment improved the adsorption of the ALD precursor TMA on graphene. This led to the formation of a closed uniform Al_2O_3 layer. On pristine graphene a closed film was not obtained due to the absence of dangling bonds and the resulting high activation barrier for TMA adsorption. DFT calculations confirmed the improved precursor adsorption on hydrogenated graphene. As for oxygen plasma treatments, the hydrogen plasma treatment led to the partial deterioration of the sp^2 hybridization of the graphene, which resulted in a drastic reduction in charge carrier mobility. Contrary to oxygen plasma functionalized graphene, for hydrogen plasma functionalized graphene this reduction in charge carrier mobility was fully recovered upon Al_2O_3 ALD. Subsequent annealing at 400 ºC further improved the mobility to 152% of its initial value. DFT calculations showed that the recovery of charge carrier mobility can be explained by a reaction pathway, in which TMA adsorption on hydrogenated graphene proceeds via a CH_4 release mechanism preceded by the

abstraction of H_2 from the surface, which recovers the sp^2 hybridization of graphene. The DFT predictions were confirmed by Raman spectroscopy. Factors that could explain the improvement of the charge carrier mobility of the graphene beyond its initial value are: (1) the excellent barrier properties of the ALD Al_2O_3 after annealing, (2) screening of charged impurity by Al_2O_3 and (3) the removal of resist residues by the H_2 plasma treatment. Functionalization of graphene by H_2 plasma treatments is therefore an excellent way to enable direct ALD growth of thin uniform dielectric layers on graphene without deteriorating graphene's electrical properties.

Acknowledgements

The authors would like to thank C.O. van Bommel, C.A.A. van Helvoirt, J.J.L.M. Meulendijks & J.J.A. Zeebregts for technical assistance. Dr. H. Friedrich is acknowledged providing access to the Hall measurement system. This work is part of the research program of the Foundation for Fundamental Research on Matter (FOM), which is part of the Netherlands Organization for Scientific Research (NWO).

3.5 Appendix A: Reversibility of the Plasma Treatments

For the plasma treatments discussed above, treatment times of 35 and 30 s were chosen for the H_2 and O_2 plasma, respectively. To obtain a higher density of functional groups on the graphene surface longer plasma treatments could be used. This would possibly also make the deposition of thinner dielectrics on the graphene possible. However, there are also species present in the plasma that do not contribute to the functionalization, and can possibly damage the graphene, for example photons (> 6 eV) and ions. The damage induced by these processes is not reversible. Long H_2 and O_2 plasma exposures are therefore expected to irreversibly damage the graphene.

This is shown in Figure 3.11. After 45 s of H_2 plasma treatment the defect related D-band (1350 cm^{-1}) remains present in the Raman spectrum after ALD deposition and annealing, showing that the functionalization is only partly reversed (see Figure 3.11a). For the O_2 plasma treatments beyond 30 s the effect is even stronger, the 2D-peak (2690 cm^{-1}) almost completely disappears after plasma treatment, and the peaks broaden significantly (see Figure 3.11b). The peak-broadening indicates the formation of α-carbon, which can no longer be converted back to graphene in the subsequent ALD and annealing steps. The Hall measurements (Figure 3.11c) also show that the graphene is irreversibly damaged by the longer plasma treatments. An O_2 plasma treatment of 1 min

leads to a reduction of the mobility of more than 98% and cannot be recovered after Al_2O_3 ALD and subsequent annealing at 400 ºC. After a 45 s H_2 plasma treatment the mobility recovers, after ALD and annealing, to only 44% of its original value. Indicating that also the H_2 functionalization process becomes irreversible for longer plasma treatment times. The irreversibility of the plasma treatments for longer exposure times is most likely caused by ions and photons present in the plasma. The functionalization of graphene using other sources of H_2 or O_2 radicals, such as hot wire generation, might therefore make it possible to achieve a higher functionalization degree without irreversibly damaging the graphene since energetic species such as ions and photons are absent. The higher density of functional groups could make the deposition of thinner Al_2O_3 films on graphene by ALD possible.

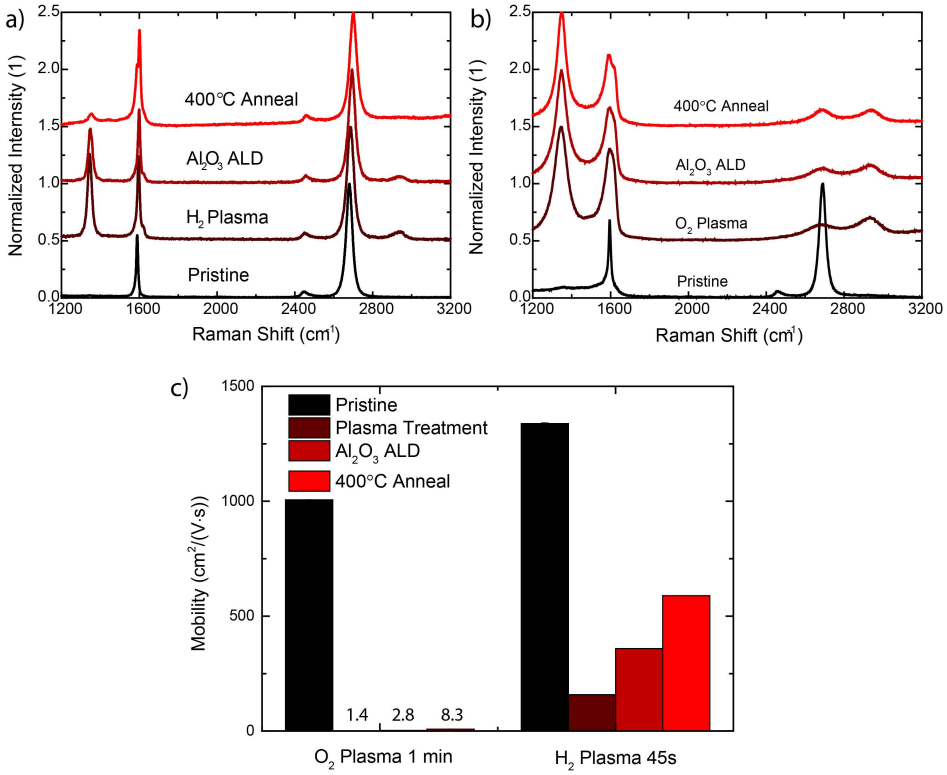


Figure 3.11: Reversibility of different plasma treatments determined by Raman spectroscopy for a) 45 s H_2 plasma treated sample and b) 1 min O_2 plasma treated sample and c) the mobility of the samples, after each processing step. The pristine samples were annealed at 400 °C before measuring. The ALD was performed at 200 °C for 100 cycles.

3.6 Appendix B: Effect of the SiO_2 Substrate on the TMA Binding

In order to check if the SiO_2 substrate has an effect on the TMA adsorption on pristine graphene, a hydroxylated α-quartz (001) surface slab model (discussed in depth in ref. [59]) is considered as a substrate. The same DFT settings were used as for the free-standing graphene. The resulting DFT energies and corresponding minimum structures are compiled in Figure 3.12. Evidently, the physisorption energy differs only very slightly (-0.53 eV vs. -0.52 eV) upon the addition of a hydroxylated SiO_2 support. Likewise, for the chemisorption of TMA via the most feasible route involving a methyl transfer, the binding energy is affected by the SiO_2 substrate only insignificantly (1.84 eV vs. 1.82 eV). The rather minute substrate effect can be ascribed to the H-passivation of SiO_2, following from the spontaneous hydroxylation of a freshly-cleaved SiO_2 surface upon air exposure [59]. This passivation mitigates the strength of the interaction between SiO_2 substrate and graphene, which is mostly through non-bonded interactions rather than bonded ones, and fades rapidly with increasing separation of the two subunits. Similarly, other weakly interacting substrates, for example other 2D materials are expected to have little influence on the binding energy and reaction pathways.

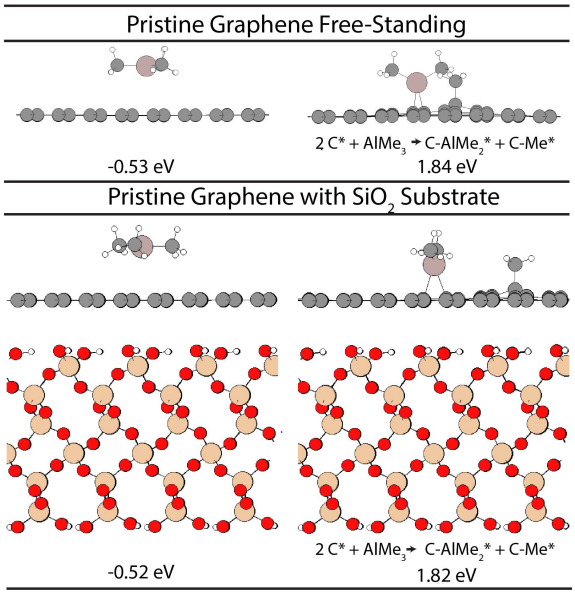


Figure 3.12: DFT-predicted structures of the lowest-energy (left) physisorbed and (right) chemisorbed species [and their relative energies] resulting from the TMA adsorption on (top) free-standing and (bottom) SiO_2-supported pristine graphene.

References

1. Morozov, S. V., Novoselov, K.S., Katsnelson, M.I., et al. (2008) Giant Intrinsic Carrier Mobilities in Graphene and Its Bilayer. *Phys. Rev. Lett.*, **100** (1), 16602.

2. Schwierz, F. (2010) Graphene transistors. *Nat. Nanotechnol.*, **5** (7), 487–496.

3. Wu, Y., Jenkins, K.A., Valdes-Garcia, A., et al. (2012) State-of-the-Art Graphene High-Frequency Electronics. *Nano Lett.*, **12** (6), 3062–3067.

4. Popinciuc, M., Józsa, C., Zomer, P.J., et al. (2009) Electronic spin transport in graphene field-effect transistors. *Phys. Rev. B*, **80** (21), 214427.

5. Wang, X., Tabakman, S.M., and Dai, H. (2008) Atomic Layer Deposition of Metal Oxides on Pristine and Functionalized Graphene. *J. Am. Chem. Soc.*, **130** (26), 8152–8153.

6. Park, K.S., Kim, S., Kim, H., et al. (2015) Wafer-scale single-domain-like graphene by defect-selective atomic layer deposition of hexagonal ZnO. *Nanoscale*, **7** (42), 17702–17709.

7. Garces, N.Y., Wheeler, V.D., and Gaskill, D.K. (2012) Graphene functionalization and seeding for dielectric deposition and device integration. *J. Vac. Sci. Technol. B Microelectron. Nanom. Struct.*, **30** (3), 30801.

8. Marichy, C., and Pinna, N. (2013) Carbon-nanostructures coated/decorated by atomic layer deposition: Growth and applications. *Coord. Chem. Rev.*, **257** (23–24), 3232–3253.

9. Kim, J., and Jandhyala, S. (2013) Atomic layer deposition of dielectrics for carbon-based electronics. *Thin Solid Films*, **546**, 85–93.

10. Fallahazad, B., Kim, S., Colombo, L., and Tutuc, E. (2010) Dielectric thickness dependence of carrier mobility in graphene with HfO_2 top dielectric. *Appl. Phys. Lett.*, **97** (12), 123105.

11. Lee, B., Park, S., Kim, H.-C., et al. (2008) Conformal Al_2O_3 dielectric layer deposited by atomic layer deposition for graphene-based nanoelectronics. *Appl. Phys. Lett.*, **92** (20), 203102.

12. Lim, T., Kim, D., and Ju, S. (2013) Direct deposition of aluminum oxide gate dielectric on graphene channel using nitrogen plasma treatment. *Appl. Phys. Lett.*, **103** (1), 13107.

13. Dlubak, B., Kidambi, P.R., Weatherup, R.S., et al. (2012) Substrate-assisted

nucleation of ultra-thin dielectric layers on graphene by atomic layer deposition. *Appl. Phys. Lett.*, **100** (17), 173113.

14. Farmer, D.B., Chiu, H.-Y., Lin, Y.-M., et al. (2009) Utilization of a Buffered Dielectric to Achieve High Field-Effect Carrier Mobility in Graphene Transistors. *Nano Lett.*, **9** (12), 4474–4478.

15. Alaboson, J.M.P., Wang, Q.H., Emery, J.D., et al. (2011) Seeding Atomic Layer Deposition of High- k Dielectrics on Epitaxial Graphene with Organic Self-Assembled Monolayers. *ACS Nano*, **5** (6), 5223–5232.

16. Nayfeh, O.M., Marr, T., and Dubey, M. (2011) Impact of Plasma-Assisted Atomic-Layer-Deposited Gate Dielectric on Graphene Transistors. *IEEE Electron Device Lett.*, **32** (4), 473–475.

17. Young, M.J., Musgrave, C.B., and George, S.M. (2015) Growth and Characterization of Al_2O_3 Atomic Layer Deposition Films on sp^2 -Graphitic Carbon Substrates Using NO_2 /Trimethylaluminum Pretreatment. *ACS Appl. Mater. Interfaces*, **7** (22), 12030–12037.

18. Lee, B., Mordi, G., Kim, M.J., et al. (2010) Characteristics of high-κ Al_2O_3 dielectric using ozone-based atomic layer deposition for dual-gated graphene devices. *Appl. Phys. Lett.*, **97** (4), 43107.

19. Jandhyala, S., Mordi, G., Lee, B., et al. (2012) Atomic Layer Deposition of Dielectrics on Graphene Using Reversibly Physisorbed Ozone. *ACS Nano*, **6** (3), 2722–2730.

20. Shin, W.C., Bong, J.H., Choi, S.-Y., and Cho, B.J. (2013) Functionalized Graphene as an Ultrathin Seed Layer for the Atomic Layer Deposition of Conformal High-κ Dielectrics on Graphene. *ACS Appl. Mater. Interfaces*, **5** (22), 11515–11519.

21. Nourbakhsh, A., Adelmann, C., Song, Y., et al. (2015) Graphene oxide monolayers as atomically thin seeding layers for atomic layer deposition of metal oxides. *Nanoscale*, **7** (24), 10781–10789.

22. Park, Y.H., Kim, M.H., Kim, S. Bin, et al. (2016) Enhanced Nucleation of High-κ Dielectrics on Graphene by Atomic Layer Deposition. *Chem. Mater.*, **28** (20), 7268–7275.

23. Dingemans, G., van de Sanden, M.C.M., and Kessels, W.M.M. (2010) Influence of the Deposition Temperature on the c-Si Surface Passivation by Al_2O_3 Films Synthesized by ALD and PECVD. *Electrochem. Solid-State Lett.*, **13** (3), H76.

24. Elias, D.C., Nair, R.R., Mohiuddin, T.M.G., et al. (2009) Control of Graphene's

Properties by Reversible Hydrogenation: Evidence for Graphane. *Science*, **323** (5914), 610–613.

25. Luo, Z., Yu, T., Kim, K., et al. (2009) Thickness-Dependent Reversible Hydrogenation of Graphene Layers. *ACS Nano*, **3** (7), 1781–1788.

26. Blöchl, P.E. (1994) Projector augmented-wave method. *Phys. Rev. B*, **50** (24), 17953–17979.

27. Kresse, G., and Joubert, D. (1999) From ultrasoft pseudopotentials to the projector augmented-wave method. *Phys. Rev. B*, **59** (3), 1758–1775.

28. Kresse, G., and Hafner, J. (1993) Ab initio molecular dynamics for liquid metals. *Phys. Rev. B*, **47** (1), 558–561.

29. Kresse, G., and Hafner, J. (1994) Ab initio molecular-dynamics simulation of the liquid-metal–amorphous-semiconductor transition in germanium. *Phys. Rev. B*, **49** (20), 14251–14269.

30. Kresse, G., and Furthmüller, J. (1996) Efficiency of ab-initio total energy calculations for metals and semiconductors using a plane-wave basis set. *Comput. Mater. Sci.*, **6** (1), 15–50.

31. Kresse, G., and Furthmüller, J. (1996) Efficient iterative schemes for ab initio total-energy calculations using a plane-wave basis set. *Phys. Rev. B*, **54** (16), 11169–11186.

32. Hohenberg, P., and Kohn, W. (1964) Inhomogeneous Electron Gas. *Phys. Rev.*, **136** (3B), B864–B871.

33. Kohn, W., and Sham, L.J. (1965) Self-Consistent Equations Including Exchange and Correlation Effects. *Phys. Rev.*, **140** (4A), A1133–A1138.

34. Perdew, J.P., Burke, K., and Ernzerhof, M. (1996) Generalized Gradient Approximation Made Simple. *Phys. Rev. Lett.*, **77** (18), 3865–3868.

35. Perdew, J.P., Burke, K., and Ernzerhof, M. (1997) Generalized Gradient Approximation Made Simple [Phys. Rev. Lett. 77, 3865 (1996)]. *Phys. Rev. Lett.*, **78** (7), 1396–1396.

36. Grimme, S., Antony, J., Ehrlich, S., and Krieg, H. (2010) A consistent and accurate ab initio parametrization of density functional dispersion correction (DFT-D) for the 94 elements H-Pu. *J. Chem. Phys.*, **132** (15), 154104.

37. Karasulu, B., Vervuurt, R.H.J., Kessels, W.M.M., and Bol, A.A. (2016) Continuous and ultrathin platinum films on graphene using atomic layer

deposition: a combined computational and experimental study. *Nanoscale*, **8** (47), 19829–19845.

38. Vervuurt, R.H.J., Karasulu, B., Verheijen, M.A., et al. (2017) Uniform Atomic Layer Deposition of Al_2O_3 on Graphene by Reversible Hydrogen Plasma Functionalization. *Chem. Mater.*, **29** (5), 2090–2100.

39. Gao, W. (2015) The Chemistry of Graphene Oxide, in *Graphene Oxide*, Springer International Publishing, Cham, pp. 61–95.

40. Criado, A., Melchionna, M., Marchesan, S., and Prato, M. (2015) The Covalent Functionalization of Graphene on Substrates. *Angew. Chemie - Int. Ed.*, **54** (37), 10734–10750.

41. Lin, Y.-C., Lu, C.-C., Yeh, C.-H., et al. (2012) Graphene Annealing: How Clean Can It Be? *Nano Lett.*, **12** (1), 414–419.

42. C1s.

43. Groner, M.D., Fabreguette, F.H., Elam, J.W., and George, S.M. (2004) Low-Temperature Al_2O_3 Atomic Layer Deposition. *Chem. Mater.*, **16** (4), 639–645.

44. Eckmann, A., Felten, A., Mishchenko, A., et al. (2012) Probing the Nature of Defects in Graphene by Raman Spectroscopy. *Nano Lett.*, **12** (8), 3925–3930.

45. Van Lam, D., Kim, S.-M., Cho, Y., et al. (2014) Healing defective CVD-graphene through vapor phase treatment. *Nanoscale*, **6** (11), 5639.

46. Schwan, J., Ulrich, S., Batori, V., et al. (1996) Raman spectroscopy on amorphous carbon films. *J. Appl. Phys.*, **80** (1), 440.

47. Franklin, A.D., Han, S.-J., Bol, A.A., and Haensch, W. (2011) Effects of Nanoscale Contacts to Graphene. *IEEE Electron Device Lett.*, **32** (8), 1035–1037.

48. Meric, I., Dean, C.R., Young, A.F., et al. (2011) Channel Length Scaling in Graphene Field-Effect Transistors Studied with Pulsed Current−Voltage Measurements. *Nano Lett.*, **11** (3), 1093–1097.

49. Horiuchi, K., Nakada, K., Uchino, S., et al. (2002) Passivation effects of alumina insulating layer on C60 thin-film field-effect transistors. *Appl. Phys. Lett.*, **81** (10), 1911.

50. Ryu, S., Liu, L., Berciaud, S., et al. (2010) Atmospheric Oxygen Binding and Hole Doping in Deformed Graphene on a SiO_2 Substrate. *Nano Lett.*, **10** (12), 4944–4951.

51. Chen, F., Xia, J., Ferry, D.K., and Tao, N. (2009) Dielectric Screening Enhanced Performance in Graphene FET. *Nano Lett.*, **9** (7), 2571–2574.

52. Hoex, B., Schmidt, J., Pohl, P., et al. (2008) Silicon surface passivation by atomic layer deposited Al_2O_3. *J. Appl. Phys.*, **104** (4), 44903.

53. Oh, I.-K., Tanskanen, J., Jung, H., et al. (2015) Nucleation and Growth of the HfO_2 Dielectric Layer for Graphene-Based Devices. *Chem. Mater.*, **27** (17), 5868–5877.

54. Kim, K., Lee, H.-B.-R., Johnson, R.W., et al. (2014) Selective metal deposition at graphene line defects by atomic layer deposition. *Nat. Commun.*, **5**, 4781.

55. Elliott, S.D. (2012) Atomic-scale simulation of ALD chemistry. *Semicond. Sci. Technol.*, **27** (7), 74008.

56. Elliott, S.D., Dey, G., Maimaiti, Y., et al. (2016) Modeling Mechanism and Growth Reactions for New Nanofabrication Processes by Atomic Layer Deposition. *Adv. Mater.*, **28** (27), 5367–5380.

57. Potts, S.E., and Kessels, W.M.M. (2013) Energy-enhanced atomic layer deposition for more process and precursor versatility. *Coord. Chem. Rev.*, **257** (23–24), 3254–3270.

58. Weckman, T., and Laasonen, K. (2015) First principles study of the atomic layer deposition of alumina by TMA–H_2O-process. *Phys. Chem. Chem. Phys.*, **17** (26), 17322–17334.

59. Goumans, T.P.M., Wander, A., Brown, W.A., and Catlow, C.R.A. (2007) Structure and stability of the (001) α-quartz surface. *Phys. Chem. Chem. Phys.*, **9** (17), 2146–2152.

Chapter 4

Area-Selective Atomic Layer Deposition of Platinum Using Photosensitive Polyimide*

Abstract

Area-selective atomic layer deposition (AS-ALD) of platinum (Pt) was studied using photosensitive polyimide as a masking layer. The polyimide films were prepared by spin-coating and patterned using photolithography. AS-ALD of Pt using poly(methyl-methacrylate) (PMMA) masking layers was used as a reference. The results show that polyimide has excellent selectivity towards the Pt deposition, after 1000 ALD cycles less than a monolayer of Pt is deposited on the polyimide surface. The polyimide film could easily be removed after ALD using a hydrogen plasma, due to a combination of weakening of the polyimide resist during Pt ALD and the catalytic activity of Pt traces on the polyimide surface. Compared to PMMA for AS-ALD of Pt, polyimide has better temperature stability. This resulted in an improved uniformity of the Pt deposits and superior definition of the Pt patterns. In addition, due to the absence of reflow contamination using polyimide the nucleation phase during Pt ALD is drastically shortened. Pt patterns down to 3.5 μm were created with polyimide, a factor 10 smaller than what is possible using PMMA, at the typical Pt ALD processing temperature of 300 °C. Initial experiments indicate that after further optimization of the polyimide process Pt features down to 100 nm should be possible, which makes AS-ALD of Pt using photosensitive polyimide a promising candidate for patterning at the nanoscale.

*R.H.J. Vervuurt, A. Sharma, Y. Jiao, W.M.M. Kessels & A.A. Bol, *Nanotechnology* **27** (2016) 405302.

4.1 Introduction

Platinum (Pt) is of interest for many applications, due to its high chemical stability, catalytic properties, and excellent electronic properties. In the field of future nanoelectronics, Pt is a promising candidate for metal contacts in field-effect transistors because of its high work function of 5.6 eV and low resistivity of 10.8 μΩ·cm. For example, Pt is considered as a contact material in carbon nanotube and graphene field-effect transistors, where the high work function allows for the formation of an ohmic contact resulting in a lower contact resistance and better device performance [1,2].

To incorporate Pt in these devices, Atomic Layer Deposition (ALD) is a promising method. The self-limiting nature of the ALD process allows for the deposition of conformal and uniform Pt thin films, with sub-monolayer control over the layer thickness. The self-limiting and chemical nature gives ALD significant advantages over other vapour deposition techniques when films of low thickness, high uniformity and good conformality are required. ALD, like other gas phase deposition techniques, has no inherent growth control in the lateral dimension, which is desirable for applications in nanoelectronic devices.

To overcome this issue, area-selective ALD (AS-ALD) has gained considerable scientific interest in the last few years. AS-ALD relies on the activation or deactivation of areas on the target substrate, to prevent or promote ALD precursor adsorption [3]. This results in the selective deposition of the ALD film on the desired parts of the substrate. Currently two methods have been reported to achieve area-selectivity of Pt ALD: (1) the use of self-assembled monolayers (SAMs) [4,5], or thermally stable polymer films that block ALD growth [6–8], and (2) the use of an electron beam deposited seed-layer to promote Pt growth [9–11]. Here we will focus on the use of thermally stable polymer films that block the ALD growth of Pt.

Previous research by Färm et al. has shown that poly(methyl-methacrylate) (PMMA) can be used as blocking layer for the AS-ALD of Pt [6]. PMMA can be patterned using conventional photolithography or electron beam lithography (EBL). It is rather remarkable that PMMA can be used to selectively deposit Pt features. Typical deposition temperatures used for the ALD of Pt lie around 300 °C. This temperature is well above the melting point of PMMA of 160 °C [12]. The higher deposition temperature therefore, likely results in the reflowing of the PMMA resist, ultimately limiting the feature size.

For this reason polymers with a higher temperature stability such as poly(vinyl pyrrolidone) (PVP), and polymethacrylamide (PMAM) have been investigated as blocking layers for Pt ALD [7,8]. Successful AS-ALD of Pt using PVP could only be achieved when Al_2O_3 was used as a seed layer for Pt growth. Without a seed layer no deposition of Pt was observed in the developed areas after photolithography. This is most likely caused by PVP residues remaining in the developed areas after the lithography process. The need for an oxide seed layer to initiate growth is undesired for applications where the Pt serves as the electrode or metal contact. PMAM AS-ALD does not require a seed layer, but the selectivity of the Pt ALD process for this polymer was only investigated up to 100 cycles of Pt ALD, insufficient to form a closed Pt film [13].

In this work, photosensitive polyimide is investigated as a masking layer for the AS-ALD of Pt. Polyimide has good temperature stability (> 350 °C) and can be removed using dry chemical processing, for example by applying an CF_4-O_2 plasma [14]. The minimum Pt feature size obtainable as well as the uniformity of the Pt deposition are analysed and compared with PMMA created Pt features. It is shown that the use of polyimide improves the minimum feature size by at least a factor of 10, limited by the resolution of the lithography tool used. In addition, due to the absence of reflow contamination using polyimide, the Pt nucleation is drastically shortened.

4.2 Methods

Polyimide films were prepared by spin coating on 90 nm SiO_2 coated Si (100) wafers using Polyimide HD4101 (HD MicroSystems). Before spinning the wafers were heated to 200 °C for 5 min to remove all remaining water from the surface and improve adhesion. The spin speed was 6000 rpm for 90 s. After spinning the films were baked on a hotplate for 5 min at 100 °C. Patterning of the polyimide was performed using a Karl Suss MA6 Mask Aligner (I-line, 365 nm wavelength). The exposure time was 50 s using vacuum contact mode, at a light intensity of 9 mW/cm^2. After patterning the samples were post-baked to 80 °C for 1 min. Development of the polyimide was performed in developer PA 401D (based on cyclopentanone) for 90 s. Rinsing was done using PA400R (based on Propylene glycol methyl ether acetate). The final curing step consisted of annealing the polyimide to 375 °C for an hour in vacuum. The resulting polyimide film had a thickness of 1.5 μm, determined using a J.A. Woollam M-2000D variable angle spectroscopic ellipsometer (SE). After ALD deposition the polyimide

was removed in an Oxford instruments FlexAL reactor, using a 200W 50 mTorr H_2 plasma for 30 min.

PMMA films were prepared by spin-coating on 90 nm SiO_2 coated Si (100) wafers using PMMA A4 950k (Micro Chem). The spin speed was 4000 rpm for 1 min. After spinning the samples were baked on a hot plate at 180 °C for 5 min. This resulted in a PMMA layer thickness of 220 nm. Patterning of the PMMA films was done by EBL using a FEI Helios 650 DualBeam system, with a 30 kV e-beam and a beam current of 0.63 nA. The required patterning dose was 185–300 μC/cm^2, depending on the pattern size. The exposed PMMA film was developed in a 1:1 Methylisobutylketon: Isopropyl alcohol (IPA) solution for 60 s. Rinsing was performed in IPA for 45 s. After drying the samples were stored in darkness, to prevent light-induced degradation. After ALD, the PMMA lift-off was performed by annealing at 375 °C in Ar for 30 min.

The mask design for both EBL and photolithography consisted of circles, squares and lines in the range of 1 to 100 μm. Pt was deposited using $MeCpPtMe_3$ as the metal source and oxygen as the co-reactant at 300 °C for 1000 cycles. This resulted in a Pt layer of 50.4 nm on a bare SiO_2 substrate, determined by SE. More details on the Pt ALD process can be found elsewhere [15,16].

The patterned films were characterized before ALD, after ALD and after resist lift-off with a Zeiss Axio Imager 2 Optical microscope and a JEOL 7500 FA scanning electron microscope (SEM). The selectivity of the resists towards Pt ALD was measured by a Thermo Scientific K-Alpha KA 1066 X-ray photon electroscope (XPS). The thickness of the Pt patterns after ALD, and uniformity of the deposit was determined by energy dispersive X-ray spectroscopy (EDX) with an EDAX UMSII EDX spectrometer in combination with a SE calibrated Pt thickness series. Further details on the EDX thickness calibration can be found in appendix A.

4.3 Results and Discussion

First the selectivity of the Pt ALD process was tested, by performing 1000 cycles of Pt ALD on a PMMA and polyimide layer without patterns. The amount of Pt on the resist surface after ALD was determined with XPS to be 0.06 % and 0.45% for PMMA and polyimide, respectively. This corresponds to less than a monolayer of Pt atoms being deposited on both PMMA and polyimide, assuming a typical XPS analysis depth of 10 nm [17]. A bare SiO_2 wafer present during the same deposition was covered with 50.4 ± 0.7 nm Pt as measured by SE, indicating that both resists provide excellent selectivity for the Pt ALD process.

To obtain an indication of the possible feature sizes and the limitations of the resists, negative patterns were created for PMMA and polyimide, as shown in Figure 4.1a,c. Positive patterns were created as well and can be found in appendix B, Figure 4.8. The positive pattern helps to better visualize edge effects, for example as a result from reflowing of the resist.

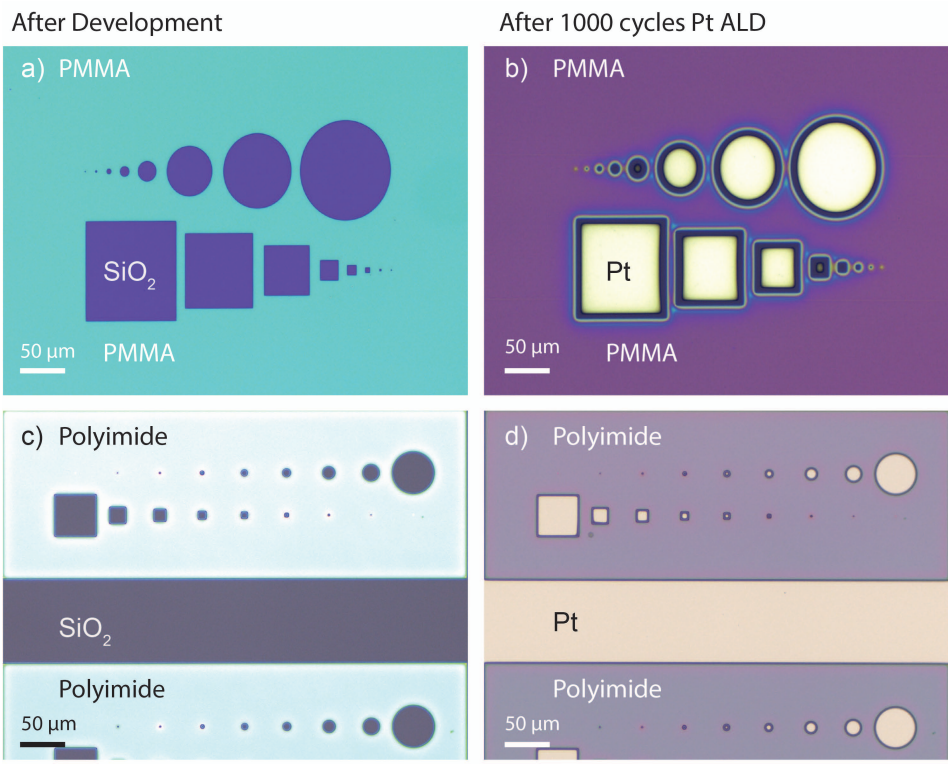


Figure 4.1: Optical microscopy images of a) PMMA pattern and c) polyimide pattern after development, and after 1000 cycles of Pt ALD without resist lift-off for b) PMMA and d) polyimide. The PMMA patterns range from 1-100 µm. The polyimide patterns from range 1-50 µm. The color change of the PMMA in b) towards the feature edges indicates a reduction in thickness due to reflowing during the ALD process.

Figure 4.1b,d show the patterned PMMA and polyimide layer after 1000 cycles of Pt ALD, before lifting off the resist. The deposition of metallic Pt is clearly visible in the developed areas, whereas no Pt deposition is visible on the polyimide and PMMA. It can be observed that close to the PMMA edges no Pt deposition is present. The size of the edge (about 5 µm) is independent of the PMMA feature size, resulting in Pt features that are around 10 µm smaller than intended. Most likely this is caused by the reflowing

of the PMMA resist at 300 °C. This assumption is supported by the change in color of the PMMA towards the feature edges in Figure 4.1b, indicating the resist gets gradually thinner towards the Pt feature.

The reason Pt deposition is not completely blocked over the full area by the reflowing of the PMMA resist is linked to the high molecular weight of the PMMA used (950 kg/mol). AS-ALD was also attempted using ZEP 520A resist, but this did not result in any Pt deposition (data not shown). Compared to PMMA, ZEP 520A has a similar temperature stability (glass transition temperature 145 °C), but a much lower molecular weight of 55 kg/mol [18]. The higher viscosity of the PMMA thus prevents reflowing to a certain extent making the deposition of Pt possible. Ultimately however, the reflowing limits the minimum feature size. Experimentally it was observed that features smaller than 10 µm contained no Pt.

The polyimide is stable to at least 375 °C, preventing reflowing of the resist during deposition. The Pt features in Figure 4.1d are therefore well defined with sharp edges and can also be smaller in size when compared to the PMMA. Pt is deposited uniformly in the features and the resulting features match openings in the polyimide resist after development. This is shown more clearly in Figure 4.2 where the dimensions of the patterns after resist development are compared with the dimensions of the Pt patterns obtained after ALD. The pattern size shown is the average of three identical patterns. The average size of the Pt patterns created using polyimide, match the opening size in the resist layer. whereas the Pt patterns created with PMMA deviate by 10 µm, due to the reflowing of the resist.

The minimum Pt feature size using polyimide, shown in Figure 4.1d, is limited to about 3.5 µm. In smaller features no Pt deposition occurs, due to polyimide residue in these features, caused by overexposure of the smaller feature sizes. The polyimide thickness of 1.5 µm in combination with the lithography tool used, results in polyimide residue covering the smaller features, and thus blocking Pt ALD growth. Features with a size down to 100 nm should, however, be possible. Figure 4.9 (appendix C) shows the creation of small ~100 nm openings in an overexposed and overdeveloped polyimide layer. In these small openings Pt can still be deposited. This indicates that the resolution is currently limited by the polyimide lithography process. The resolution can be improved using, for example, a thinner polyimide film and a more advanced lithography tool. The minimum resolution of the Karl Suss MA6 mask aligner used here, in combination with an optimized resist, is around 0.8 µm.

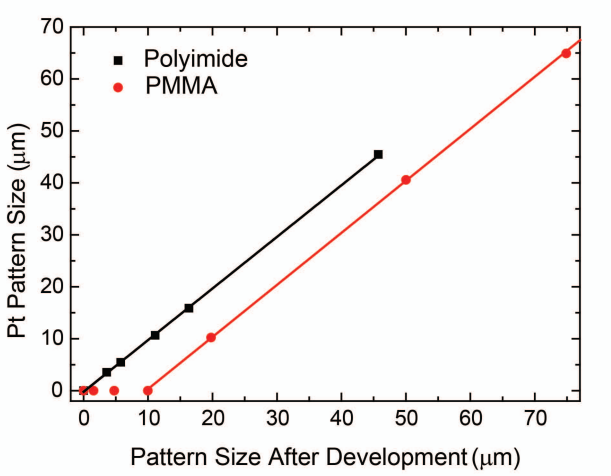


Figure 4.2: Pattern size analysis of the polyimide and PMMA patterns before and after 1000 cycles Pt ALD, shown in Figure 4.1. For the polyimide the Pt pattern sizes matches the size of those present in the resist after development. For PMMA the resist openings below 20 μm contain no Pt, the deposition is blocked by the reflowing of the resist. The error bars of the measurements are < 0.5 μm (smaller than dot size).

Figure 4.3a shows a Pt pattern created using PMMA, after lift-off. The PMMA was removed by thermal annealing at 375 °C in Ar for 30 min. Thermal annealing was chosen to lift-off the PMMA, instead of the more common wet-chemical approach with acetone, to prevent delamination of the Pt. The poor adhesion between Pt and the SiO_2 substrate can lead to delamination of the Pt when solvents are used. This is especially a problem for the larger features (> 50 μm x 50 μm).

EDX line-scans were used to get an indication of the Pt deposition uniformity (Figure 4.3b). PMMA features larger than 20 μm have a thickness of about 20 ± 2 nm, which decreases slightly towards the feature edge, resulting in a slightly rounded shape of the thickness profile. For the feature of 20 μm almost no Pt is visible. Compared to the bare SiO_2 reference wafer, on which 50.4 ± 0.7 nm of Pt was deposited, the resulting Pt feature thickness is considerably less. This is possibly caused by PMMA residuals in the cleared area in combination with the reflowing of the resist. These residues could significantly increase the nucleation delay, resulting in a reduction of the layer thickness compared to the reference SiO_2 sample [6].

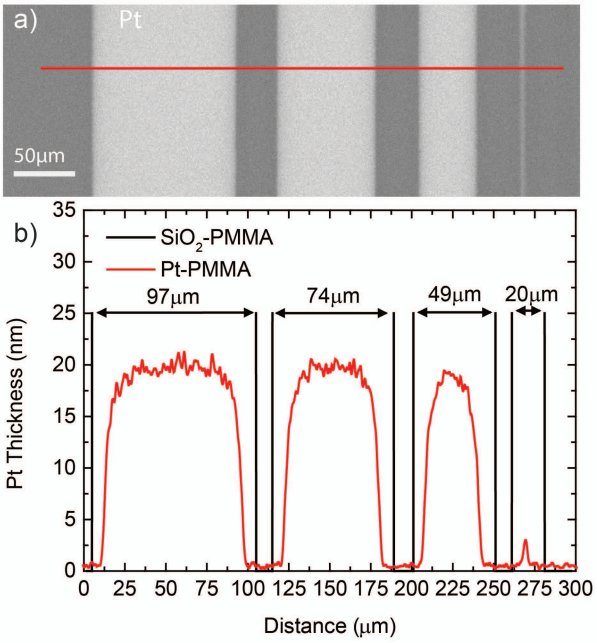


Figure 4.3: a) SEM image of PMMA pattern after 1000 cycles Pt ALD and PMMA lift-off, pattern size after development: 97, 74, 49 and 20 μm. The position of the EDX line scan is indicated by the red line. The scale bar is 50 μm b) Pt thickness determined from the EDX line scan. The scan shows that the measured feature width is smaller than intended. For the 20 μm feature almost no Pt is present.

Polyimide is conventionally removed using a CF_4-O_2 plasma. An O_2 plasma, however, can also etch or oxidize Pt [19]. To prevent this a H_2 plasma of 200 W (Ion energies < 10 eV [20]) was tried instead. Using a polyimide blanket sample without deposited Pt, the etch rate was measured using SE. After 30 min of exposure no thickness decrease was observed by SE. H_2 plasma treatments of up to 2 h did not result in a change in the polyimide thickness either. This indicates that a H_2 plasma, with the conditions used here, is not able to etch bare polyimide. However, for patterned polyimide samples exposed to the Pt ALD process all polyimide was removed after 30 min of H_2 plasma exposure, shown in Figure 4.4a.

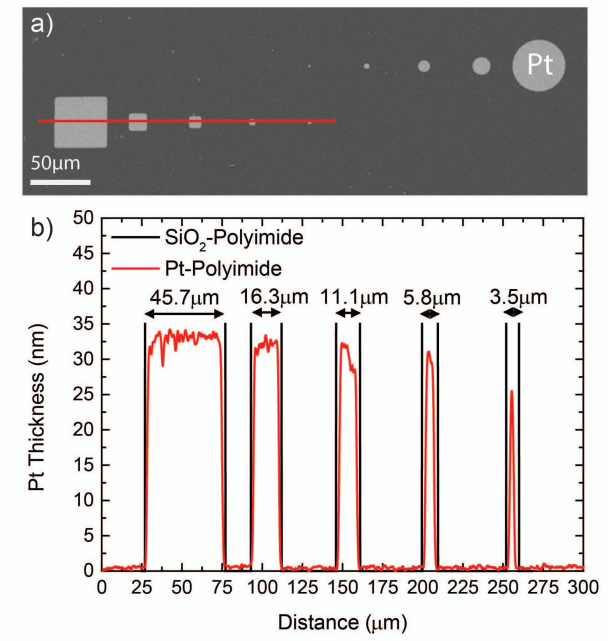


Figure 4.4: a) SEM image of polyimide pattern after 1000 cycles Pt ALD and polyimide lift-off using a H_2 plasma, pattern size after development: 45.7, 16.3, 11.1, 5.8, 3.5 μm. The position of the EDX line scan is indicated by the red line. The scale bar is 50 μm b) Pt thickness determined from the EDX line scan.

To investigate if any compositional changes occurred in the polyimide film during Pt ALD, XPS measurements were performed. XPS was performed on polyimide samples after development, and after development and 1000 cycles of Pt ALD. To make sure that the oxygen half-cycle of the ALD process at 300 °C does not affect the polyimide, a polyimide sample after development and 1000 cycles of Pt ALD where no precursor was dosed in the system was used as a reference. The XPS data can be found in the appendix D (Figure 4.10). Deconvolution of the C1s spectrum of polyimide after development indicates that 19% of the carbon is doubly bonded to oxygen and nitrogen (C=O, C=N) and 8% is singly bonded to oxygen and nitrogen (C-O, C-N). The remainder of the C1s spectra consist of C-C bonds. No changes in the bonding configuration occurred for the O_2 reference sample, for which no precursor was dosed in the system. After 1000 cycles of Pt ALD however, the amount of C=O, C=N bonding in the polyimide decreased by 10%, and a relative decrease in the oxygen content was observed. This indicates that the Pt ALD process changes the chemical structure of the

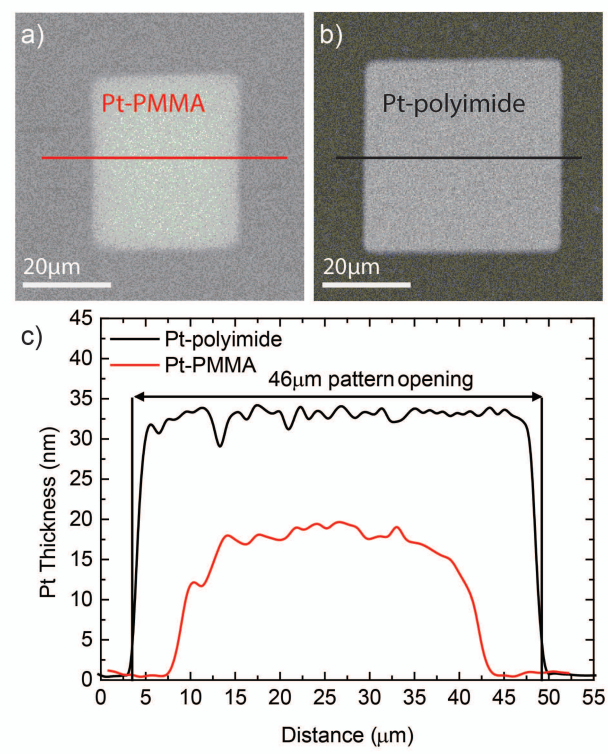


Figure 4.5: SEM image of a Pt pattern for a) PMMA and b) polyimide after resist lift-off, the pattern size after lift-off was 46µm. The position of the EDX scan is indicated by the red and black line, respectively. c) Comparison of Pt thickness determined from an EDX scan for a PMMA and polyimide defined feature.

polyimide resist, making it more susceptible to etching with a H_2 plasma. Furthermore, the trace amount of Pt (0.45%) deposited on the polyimide surface after ALD, could assist the polyimide etching. Pt is a catalyst able to dissociate H_2 molecules present in the plasma and C-H and C-O bonds present in the polyimide [21]. This could aid in the etching of the polyimide as well.

The EDX line-scans of the polyimide sample after lift-off in Figure 4.4b, show that the Pt patterns are not rounded towards the edge, as is observed for the PMMA, indicating that edge-effects do not play a role. The thickness is around 34 ± 2 nm for the larger Pt features, for the smaller features the minimum thickness is 25 ± 2 nm. This is still considerably less than the 50.4 ± 0.7 nm deposited on the SiO_2 blanket wafer. Possibly a small amount of polyimide residue is still present after polyimide development which increases the nucleation delay of the Pt deposition.

Figure 4.5 shows a direct comparison of the polyimide with the PMMA, for a positive feature of 50 µm. The PMMA feature is only 34 µm in width due to reflowing of the resist, as was observed in Figure 4.1 as well. The Pt feature created using polyimide is 46 µm in width, and equal to the opening in the polyimide resist after development. The results show that polyimide is better suited for the AS-ALD of Pt than PMMA, due to its better temperature stability.

4.4 Conclusions

In this work AS-ALD of Pt was demonstrated using photosensitive polyimide and compared with PMMA as a blocking layer. The results showed that both polyimide and PMMA possess excellent selectivity towards the Pt precursor, resulting in less than a monolayer of ALD growth on the resists after 1000 cycles. Polyimide shows superior behavior compared to PMMA when it comes to pattern stability and definition during Pt ALD at 300 °C. The Pt patterns created using PMMA are 10 µm smaller than the initial PMMA pattern openings due to reflowing of the resist. This limits the Pt feature size to 10 µm and above, unsuitable for many nanoelectronic applications. Pt patterns created using polyimide matched the pattern size present in the resist. The minimum pattern size obtained using polyimide was 3.5 µm and was limited by the polyimide lithography process used. Further optimization should make patterns down to 100 nm in width possible. The polyimide could easily be removed using a H_2 plasma, most likely due to a combination of weakening of the polyimide resist during Pt ALD and the catalytic activity of Pt traces on the polyimide surface. The results show that photosensitive polyimide is a good blocking layer to achieve AS-ALD of Pt for future nano-applications.

Acknowledgements

The authors would like to thank C.O. van Bommel, J.J.L.M. Meulendijks & J.J.A. Zeebregts for technical assistance. This work is part of the research program of the Foundation for Fundamental Research on Matter (FOM), which is part of the Netherlands Organization for Scientific Research (NWO).

4.5 Appendix A: Energy dispersive X-ray spectroscopy for Pt thickness determination

This appendix elaborates on the procedure used to determine the thickness of the Pt features created using poly(methyl-methacrylate) (PMMA) and polyimide using energy dispersive X-ray spectroscopy (EDX).

EDX can be used to determine the Pt film thickness on SiO_2 if the thickness of the Pt film is thinner than the electron beam penetration depth in Pt. Depending on the Pt thickness the intensity of the Si peak and Pt peak in the EDX spectra varies. The Pt peak increases with Pt thickness whereas the Si substrate peak decreases (Figure 4.6). The calibration shown here has been carried out on 90 nm SiO_2 on a Si (100) wafer. Since the calibration relies on the interaction between the electron beam and the substrate, it should be repeated when a different substrate material or different SiO_2 thickness is used. This is because the bulk Si contributes differently to the EDX signal depending on the thickness of the SiO_2.

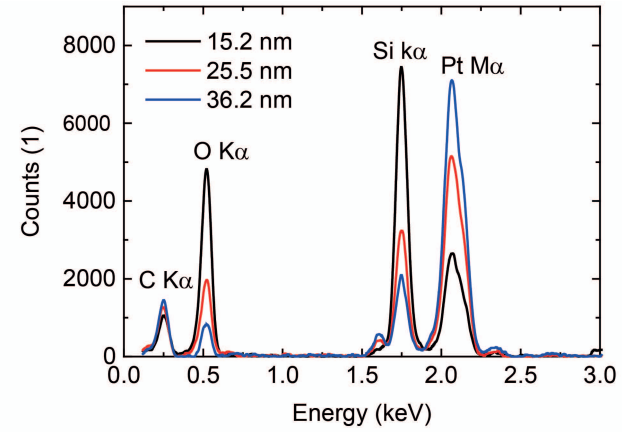


Figure 4.6: EDX spectra measured using a 5 kV electron beam for Pt films of different thickness on 90 nm SiO_2/Si. The ratio of Pt and Si peaks changes depending on the Pt thickness. The carbon peak is a result of electron beam induced deposition of background carbon and has the same height for all samples. The thickness of the Pt films was determined using Spectroscopic Ellipsometry (SE).

If the above is taken into account, the calibration is straightforward. First the relative intensity *K,* which is the ratio between integrated intensity of the 2.05 keV Mα Pt peak I_{Pt} emerging from the film and integrated intensity of the 1.74 keV Si Kα peak I_{Si} emerging from the substrate, is determined for Pt films of known thickness:

$$K_{\text{film}} = \frac{I_{\text{Pt}}}{I_{\text{Si}} + I_{\text{Pt}}} \tag{4.1}$$

A similar ratio can be defined for the substrate:

$$K_{\text{substrate}} = \frac{I_{\text{Si}}}{I_{\text{Si}} + I_{\text{Pt}}} \tag{4.2}$$

The intensity was determined from the EDX data using EDAX Genesis software, the software automatically corrects for the continuum background radiation. Using EDX data obtained from Pt samples of different thickness a calibration curve can be obtained, see Figure 4.7. Two different e-beam voltages were used to determine the Pt thickness. The 5 kV e-beam is most sensitive and can be used to determine the thickness of the thinner Pt films. However, when the Pt thickness becomes too large (> 45 nm) for the e-beam to completely penetrate a 10 kV beam should be used instead, which has a much higher penetration depth. For the same reason, however, it is also less sensitive for the Pt film thickness.

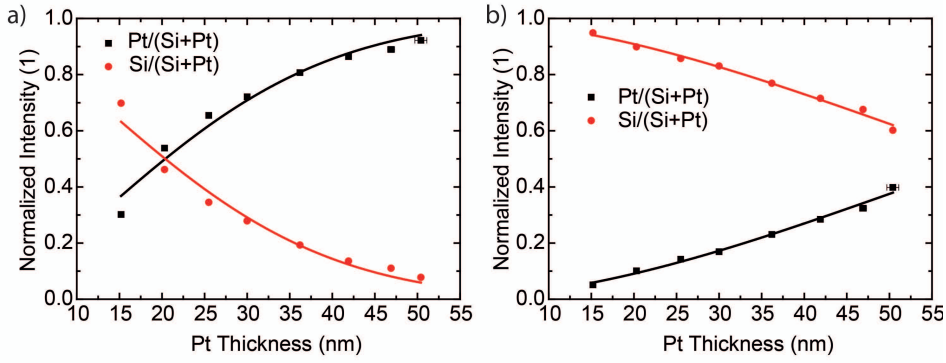


Figure 4.7: EDX calibration curves, measured using a) 5kV electron beam and b) 10 kV electron beam. The data were acquired over 100 seconds using a beam current of 1.6 and 0.5 nA, respectively, using samples of varying Pt thickness on 90 nm SiO_2 / Si (100). The thickness of the Pt films was determined using spectroscopic ellipsometry.

Using semi-empirical analytic functions the relation between the Pt and Si peak intensity can then be determined as a function of Pt thickness [22]:

$$K_{\text{film}} = \frac{I_{\text{Pt}}}{I_{\text{si}}+I_{\text{Pt}}} = \frac{Pt}{Si+Pt} = 1\text{-}e^{-(Ax+Bx^2)} \qquad (4.3)$$

$$K_{\text{substrate}} = \frac{I_{\text{si}}}{I_{\text{si}}+I_{\text{Pt}}} = \frac{Si}{(Si+Pt)} = e^{-(Cx+Dx^2)} \qquad (4.4)$$

where A, B, C and D are fit parameters and x is the films thickness. The parameters A and C take into account the attenuation of the signal due to scattering of electrons in the film. The parameters B and D take into account backscattering events. Using this calibration method the thickness of the Pt features can be determined with an accuracy of about 1- 2 nm.

4.6 Appendix B: Positive resist patterns

Figure 4.8 shows the positive patterns created in PMMA and polyimide before and after ALD. Similar as to the negative patterns no Pt deposition is observed close to the PMMA edge. A color change of the PMMA towards the feature edge can be observed for all patterns, indicating a slow decrease in thickness over several microns. This is caused by a reflowing of the PMMA resist during the ALD process, because the ALD processing temperature (300 °C) is far above the melting point of PMMA (160 °C). The higher temperature stability of polyimide prevents the resist reflowing resulting in better defined patterns.

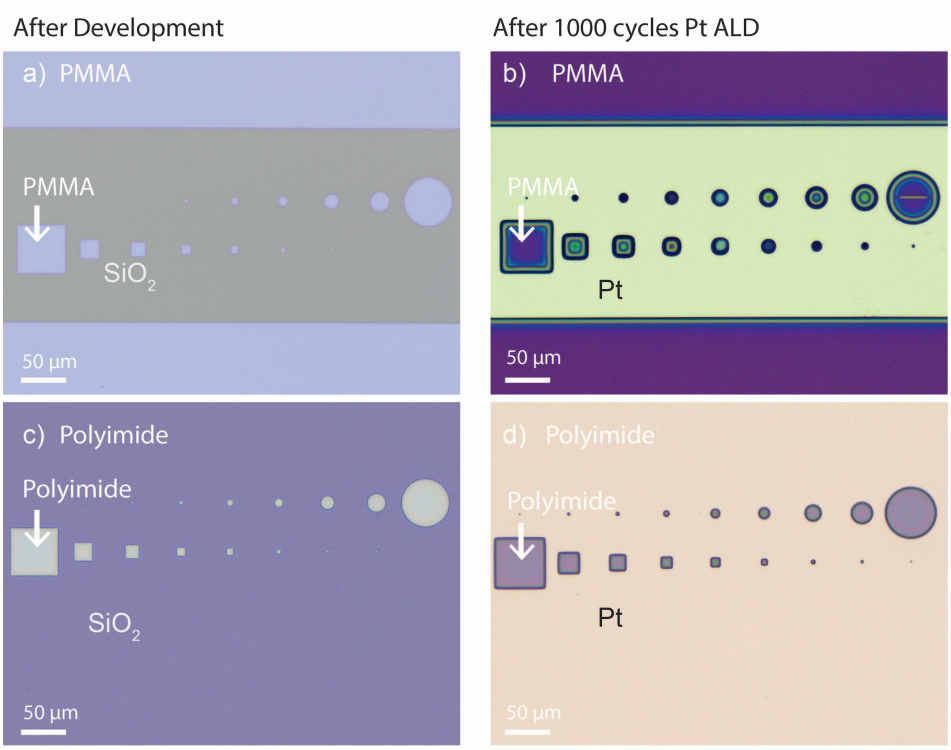


Figure 4.8: Optical microscopy image of a positive pattern in a) PMMA and c) Polyimide before ALD deposition, and after 1000 cycles of Pt ALD b) PMMA and d) Polyimide. The scale bar has a size of 50 µm. The PMMA patterns and polyimide patterns range from 1-50 µm. The color change of the PMMA in b) towards the feature edges indicates a reduction in thickness and reflowing during the ALD process.

4.7 Appendix C: Limitation on the feature size

To get an indication whether features < 3.5 µm are possible using polyimide, an overexposed polyimide feature was overdeveloped for 120 s. The overexposure results in a thin polyimide layer covering most of the feature. The overdevelopment results in small openings of ~ 100 nm in the residual polyimide layer. The thus created openings in the polyimide are much smaller than the minimum feature size that can be obtained using the Karl Suss MA6 Mask Aligner used in this work (~ 0.8 µm using an optimized resist process). Figure 4.9 shows a SEM image of the overexposed polyimide after 1000 cycles of Pt ALD. The polyimide matrix (black) that covers most of the feature is clearly visible, openings where no polyimide residue is present can be observed as well (white). EDX analysis of the openings, Figure 4.9b, reveals that Pt is deposited within

these small openings. The thickness of the Pt is approximately 12 nm. The deposition of Pt in the over developed polyimide indicates that the minimum feature size is currently limited by the polyimide lithography process. Further optimization of the polyimide lithography process, using for example, a thinner polyimide film in combination with a more advanced lithography tool, should allow for the fabrication of Pt features < 100 nm.

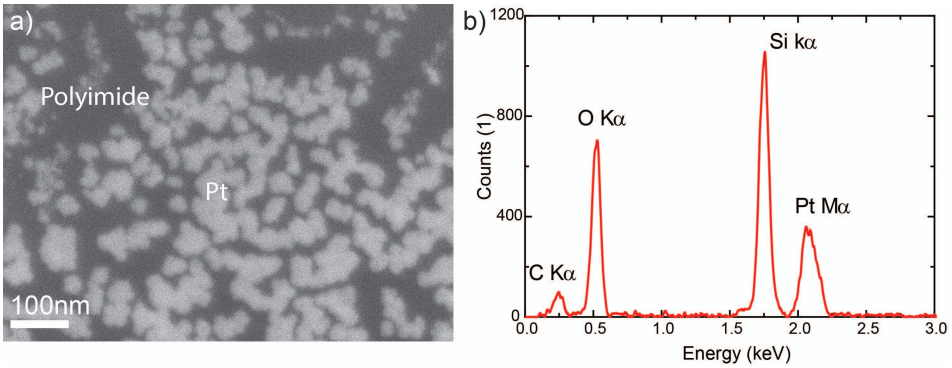


Figure 4.9: a) SEM image of an overexposed polyimide feature developed for 120 s and after 1000 cycles of Pt ALD, polyimide covers most of the feature, but small holes ~ 100 nm are visible in the where no polyimide is present. b) The EDX spectrum of the image shown in a) reveals that Pt is present in the small openings of the polyimide. Using the EDX calibration of Figure 4.7 it is established that the Pt thickness is approximately 12 nm.

4.8 Appendix D: XPS data of Polyimide after ALD

XPS measurements were performed to investigate if any compositional changes of the polyimide film take place during Pt ALD that might explain why polyimide can be etched by a H_2 plasma after Pt ALD. The XPS analysis of the polyimide core C1s level is shown in Figure 4.10. XPS was performed on polyimide samples after development, and after development and 1000 cycles of Pt ALD. To make sure the oxygen half-cycle of the ALD process at 300 °C does not affect the polyimide, a polyimide sample after development and 1000 cycles of Pt ALD where no precursor was dosed in the system was used as a reference. No changes in the polyimide occur when exposing it to 1000 ALD half-cycles using only oxygen and dosing no precursor into the system at 300 °C. After 1000 cycles of Pt ALD, however, a decrease in the C=O/C=N binding can be observed, indicating that the polyimide is partly being decomposed during Pt ALD . The oxygen content (26.0%) is much higher than the nitrogen content (5.6%). To get a better

understanding what causes this change the molecular structure of the polyimide might provide more insight, unfortunately this information is not disclosed by the supplier.

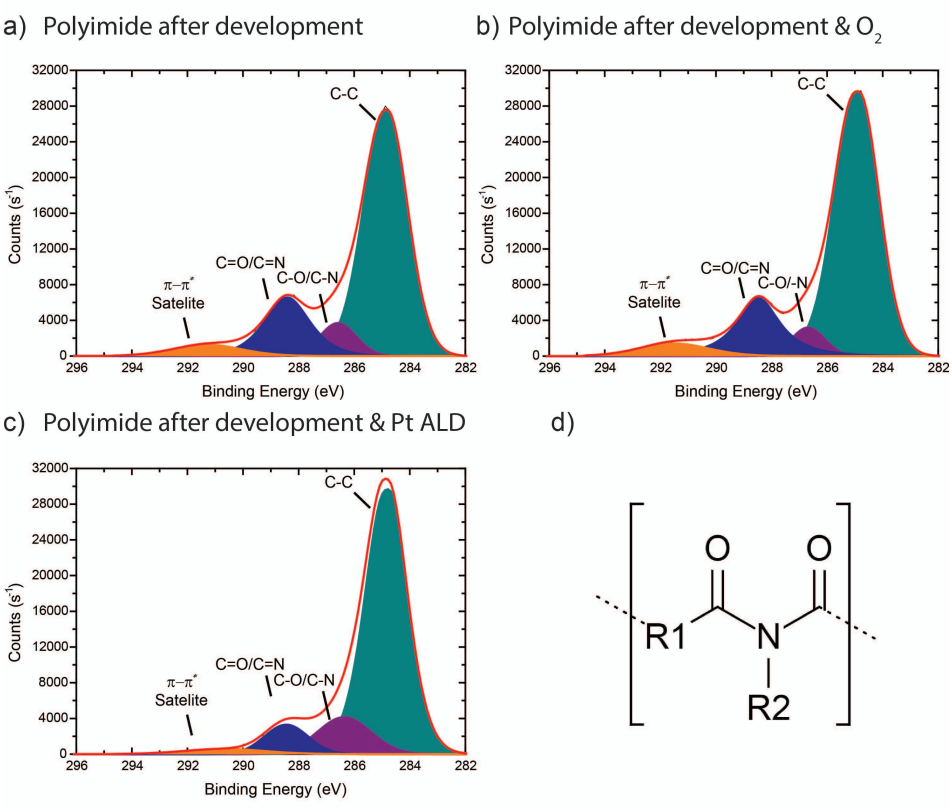


Figure 4.10: XPS spectra of the core C1s level of the polyimide a) after lift-off, b) after lift-off and 1000 ALD half-cycles using only oxygen and no precursor dose, c) after lift-lift off and 1000 cycles of Pt ALD. d) the chemical structure of polyimide, R1 and R2 are not disclosed.

References

1. Chaves, F.A., Jiménez, D., Cummings, A.W., and Roche, S. (2014) Physical model of the contact resistivity of metal-graphene junctions. *J. Appl. Phys.*, **115** (16), 164513.

2. Javey, A., Guo, J., Wang, Q., et al. (2003) Ballistic carbon nanotube field-effect transistors. *Nature*, **424** (6949), 654–657.

3. Mackus, A.J.M., Bol, A.A., and Kessels, W.M.M. (2014) The use of atomic layer deposition in advanced nanopatterning. *Nanoscale*, **6** (19), 10941–10960.

4. Chen, R., and Bent, S.F. (2006) Chemistry for Positive Pattern Transfer Using Area-Selective Atomic Layer Deposition. *Adv. Mater.*, **18** (8), 1086–1090.

5. Jiang, X., Chen, R., and Bent, S.F. (2007) Spatial control over atomic layer deposition using microcontact-printed resists. *Surf. Coatings Technol.*, **201** (22–23), 8799–8807.

6. Färm, E., Kemell, M., Ritala, M., and Leskelä, M. (2008) Selective-Area Atomic Layer Deposition Using Poly(methyl methacrylate) Films as Mask Layers. *J. Phys. Chem. C*, **112** (40), 15791–15795.

7. Färm, E., Kemell, M., Santala, E., et al. (2010) Selective-Area Atomic Layer Deposition Using Poly(vinyl pyrrolidone) as a Passivation Layer. *J. Electrochem. Soc.*, **157**, K10.

8. Mullings, M.N., Lee, H.-B.-R., Marchack, N., et al. (2010) Area Selective Atomic Layer Deposition by Microcontact Printing with a Water-Soluble Polymer. *J. Electrochem. Soc.*, **157** (12), D600.

9. Mackus, A.J.M., Mulders, J.J.L., van de Sanden, M.C.M., and Kessels, W.M.M. (2010) Local deposition of high-purity Pt nanostructures by combining electron beam induced deposition and atomic layer deposition. *J. Appl. Phys.*, **107** (11), 116102.

10. Mackus, A.J.M., Dielissen, S.A.F., Mulders, J.J.L., and Kessels, W.M.M. (2012) Nanopatterning by direct-write atomic layer deposition. *Nanoscale*, **4** (15), 4477.

11. Mackus, A.J.M., Thissen, N.F.W., Mulders, J.J.L., et al. (2013) Direct-Write Atomic Layer Deposition of High-Quality Pt Nanostructures: Selective Growth Conditions and Seed Layer Requirements. *J. Phys. Chem. C*, **117** (20), 10788–10798.

12. Smith, W.F., and Hashemi, J. (2005) *Foundations of materials science and engineering*, McGraw-Hill, Boston.

13. Mackus, A.J.M., Verheijen, M.A., Leick, N., et al. (2013) Influence of Oxygen Exposure on the Nucleation of Platinum Atomic Layer Deposition: Consequences for Film Growth, Nanopatterning, and Nanoparticle Synthesis. *Chem. Mater.*, **25** (9), 1905–1911.

14. Turban, G., and Rapeaux, M. (1983) Dry Etching of Polyimide in O2-CF4, and O2-SF6 Plasmas. *J. Electrochem. Soc.*, **120**, 2231–2236.

15. Aaltonen, T., Ritala, M., Sajavaara, T., et al. (2003) Atomic Layer Deposition of Platinum Thin Films. *Chem. Mater.*, **15** (9), 1924–1928.

16. Knoops, H.C.M., Mackus, A.J.M., Donders, M.E., et al. (2009) Remote Plasma ALD of Platinum and Platinum Oxide Films. *Electrochem. Solid-State Lett.*, **12** (7), G34.

17. Techane, S.D., Gamble, L.J., and Castner, D.G. (2011) X-ray photoelectron spectroscopy characterization of gold nanoparticles functionalized with amine-terminated alkanethiols. *Biointerphases*, **6** (3), 98.

18. Nishida, T., Notomi, M., Iga, R., and Tamamura, T. (1992) Quantum Wire Fabrication by E-Beam Elithography Using High-Resolution and High-Sensitivity E-Beam Resist ZEP-520. *Jpn. J. Appl. Phys.*, **31** (Part 1, No. 12B), 4508–4514.

19. Shibano, T. (1998) Platinum etching in Ar/O_2 mixed gas plasma with a thin SiO2 etching mask. *J. Vac. Sci. Technol. A Vacuum, Surfaces, Film.*, **16** (2), 502.

20. Profijt, H.B., Potts, S.E., van de Sanden, M.C.M., and Kessels, W.M.M. (2011) Plasma-Assisted Atomic Layer Deposition: Basics, Opportunities, and Challenges. *J. Vac. Sci. Technol. A Vacuum, Surfaces, Film.*, **29** (5), 50801.

21. Freyschlag, C.G., and Madix, R.J. (2011) Precious metal magic: catalytic wizardry. *Mater. Today*, **14** (4), 134–142.

22. Campos, C.S., Coleoni, E.A., Trinacavelli, J.C., et al. (2001) Metallic thin films thickness determination using electron probe microanalysis. *X-Ray Spectrom.*, **30**, 253–259.

Chapter 5

Pt-Graphene Contacts Fabricated by Plasma Functionalization and Atomic Layer Deposition*

Abstract

Pt-graphene contacts were fabricated by atomic layer deposition (ALD) on H_2 and O_2 plasma functionalized graphene. The plasma functionalization of graphene enabled the growth of uniform Pt layers on graphene by ALD and improved the Pt-graphene interaction, which resulted in a reduced Pt-graphene contact resistance. Devices created using a H_2 plasma treatment before Pt ALD performed considerably better than the ones created using O_2 plasma treatments (R_c = 0.4 ± 0.2 kΩ·μm and R_c = 1.2 ± 0.1 kΩ·μm, respectively). The lower performance of the O_2 plasma treatments was attributed to a less favorable Pt-graphene oxide interaction and the amorphization of graphene due to the O_2 plasma interaction. Supporting the latter, density functional theory (DFT) calculations indicated that the C-H groups created by a H_2 plasma treatment leave the π-conjugation (by C-p_z orbitals) of graphene largely intact, resulting in good in-plane and out-of-plane conductivity. The C-O groups formed by an O_2 plasma treatment however disturb the C-p_z character, deteriorating the in-plane conduction of graphene, despite the good out-of-plane conduction. The results indicate that the treatment of graphene by H_2 plasma is a straightforward approach to improve the ALD growth on graphene and reduce the Pt-graphene contact resistance.

---

* R.H.J. Vervuurt, B. Karasulu, N.W.F. Thissen, Y. Jiao, J.W. Weber, W.M.M. Kessels & A.A. Bol, to be submitted.

5.1 Introduction

Graphene is a promising candidate for post-silicon optical and electronic applications, due to its outstanding electronic, optical and thermal properties. The high intrinsic charge carrier mobility and large maximum current density make it a favorable channel material to be used in, for example, radio frequency electronic devices, [1,2] while its broad band absorption makes it suitable for use in high speed photodetectors [3]. To further improve graphene device performance and make optimum use of graphene's properties, the ability to deposit high quality metal contacts on graphene is required [4,5]. Above all, the resistance between the contact metal and the graphene has to be low, typically less than 10% of the total device resistance. Despite significant advances over the past few years, the contact resistances typically obtained are often still several times higher than required and therefore this remains a bottleneck for future device applications.

The metal-graphene contact resistance is influenced by a number of material and device parameters including the work function of the contact metal [6–9], the interaction strength between the contact metal and the graphene [7,8], the type of contact (top or edge) [5,10–12], and the possible presence of resist residue (from graphene transfer or patterning processes) between the metal and the graphene [13–15]. Different contact metals have been tested in the literature (Ni, Cu, Pd, Ti, Au, Ag etc.), to minimize the contact resistance. Each metal offers certain advantages and disadvantages in terms of interaction strength with the graphene and shift of the Fermi level (contact doping) [6–9]. In general the stronger interacting metals (Pd, Ni and Ti) have been shown to lead to a lower contact resistance. Theoretical work has shown that Pt might also give a high-quality metal graphene contact, due to its high work function [9]. However, compared to Pd, Pt generally has difficulty wetting carbon surfaces, resulting in non-uniform films and a high contact resistance [16].

It has been suggested in the literature that using alternative metallization schemes such as atomic layer deposition (ALD) might further lower the contact resistance [5,17]. The chemical nature of ALD could lead to an improved metal graphene interaction strength compared to physical vapor deposition (PVD) techniques. Furthermore, ALD has been shown to enhance the wetting of Pt on carbon nanotubes [18]. However, the lack of dangling bonds and the hydrophobicity of the graphene makes it difficult to initialize ALD growth on graphene [19]. For example, Pt ALD on graphene leads to the preferential deposition of Pt on the graphene grain boundaries and defect sites [20].

Though this offers opportunities for catalytic applications, this growth characteristic makes Pt ALD currently unsuitable for the deposition of metal-graphene contacts.

The difficulty of ALD to nucleate on graphene has also been observed for the deposition of metal-oxides on graphene [21,22]. In the literature different surface modification techniques have been shown to enable uniform metal-oxide ALD through the creation of nucleation sites on the graphene that enable ALD precursor adsorption [23–26]. These nucleation sites can be functional groups which are either chemisorbed or physisorbed on the graphene surface or they can be seed-layers deposited by, for example, e-beam evaporation. Among the various modification techniques surface functionalization techniques, such as ozone [27,28] or plasma treatments [29–31], are of particular interest for the fabrication of contacts to graphene. This is because these surface functionalization techniques often change the graphene basal plane by converting the sp^2-C bonds to sp^3 bonds upon plasma exposure through the creation of chemisorbed functional groups [30]. While this conversion to sp^3carbon is unwanted if the graphene is used as a channel material, it has been shown in the literature that plasma treatments of graphene under the metal contacts can aid in the injection and extraction of carriers into the graphene. This can lower the contact resistance, a result of the improved metal-graphene interaction [12,32–34]. Furthermore, the plasma treatment removes polymer residues remaining on the graphene from the graphene transfer process that would normally prevent a good contact between the graphene and the contact metal [32]. The use of plasma functionalization in combination with Pt ALD therefore might make it possible to deposit Pt uniformly on graphene, while simultaneously improving the Pt-graphene contact resistance.

In this work, Pt-graphene contacts have fabricated by ALD on H_2 and O_2 plasma functionalized graphene. The influence of H_2 and O_2 plasma treatments on the Pt-graphene interaction, and the resulting contact resistance is investigated. First the effect of H_2 and O_2 plasma treatment on the structural properties of graphene is examined by Raman spectroscopy, and X-ray photoelectron spectroscopy (XPS). The functional groups created by the H_2 and O_2 plasma pretreatments make it possible to uniformly grow Pt on graphene by ALD. Area-selectivity of the Pt ALD process is achieved using photosensitive polyimide as the blocking layer. Polyimide is used to accommodate the relatively high processing temperature of thermal Pt ALD (300 °C) [35]. This makes it possible to fabricate circular transfer length method (CTLM) structures to determine the quality of the Pt ALD-graphene contacts, and investigate the effect of the plasma treatment time on the contact resistance. The Pt ALD devices are compared to reference Pt-graphene devices fabricated by electron beam lithography (EBL) and e-beam

evaporation. Furthermore, *ab initio* calculations are used to gain insight into the influence of the H_2 and O_2 plasma treatments on the Pt-graphene interaction at a molecular level. Specifically, changes in the in-plane and out-of-plane conductivity as a consequence of the attachment of hydrogen and oxygen containing functional groups and their influence on the contact resistances are investigated.

5.2 Methods

5.2.1 Experimental Methods

Graphene growth. Large-area graphene was grown on Cu foil (Alfa Aesar 99.8, No 13382) by chemical vapor deposition (CVD). The Cu foil was cleaned before growth in acetone and methanol followed by a 30 s 1.0 M HNO_3 etch to remove the surface oxide. After rinsing in DI water the Cu foil was dried and loaded into a tube furnace. The graphene was grown by a two-step process. First, the Cu foil was heated to 1050 °C and annealed in an Ar/H_2 flow (500/10 sccm) at a pressure of 0.4 Torr. After 30 min the H_2 flow was reduced to 6 sccm and 100 sccm CH_4 was added to the gas flow, resulting in monolayer graphene coverage after 20 min. The sample was cooled down to room temperature in 15 min while leaving the gas flows on.

Graphene transfer. Following growth, the graphene was transferred to 90 nm SiO_2/Si (100) substrates using poly(methyl methacrylate) (PMMA) A4 950k (Micro Chem.) as a support layer. Ammonium persulfate ($(NH_4)_2S_2O_8$ 0.1 M) was used to etch the Cu. After transfer the PMMA was removed using acetone followed by a final rinse in methanol. Finally, the samples were annealed at 400 °C in an Ar/H_2 atmosphere for 2 h, to minimize any PMMA residue remaining on the graphene surface after PMMA lift-off.

Graphene functionalization. Graphene functionalization was performed by H_2 and O_2 plasma treatments in an Oxford Instruments FlexAL reactor using a 100 W, 50 mTorr plasma at 50 °C. The base pressure of the system was $< 1 \cdot 10^{-6}$ Torr. The creation of functional groups was monitored by a Renishaw Invia Raman microscope (514.5 nm) and Thermo Scientific K-Alpha KA 1066 X-ray photon spectroscope (XPS).

Pt atomic layer deposition. To investigate the effect of the functionalization on the Pt coverage after ALD, 500 cycles of Pt ALD were performed on the plasma treated graphene samples. As a reference also a pristine graphene sample was added. The ALD process consisted of a $MeCpPtMe_3$ precursor dose and an O_2 reaction step, separated by pump steps, at a temperature of 300 °C. Additional details on the Pt ALD process can

be found elsewhere [35,36]. After ALD the Pt coverage on graphene was analyzed by a JEOL 7500 FA scanning electron microscope (SEM).

Device Fabrication. To evaluate the properties of the Pt-graphene, contacts circular transfer length method (CTLM) structures, consisting of rings with an inner diameter of 100 μm and outer diameter ranging between 110 and 200 μm, were created by photolithography of photosensitive polyimide. Polyimide acts as a blocking layer during Pt ALD, preventing $MeCpPtMe_3$ precursor adsorption where polyimide is present. This makes it possible to selectively deposit the Pt on graphene. Further details on the polyimide lithography process can be found elsewhere [35]. For the created CTLM structures H_2 and O_2 plasma treatments were performed after polyimide lithography, to prevent damage to the graphene channel. No Pt deposition occurred on the polyimide when it was treated with a plasma, indicating that the selectivity of the Pt ALD process was not affected. After plasma functionalization 1000 cycles of Pt ALD were performed at 300 °C. This resulted in a Pt thickness of ~ 36 nm on the plasma treated graphene. The thickness was determined by energy dispersive X-ray spectroscopy (EDX) with an EDAX UMSII EDX spectrometer. More details on the AS-ALD process can be found elsewhere [35].

Reference CTLM structures were created by electron beam lithography (EBL) using PMMA as the resist material. The patterning was done in a Raith EBPG5150 system, with a 100 kV e-beam and a beam current of 100 nA. The required patterning dose ranged between 750 and 900 $\mu C/cm^2$, depending on the pattern dimensions. For some samples H_2 plasma treatments were performed after the EBL patterning to functionalize the graphene. For the contacts 35 nm of Pt was evaporated by a Temescal FC2000 e-beam evaporator, to prevent contact delamination a 1 nm Ti adhesion layer was used.

Device characterization. The CTLM structures were analyzed using a Janis micro-manipulated vacuum probe station with a Keithley 4200-SCS parameter analyzer. The samples were annealed overnight at 475 K in vacuum ($\sim 10^{-4}$ mbar) to reduce the ambient doping of the graphene and improve measurement reproducibility. Measurements were carried out in a two-probe configuration at room temperature under vacuum, a minimum of 6 devices (for 9 different channel lengths) were measured per sample.

5.2.2 Computational Methods

The orbital-projected density of states (DOS) and band diagrams of pristine graphene (PG), oxygenated graphene (GO) and single-sided hydrogenated graphene (SSHG) with and without Pt contacts were determined by density functional theory (DFT). The DFT calculations were performed using the projector augmented wavefunction (PAW) [37,38] method as implemented in Vienna Ab Initio Simulation Package (VASP v.5.4.1) [39–42]. Local-density approximation (LDA) [41] was utilized in view of its capability to predict the graphene electronic and structural properties on different substrates [7,8,43,44]. To account for the dispersion effects (e.g. van der Waals interactions) the van der Waals density functional (vdW-DF2) [45,46] was used in combination with the generalized gradient approximation (GGA) [47,48]. The vdW-DF2 is expected to give a better description of the dispersion effects by considering non-local additions to the exchange correlation functional. In view of the detailed comparison of two functionals, LDA was used for structures and vdW-DF2 for DOS and band diagrams. DFT with different functionals is commonly employed for probing the electronic and structural properties of pristine and functionalized graphene, either isolated or on a metal substrate [49–55].

The electronic DOS and band diagrams of graphene analogues were predicted using a collection of periodic models consisting of: PG, GO with a linear epoxy-group decoration and SSHG, with a honeycomb decoration model (see Figure S7). In addition to the free-standing (isolated) graphene derivatives, their interfaces to the top/surface or side/edge Pt-metal contacts were also considered for the DFT calculations. For simulating the contacts, two Pt models, namely 4-layer Pt(111) and Pt(220)-rocksalt-like, were employed alongside the graphene models. However, only the Pt(111) results are included here for brevity (see [56] for a detailed discussion). To augment the understanding of the complex band structures of the graphene-Pt junctions/contacts, the BandUP method by Medeiros *et al.* was used. This approach unfolds the bands of a given supercell onto one of its available primitive cells [49,50]. The Bader charge partition scheme [57] was employed for estimating the charge transfer from the graphene to Pt. A dipole correction scheme was also considered, as implemented in VASP [58], along with the spin-polarization formalism.

5.3 Results & Discussion

5.3.1 Influence of plasma functionalization on the properties of graphene

To study the functional groups created by the H_2 and O_2 plasma, and how the plasma treatments affect the structure of the graphene, XPS and Raman spectroscopy were used to analyze the plasma treated graphene samples. XPS provides information on the various surface groups created during the plasma exposure, while Raman spectroscopy can be used to monitor the structure of the graphene [59–61]. Before plasma functionalization the graphene samples were annealed at 400 °C in a 5% Ar/H_2 mixture for 2 h, to minimize the polymer residues on the graphene as a result of the transfer process to SiO_2/Si substrates [62]. XPS measurements were performed on a graphene sample treated with a 5 min H_2 or 5 min O_2 plasma, and compared with a pristine graphene sample. The XPS measurements of the C 1s spectrum are shown in Figure 5.1. The main contribution for pristine graphene is related to sp^2-C (97.5%). In addition, a small amount (2.5%) of C-O bonding can be observed, possibly related to polymer residues remaining on the graphene or surface groups present at defect sites and grain boundaries [62]. A 5 min H_2 plasma treatment results in the partial conversion of sp^2-C to sp^3 bonds (23%). Although C-H bonds cannot be observed directly by XPS, the conversion of sp^2 to sp^3 is a good indication for the formation of these bonds [31]. The treatment of the graphene by a 5 min O_2 plasma results in an increase in the amount of C-O bonding (17.3%), indicating the creation of epoxy (C-O-C) or hydroxyl (C-OH) groups on the graphene. Furthermore C=O bonds (4.9%) are formed, most likely in the form of carbonyl groups. Carbonyl groups do not distort the sp^2-C configuration, therefore they are most likely formed at the edges of the graphene or incorporated in the graphene lattice as defects.

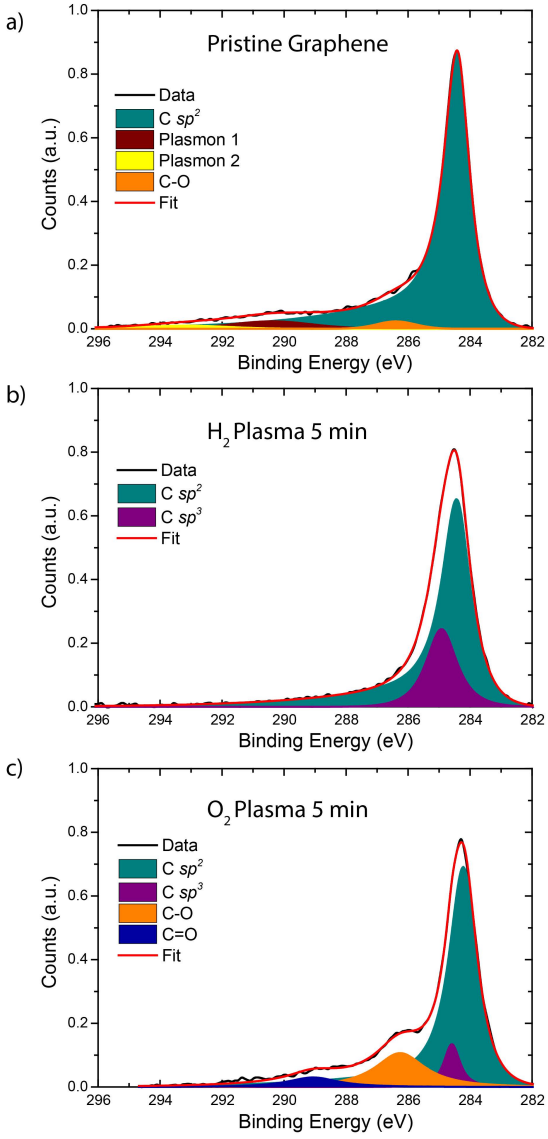


Figure 5.1: XPS spectra of the core level C 1s of a) pristine graphene, b) graphene after 5 min of H_2 plasma treatment and c) graphene after 5 min O_2 plasma treatment. Both plasma treatments were performed at a pressure of 50 mTorr and power of 100 W.

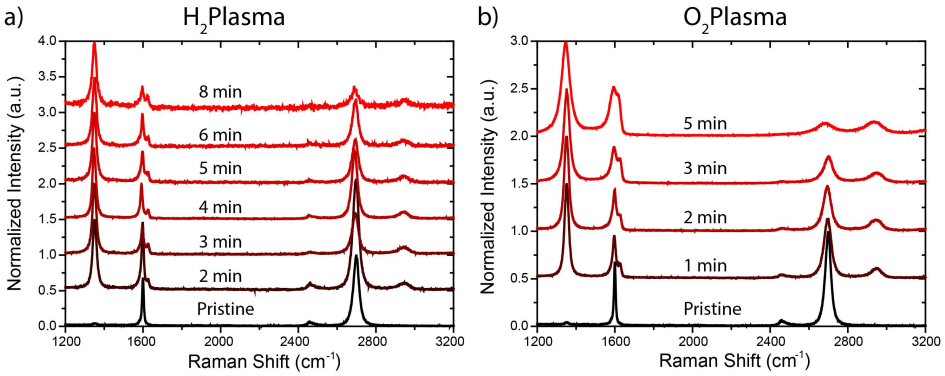


Figure 5.2: Raman spectra obtained after different plasma treatments for a) H_2 plasma treatments ranging from 2 to 8 min and b) O_2 plasma treatments from 1 to 5 min. As a reference the Raman spectrum of pristine graphene is also added. The Raman spectra are normalized to the highest peak (D band at 1350 cm^{-1} or 2D band 2690 cm^{-1}) and are vertically offset for clarity.

To confirm the change in hybridization and the formation of functional groups observed by XPS, Raman spectroscopy measurements were performed on graphene samples exposed to H_2 and O_2 plasmas for different durations. Figure 5.2a shows the Raman spectra obtained for graphene exposed to H_2 plasmas for 2-8 min. Figure 5.2b shows graphene treated with an O_2 plasma, for 1- 5 min together with a reference spectrum of pristine graphene. The H_2 and O_2 plasma functionalization both lead to the formation of a D-band (~1350 cm^{-1}) and D'-band (~1650 cm^{-1}), which are related to the functionalization of graphene or the formation of defects [60]. The D to D' ratio can be used to distinguish between the formation of defects and functionalization [61]. A ratio of ~13 is indicative for the conversion from sp^2 to sp^3 carbon bonds as a result of the formation of functional groups, while a ratio of ~7 indicates the formation of lattice defects [61].

The D/D' ratio for the H_2 and O_2 plasma treatments is plotted in Figure 5.3a. H_2 plasma functionalization predominantly functionalizes the graphene (D/D' ~ 10). The ratio also remains more or less constant as a function for plasma treatment times ≥ 3 min. This indicates that the relative amount of functionalization compared to defects stays constant even though the graphene is slowly being etched by the H_2 plasma. After a H_2 plasma of 10 min the graphene was completely etched and no peaks related to carbon were observed by Raman Spectroscopy (data not shown). Similar to a H_2 plasma treatment, an O_2 plasma treatment predominantly functionalizes the graphene (D/D' ~ 10) for plasma treatment times below 3 min. Longer plasma treatments however, result in the formation of defects in the graphene (D/D' < 7). Compared to the H_2 plasma the

peaks present in the Raman spectra for the O_2 plasma treatment also significantly broaden with increasing plasma treatment time. This is illustrated in Figure 5.3b, where the width of the G-band (~1600 cm^{-1}) and 2D-band (~2690 cm^{-1}) is plotted as a function of the plasma treatment time. For a H_2 plasma treatment the G and 2D-band broaden by 10 cm^{-1} after 8 min of plasma exposure, while for an O_2 plasma treatment the G-band broadens by 37 cm^{-1} and the 2D-band by 70 cm^{-1} after 5 min. This broadening is most likely due to the amorphization of the graphene [59] as a result of the O_2 plasma treatment.

Summarizing, the H_2 plasma treatment results in the creation of C-H groups on the graphene and leaves the structure of the graphene mostly intact, although some defects are created. The O_2 plasma treatment results in the formation of epoxide, hydroxide and carbonyl groups. The formation of these groups significantly alters the graphene structure, evident by the amorphization of the graphene after 2 min of O_2 plasma exposure.

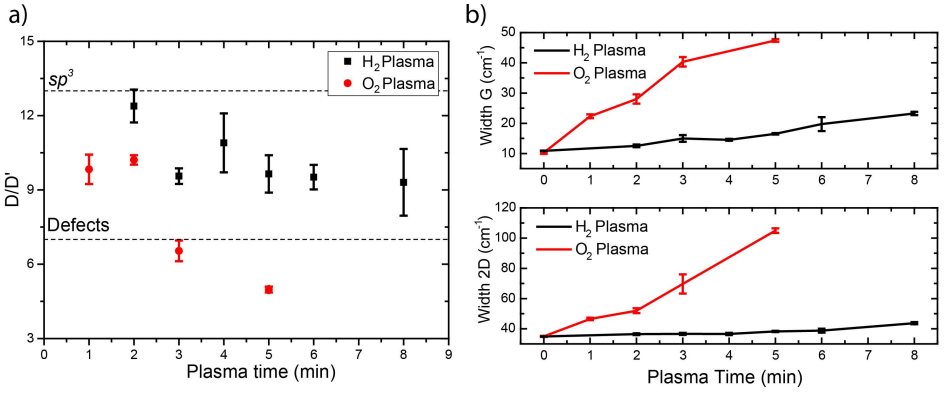


Figure 5.3: a) D/D' Ratio of the graphene spectra for the different H_2 and O_2 plasma treatment times and b) broadening of the Raman G and 2D band as function of the plasma treatment time, determined from the data in Figure 5.2.

Summarizing, the H_2 plasma treatment results in the creation of C-H groups on the graphene and leaves the structure of the graphene mostly intact, although some defects are created. The O_2 plasma treatment results in the formation of epoxide, hydroxide and carbonyl groups. The formation of these groups significantly alters the graphene structure, evident by the amorphization of the graphene after 2 min of O_2 plasma exposure.

5.3.2 Pt ALD on pristine graphene and plasma functionalized graphene

For the fabrication of Pt-graphene contacts uniform growth of Pt on graphene is required. Pt ALD on pristine graphene however, generally leads to preferential Pt growth on wrinkles, grain boundaries and defects, due to the lack of reactive surface sites and the hydrophobic nature of the graphene surface. This has been shown previously by Kim *et al*. and Karasulu *et al*. [19,20], and is reiterated here for comparison (see Figure 5.4). Figure 5.4a shows the pristine graphene before ALD, imaged using Scanning Electron Microscopy (SEM). The wrinkles and bilayer spots present in the graphene are indicated in the figure. After 500 cycles of Pt ALD (Figure 5.4b), no uniform growth of Pt is observed on the graphene. Instead Pt growth is observed only on wrinkles, grain boundaries and defect sites while no growth occurs on the graphene basal plane, due to the lack of reactive surface sites. This confirms the results reported previously [19,20].

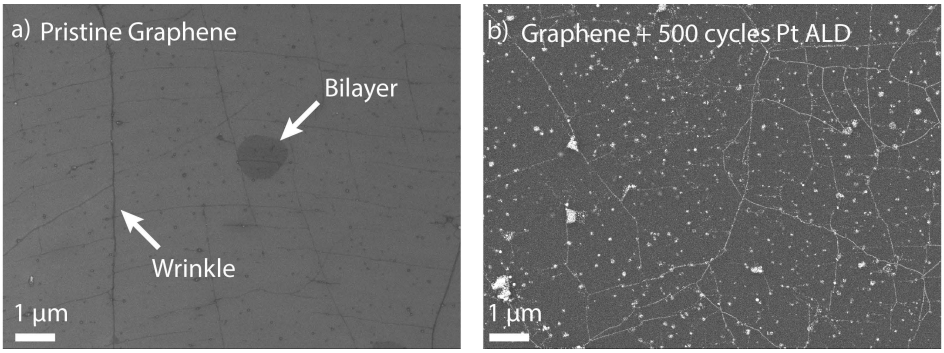


Figure 5.4: a) SEM image of pristine graphene after transfer to SiO_2 and anneal at 400 °C. Wrinkles and bilayer graphene are visible in the image. b) SEM image of pristine graphene after 500 cycles of Pt ALD at 300 °C. Preferential Pt growth occurs on the graphene wrinkles, grain boundaries and defects sites.

The effect of H_2 and O_2 plasma treatments on the nucleation of Pt ALD is shown in Figure 5.5. The SEM images show an increase of the Pt coverage as a function of both the H_2 and O_2 plasma treatment time. The functional groups created by both the H_2 plasma and the O_2 plasma enhance the ALD precursor adsorption on graphene. Small Pt particles are present all over the graphene for a H_2 plasma treatment time of 2 min. The size of these particles increases as a function of the plasma treatment time until a closed

Pt layer is obtained for a plasma treatment time of 5 min. The thickness of the Pt layer on graphene after closure was determined to be 16 ± 2 nm. The thickness was obtained by EDX analysis using Pt samples with a known thickness for calibration [35]. Increasing the plasma exposure resulted in a gradual increase of the thickness after 500 cycles of Pt ALD to 19 ± 2 nm for the 8 min H_2 plasma exposure, indicating a reduction in the nucleation delay. The O_2 plasma treatments show a similar trend; for short plasma treatment times Pt particles start to appear over the entire graphene surface and the Pt coverage increases for longer plasma times. 5 min of O_2 plasma treatment leads to an almost closed layer of Pt. The thickness of the areas covered with Pt is 18 ± 2 nm.

The basal plane of the graphene is more quickly covered with Pt when treated with an O_2 plasma (3 min), compared to a H_2 plasma treatment. This could indicate a stronger adsorption of the Pt precursor on the epoxide, hydroxide and carbonyl groups created by the O_2 plasma compared to the C-H groups created by the H_2 plasma treatment. The enhanced adsorption of ALD precursor molecules on O_2 plasma treated graphene compared to H_2 plasma treated graphene has also been observed experimentally for the adsorption of trimethylaluminum (TMA) and was confirmed by DFT calculations [31]. On the contrary, large wrinkles present in the graphene are more difficult to cover by using O_2 plasma functionalization compared to a H_2 plasma (the black lines present in Figure 5.5d,e and f). The reduced growth observed on the large wrinkles for the O_2 plasma treatment could indicate that it is more difficult for an O_2 plasma to create functional groups on or in these wrinkles. This could be caused by polymer residues (PMMA) remaining on the graphene after the graphene transfer process. The polymer residue remaining after the graphene transfer tends to gather at the wrinkles due to their enhanced reactivity [63]. The ALD of Pt is blocked by this residue [20,64]. Therefore, depending on how quickly the plasma is able to remove or functionalize the residue, it can take longer for growth to occur on these wrinkles. The H_2 plasma is likely able to remove these residues and functionalize the graphene wrinkles more efficiently compared to an O_2 plasma.

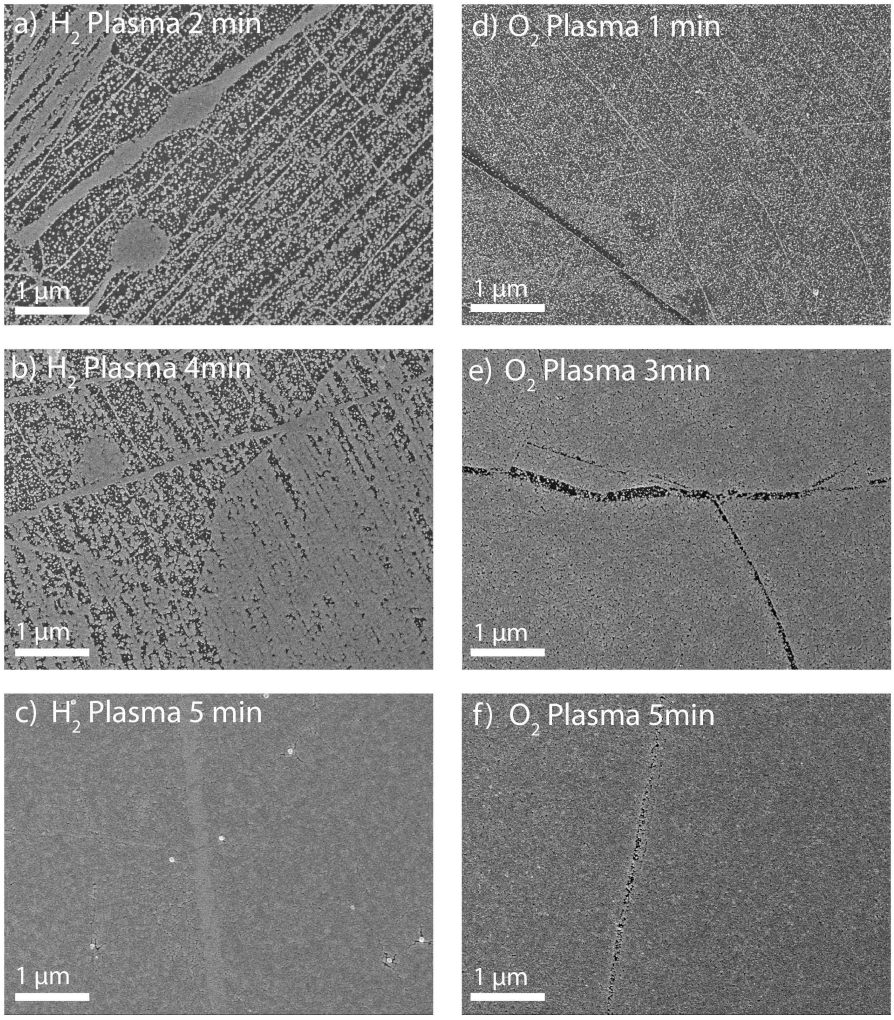


Figure 5.5: SEM image of graphene exposed to different plasma treatments followed by 500 cycles of Pt ALD: a) H_2 plasma 2 min, b) H_2 Plasma 4 min c) H_2 Plasma 5 min, d) O_2 plasma 1 min, e) O_2 plasma 3 min and f) O_2 plasma 5 min. The Pt surface coverage increases as a function of the plasma exposure time for both H_2 and O_2 plasma treatments. d), e), and f) adapted from Karasulu *et al.* [19].

5.3.3 Pt ALD graphene device fabrication and the influence of functionalization on the contact resistance

Circular transfer length method (CTLM) structures were made to investigate whether the combination of plasma treatment and Pt ALD provides a good quality metal-graphene contact. The CTLM structures on graphene were created using area-selective ALD (AS-ALD) of platinum, using photosensitive polyimide [35]. The polyimide can be patterned using photolithography and acts as a blocking layer, preventing the adsorption of the $MeCpPtMe_3$ precursor in places where polyimide is present. This makes it possible to selectively deposit Pt in the opened up regions. Compared to other polymers that can be used for the blocking of ALD growth polyimide has a relatively high temperature stability (> 350 °C). This prevents reflowing of the resist during the Pt ALD process (performed at 300 °C), allowing for better pattern definition and improved uniformity of the Pt features [35].

Figure 5.6a,c shows graphene patterned with CTLM structures. The diameter of the rings ranges between 5 and 48 μm. To initialize ALD growth on graphene, the graphene was exposed to varying H_2 plasma treatments ranging from 5 to 20 min and O_2 plasma treatments ranging from 5 to 15 min. The plasma times chosen were extended compared to those shown in Figure 5.2. This is because the additional polyimide lithography step introduces additional polymer residues on the graphene, requiring a longer plasma exposure to obtain a similar degree of functionalization when compared to the Raman spectra in Figure 5.2. Without the additional polyimide lithography step, all graphene was removed after 10 min of H_2 plasma exposure. After the additional polyimide lithography step, a plasma exposure of 20 min is required to fully etch the graphene. This indicates that the plasma needs to etch through the polyimide residue before the graphene is functionalized.

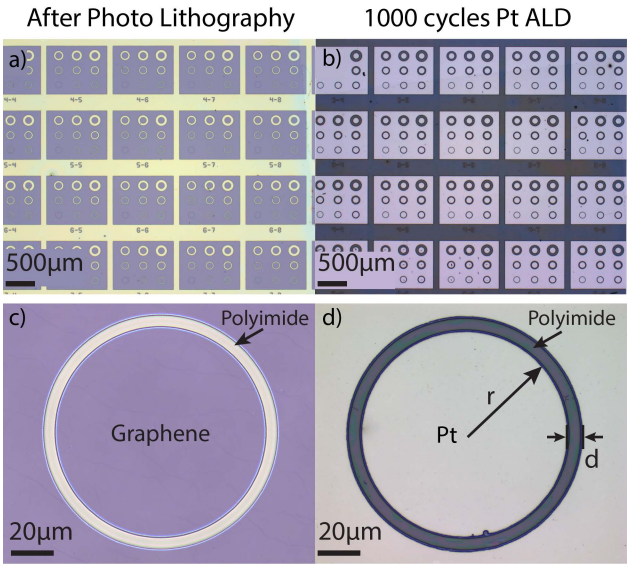


Figure 5.6: Optical micrograph of a), c) graphene patterned with CTLM structures by photolithography using photosensitive polyimide as the resist and the same structures b), d) after 5 min of H_2 plasma functionalization and 1000 cycles of Pt ALD. No Pt growth occurs on the polyimide allowing for the AS-ALD of Pt. The parameters of Eq. 5.1 are indicated in d) as well.

As an example, the CTLM structures after 5 min H_2 plasma functionalization and 1000 cycles of Pt ALD are shown in Figure 5.6b,d. No Pt growth is observed on the polyimide, while on the graphene a closed Pt layer of approximately 36 ± 3 nm thick is obtained. The thicknesses obtained were comparable for all different plasma treatment times indicating that the differences in nucleation delay due to the extended plasma treatment times are small. Furthermore, it should be noted that despite the long plasma treatment times, the Pt ALD process remains selective. This shows that a H_2 and O_2 plasma are unable to etch or modify the polyimide surface to make it susceptible for ALD, as was previously concluded from spectroscopic ellipsometry and XPS data [35]. Less than a monolayer of Pt is deposited on the polyimide during the Pt ALD process.

As demonstrated in our earlier work, the catalytic activity of these trace amounts of Pt present on the polyimide after ALD make it possible to remove the polyimide by a H_2 plasma exposure [35]. However, to prevent possible damage to the graphene channel during the polyimide removal, the polyimide was not etched here [65,66].

To determine the contact resistance, the resistance of the CTLM structures was measured in a vacuum probe station using a two-point probe configuration. The samples were annealed at 200 °C for 12 h before measuring to remove any adsorbed species

from the ambient and to improve device reproducibility. The voltage was varied from -10 to 10 mV while measuring the current. The measurements were performed at room temperature under vacuum (< 10^{-4} mbar). By plotting the resistance determined from the two probe measurements as a function of the gap size d (channel length) the contact resistance can be determined from [67–69]:

$$R_{\mathrm{tot}} = \frac{1}{2\pi}\left[R_{\mathrm{s}}L_{\mathrm{t}}\left(\frac{1}{r}+\frac{1}{r+d}\right)+R_{\mathrm{ss}}\ln\frac{r+d}{r}\right] \tag{5.1}$$

where R_{s} is the sheet resistance of the graphene under the Pt contacts, L_{t} is the transfer length, R_{ss} is the sheet resistance of the graphene in the channel, and r the inner radius of the circular contact. The contact resistance R_{c} is defined as:

$$R_{\mathrm{c}} = R_{\mathrm{s}}L_{\mathrm{t}} \tag{5.2}$$

For $r >> d$, Eq. 5.1 can be simplified to:

$$R_{\mathrm{tot}} = \frac{1}{2\pi r}(R_{\mathrm{ss}}d + 2R_{\mathrm{c}})C \tag{5.3}$$

where C is a correction factor [70]:

$$C = \frac{r}{d}\ln\left(\frac{r+d}{r}\right) \tag{5.4}$$

The correction factor takes into account the difference between the CTLM and TLM methods and makes it possible to use a linear fit to extract the contact resistance. In literature it is often assumed that the sheet resistance of the graphene in the channel R_{ss} is equal to the sheet resistance of the graphene under the contacts R_{s}, which makes it possible to determine the transfer length and specific contact resistivity ρ_{c} ($R_{\mathrm{s}}L_{\mathrm{t}}^2$) [69]. However, because a plasma treatment is used to initialize the Pt ALD growth, the sheet resistance of the graphene under the contacts is considerably higher compared to the graphene channel. Therefore this assumption does not hold for the work presented here.

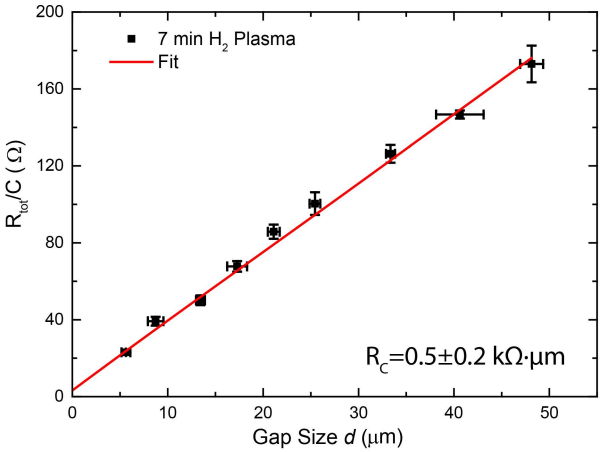


Figure 5.7: Two point probe resistance measurement of Pt ALD-graphene contacts, Pt ALD growth was initiated by a 7 min H_2 plasma treatment. The resistance is averaged over six devices and divided by a correction factor *C* which takes into account the increase in the contact area with increasing ring size. Fitting Eq. 5.3 the contact resistance is determined to be 0.5 ± 0.2 kΩ.

Figure 5.7 shows an example of a fit of Eq. 3 to data obtained from Pt-graphene contacts created using a 7 min H2 plasma exposure of graphene followed by Pt ALD. The resistance for each channel length was determined from an average of at least six different devices. From the intercept with the vertical axis the contact resistance can be determined to be 0.5 ± 0.2 kΩ·μm, while the sheet resistance of the channel can be determined from the slope (1.01 ± 0.02 kΩ/□). The contact resistances and sheet resistances for all other plasma treated samples was obtained using the same method as for the sample described above. For reference purposes, also a sample was fabricated using EBL and e-beam evaporated Pt (PVD Reference devices). In this case 35 nm Pt using a 1 nm Ti adhesion layer served as the metal-graphene contact. Polyimide is not used to pattern the reference devices, because e-beam evaporation also results in the deposition of Pt on polyimide, requiring a lift-off step to prevent shorting the channel. The lift-off of polyimide however, is not straightforward. Therefore PMMA was used for the patterning of the reference devices instead. One reference sample was exposed to a 5 min H2 plasma before Ti/Pt evaporation to investigate the effect of the H2 plasma treatment on the contact resistance, and compare the difference between ALD and evaporated Pt-graphene contacts. An overview of the contact resistances and sheet resistances, determined as a function of the plasma treatment time, is displayed in Table 5.1. The development of the contact resistance as a function of the plasma treatment time is shown in Figure 5.8.

Table 5.1: The sheet resistance of the graphene channel (R_{ss}) and contact resistance (R_c) determined from the CTLM measurements of the Pt-graphene contacts. The different H_2 and O_2 plasma exposure times indicate the duration of the plasma used to initiate the Pt ALD growth. For comparison also the contact resistance of the PVD reference devices and several literature values are also indicated.

Plasma treatment time	R_{ss} (kΩ/□)	R_c (kΩ·µm)
PVD Reference	1.33 ± 0.03	11.5 ± 0.4
PVD H_2 Plasma Treatment		
5 min	1.18 ± 0.05	3.7 ± 0.5
PVD O_2 Plasma Treatment		
Au/Graphene [33]	0.148	5.56
Pd/Cr/Graphene [12]	-	1.10
ALD H_2 Plasma Treatment		
5 min	0.83 ± 0.04	0.9 ± 0.2
7 min	1.00 ± 0.01	0.5 ± 0.2
10 min	0.76 ± 0.03	1.2 ± 0.2
15 min	1.10 ± 0.02	0.5 ± 0.1
20 min	1.11 ± 0.03	0.4 ± 0.2
ALD O_2 Plasma Treatment		
5 min	0.70 ± 0.02	4.2 ± 0.2
10 min	0.96 ± 0.03	1.2 ± 0.1
15 min	1.01 ± 0.03	1.3 ± 0.2

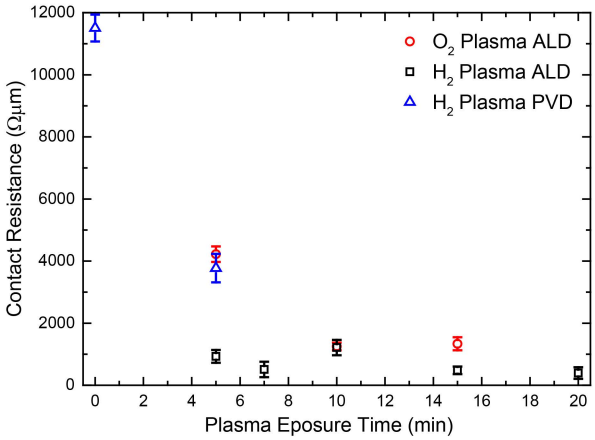


Figure 5.8: Contact resistance determined from the CTLM measurements as a function of the H_2 or O_2 plasma treatment time. A comparison is made between the devices synthesized by AS-ALD and plasma functionalization and EBL and e-beam evaporation (PVD).

Figure 5.8 shows that the contact resistance can be decreased when metallization is preceded by an H2 or O2 plasma treatment on graphene, irrespective of whether ALD or e-beam evaporation is used for the deposition of Pt. The PVD devices that received a 5 min H2 plasma treatment have a contact resistance about a factor of three lower compared to the reference PVD devices which received no plasma treatment (11.5 ± 0.4 kΩ·µm vs. 3.7 ± 0.5 kΩ·µm). The improvement of the contact resistance is most likely due to the better Pt-graphene interaction as a result of the plasma treatment. The surface groups created by the plasma treatment enhance the transport of charge carriers from the metal to the graphene through an increase of the number of chemical bonds between the metal and the graphene [33]. Compared to the PVD deposited contacts, the ALD contacts show an even larger improvement. After a 5 min H2 plasma the contact resistance is reduced to 0.9 ± 0.2 kΩ·µm. The additional improvement observed for the ALD created contacts could be due to the improved wetting interaction of the deposited Pt with the underlying graphene or an improved Pt morphology due to the use of ALD [5,18]. Additionally, as opposed to Pt PVD, for the creation of the Pt ALD contacts a Ti adhesion layer is no longer required. This could also have a positive effect on the metal graphene interaction, due to the different work function and interaction strength of Ti compared to Pt [8,9].

The lowest contact resistance (0.4 ± 0.2 kΩ·µm) is obtained after a H_2 plasma treatment of 20 min, where almost no graphene remains under the contacts. For an O_2 plasma treatment the contact resistance also decreases as a function of the plasma treatment time from 4.2 ± 0.2 kΩ·µm for a 5 min pretreatment to 1.3 ± 0.2 kΩ·µm after 15 min. The improvement however, is less than observed for a H_2 plasma treatment. The improved performance of the H_2 plasma functionalized Pt-Graphene contacts compared to the O_2 functionalized Pt-Graphene contacts could be related to the different surface groups being present at the interface of the Pt-Graphene contacts, as observed by XPS (C-H vs C-O). Furthermore, as revealed by the Raman measurements, in Figure 5.3b, the O_2 plasma treatment causes amorphization of the graphene. The amorphization of graphene with increasing oxygen-containing functionalities has previously been related to the buckling of the graphene basal plane and oxygen-doping of the graphene lattice [19,71]. The graphene that remains under the contacts after a O_2 plasma treatment is therefore of lower quality compared to the graphene after a H_2 plasma treatment. Irrespective of the plasma treatment however, the lowest contact resistance is obtained for the maximum plasma treatment time. A possible explanation could be the formation of an edge-like contact, where most of the graphene under the contacts is removed and only the edge of the channel is contacted. This is schematically illustrated in Figure 5.9.

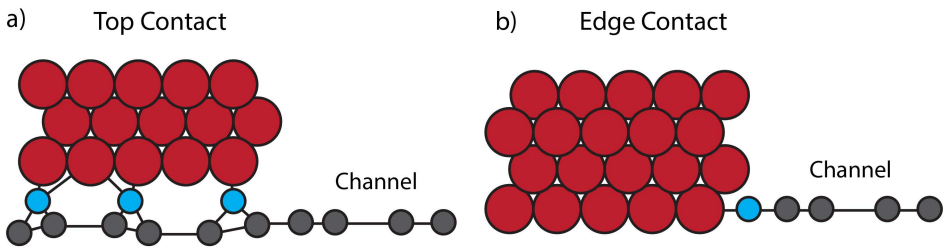


Figure 5.9: Schematic representation of the contact formation. a) For short plasma treatment times the graphene is likely still present under the contact and a top contact configuration is obtained. b) Longer plasma treatment times likely remove most of the graphene under the metal contact resulting in an edge type contact. The graphene (grey) is contacted to the platinum (red) via functional groups created by the plasma treatment (blue).

To get a better understanding of the performance of our Pt-ALD graphene contacts, compared to the more standard evaporated metal-graphene contacts, we compared our work with references [12,32,33] which used similar device structures in combination with plasma treatments. Yue *et al.* fabricated Cr/Pd-graphene contacts, with similar device dimensions as the ones reported here. The graphene under the contacts was exposed to an O_2 plasma treatment before contact formation [12]. Short plasma treatment times resulted in the formation of a functionalized top contact that showed a small improvement of the contact resistance. The use of a longer plasma treatment time on the other hand, resulted in the formation of an edge-contact, where only the edge of the contact metal was in contact with the graphene. The edge-contact gave the lowest contact resistance (1.1 kΩ·µm). This low contact resistance was attributed to the shorter binding distances, and improved orbital overlap of the electrons compared to the metal-graphene top contacts [5,10,12]. The contact resistance values reported by Yue *et al*. are comparable to the Pt-ALD contacts prepared by an O_2 plasma as reported here (1.2 kΩ·µm). Although a direct comparison is hampered by the different contact metal being used, this indicates that ALD contacts of similar quality compared to evaporated contacts can be created using an O_2 plasma treatment. Our Pt-ALD contacts fabricated using H_2 plasma functionalization showed a lower contact resistance than reported (0.4 kΩ·µm) indicating that H_2 plasma functionalization might be a viable approach to further reduce the contact resistance of evaporated contacts as well.

The decreasing contact resistance as a function of the O_2 plasma treatment time, observed in Figure 5.8, is opposite to the trend observed by Foley *et al*. who used O_2 plasma functionalization in combination with evaporation to synthesize Au-graphene contacts, obtaining a minimum contact resistance of 5.4 kΩ·µm [33]. Since both Au and

Pt interact only weakly with graphene, (both Au and Pt are expected to benefit from functional groups and defects present on the graphene surface) [34], a decrease of the contact resistance as a function of the O_2 plasma treatment time is expected for both metals. The observed increase in contact resistance as a function of the O_2 plasma treatment time for Au-graphene contacts could be explained by the fact that the Au-graphene contacts were not annealed after fabrication. Smith *et al*. have shown that annealing at 350 °C is required to activate the functionalization and improve the contact resistance for evaporated metal-graphene contacts [72]. For Pt ALD fabricated contacts an anneal is most likely not required since the temperature during the ALD process is 300 °C, which is likely sufficient to achieve an optimal metal-graphene contact. To confirm this, the sample functionalized with 7 min H_2 plasma and 5 min O_2 plasma were annealed at 400 °C in a 5% Ar/H_2 mixture for 2 h. This did not change the contact resistance of the H_2 plasma treated sample (0.2 ± 0.5 kΩ·µm vs. 0.5 ± 0.2 kΩ·µm) and slightly increased it for the O_2 plasma (5.4 ± 0.7 kΩ·µm vs. 4.2 ± 0.2 kΩ·µm). The increase in contact resistance could be due to the dewetting of Pt at 400 °C, which would also explain the larger measurement error after annealing.

5.3.4 Contact Resistance dependency on the functionalization of graphene studied by *ab into* calculations

To better understand the effect of the H_2 and O_2 plasma functionalization on the contact resistance *ab-initio* DFT calculations were performed. The orbital-projected density of states (DOS) and band diagrams along the high-symmetry **K**-points (*MΓKM* path) were computed using the model systems as depicted in Figure 5.10 (insets). The resulting partial and total DOS and band diagrams of the free-standing and Pt-(top)-contacted pristine graphene (PG), graphene oxide (GO) and hydrogenated graphene (SSHG) are shown in Figure 5.10 and Figure 5.11. Complete DOS and band structure plots of these systems, which cover different energy regions and/or also include the Pt contributions can be found elsewhere [56] (these are excluded here for clarity, as the Pt-d orbital contributions overshadow others).

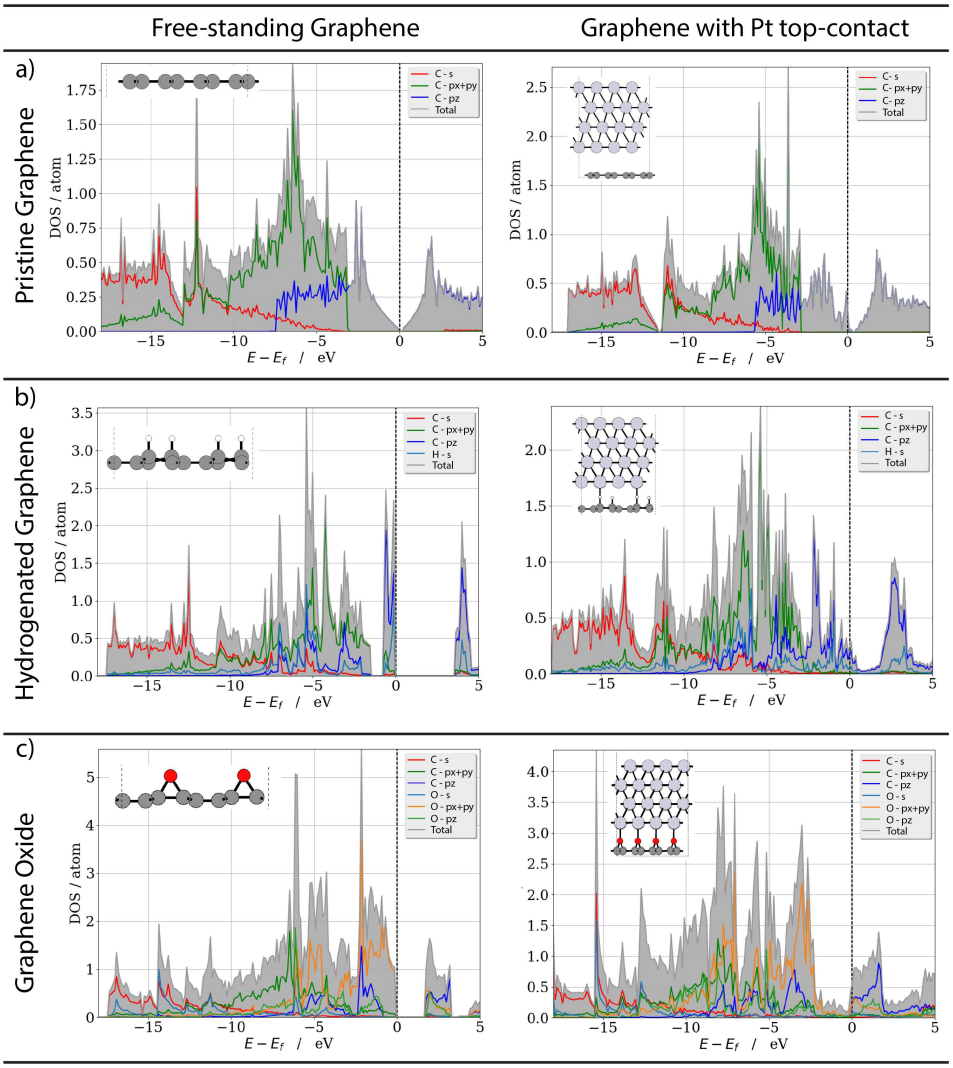


Figure 5.10: DFT/vdW-DF2 level orbital-projected density of states (DOS) per atom of free-standing and Pt(111)-contacted a) pristine graphene (PG), b) graphene oxide (GO) and c) hydrogenated graphene (SSHG). The model systems used are depicted in the inset of each graph (Pt: light gray, C: dark gray, H: white, O: red). The Fermi level of each system is set to zero (dashed vertical line). Each of the DOS curves is averaged over all atoms contributing to the individual DOS plot (e.g. C, O, and/or H, see legends for actual compositions). The gray shaded areas show the sum of contributions from the individual atomic orbital types.

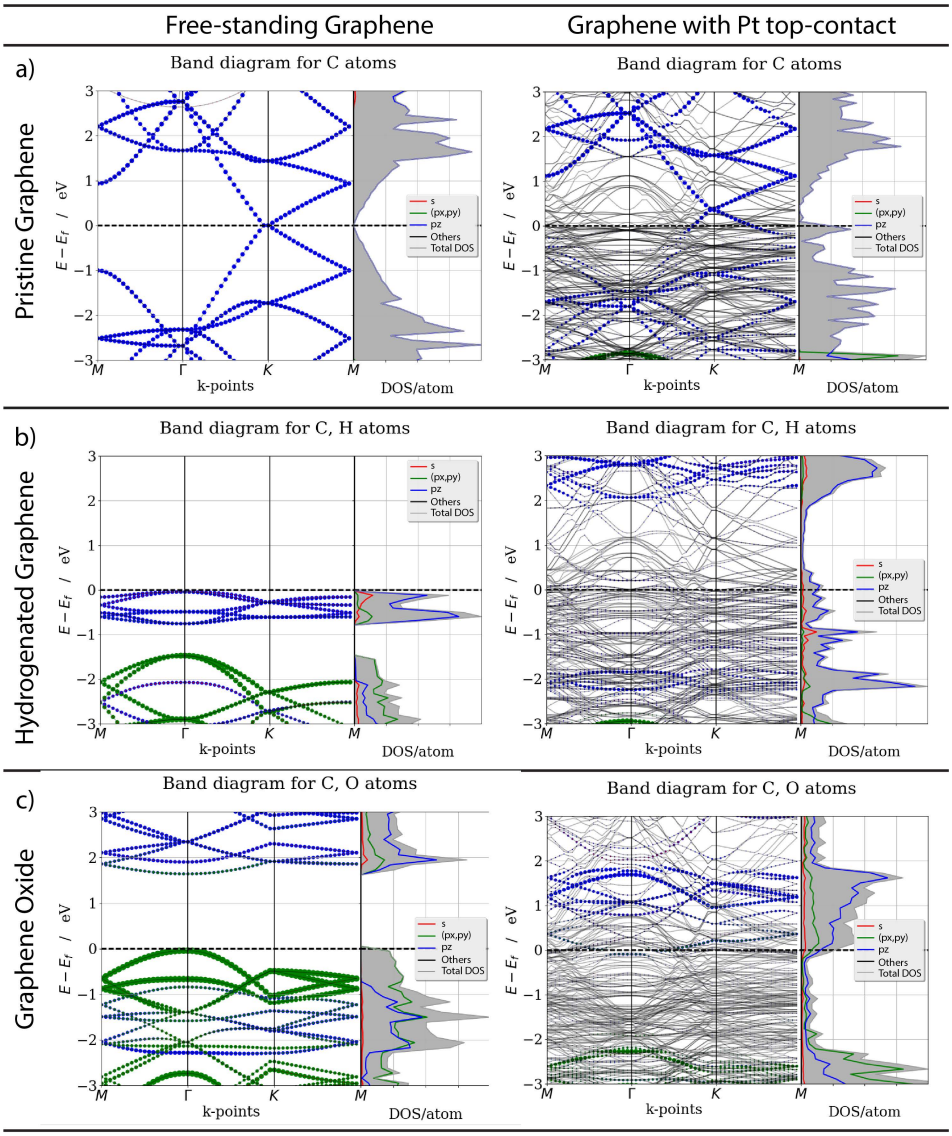


Figure 5.11: DFT/vdW-DF2 level orbital-projected band structures along the *M-Γ-K-M* high-symmetry path of (left) free-standing and (right) Pt(111)-top-contacted a) pristine graphene (PG), b) graphene oxide (GO) and c) hydrogenated graphene (SSHG). The corresponding partial DOS per atom are also plotted. The energy levels (eV) are shifted by the Fermi energy (E_f, dashed horizontal lines) and only energies within 3 eV of E_f are depicted. The DOS and band diagrams are LM-decomposed to show individual orbital contributions from selected atom types. Specific orbital contributions are depicted by colored beads (s: red; p_{xy}: green; p_z: blue; others: gray). The size of the beads indicates the weight of corresponding Bloch eigenstate of a given orbital. For the Pt-

contacted graphene samples, contributions from Pt atoms are given by pale solid lines (for clarity) and labelled as 'others'. The model systems used for band diagrams can be found in the insets of Figure 5.10.

The DOS and band structure plots of PG (Figure 5.10a and Figure 5.11a) show that the calculations reproduce the signature electronic features of graphene: specifically, the zero band-gap (i.e. vanishing DOS at the Fermi level, E_f) and the metallic character due to the topological singularities at the *K*-point (i.e. the Dirac cone of the touching valence and conductance bands). Moreover, the Fermi region ($E_f \pm 3$ eV) is dominated by the carbon-p_z contributions, a result of the extended π-conjugation that contributes to the extraordinary in-plane electronic conductivity of graphene.

The placement of a Pt-contact on top of pristine graphene (Figure 5.11a) does not distort the properties of the PG. The zero-bandgap is maintained as well as the conical shape of the carbon bands around the K-point, following from the weak (physical) and long-range coupling between Pt and graphene [7,73]. The presence of the Pt contact, however, does result in a shift of the Dirac point above E_f by about 0.30 eV. This is in good agreement with previous DFT and micro-ARPES studies [7,73]. The upshift of the Dirac point can be attributed to the p-type doping of graphene, where approximately 0.07*e* (based on Bader charges) are transferred from the graphene to the Pt contact. The findings highlight that, despite the good in-plane conductivity of PG, the conductivity between the Pt and PG is limited due to the weak Pt-graphene interaction and large coupling length. This is in agreement with the large contact resistance obtained for the evaporated Pt PVD reference sample (no H_2 treatment), shown in Figure 5.8.

The functionalization of graphene by hydrogen and oxygen (Figure 5.10b,c) significantly alters the electronic structure of graphene, indicated by the opening of a bandgap for both adsorbate types. At the surface coverage ratio used in the models (C:[O/H]=4:1) a direct bandgap is induced for both SHHG and GO. The band gap is located at the Γ-point, amounting to 3.61 and 1.69 eV for free-standing hydrogenated and oxygenated graphene, respectively. The predicted bandgaps for SSGH and GO are in good agreement with previous reports [51,52,74]. A comparison of the DOS plots of SSHG and GO with PG also reveals notable changes in the overall orbital composition and structure. In the case of isolated GO, the oxygen p_{xy} orbitals dominate the energy levels encompassing the Fermi level ($E_f \pm 3$ eV), suppressing the carbon p_{xy} and -more importantly- the carbon p_z contributions. In contrast to GO, the carbon p_z character is more pronounced in electronic structure of SSHG, like its PG counterpart. Yet, unlike PG, the carbon p_{xy} orbitals also play a key role in the DOS of SSHG in this energy regime, likely due to the sp^3 hybridization of carbon atoms. Similarly, the band structure

of SSHG in the Fermi region (Figure 11b) shows that the valence and conduction bands have more C p_z character than C p_{xy}. The top of the valence band of GO on the other hand is mainly of p_{xy} character, contributed by both carbon and oxygen atoms. The mitigated C p_z character (and resulting distorted π-conjugation) predicted in the Fermi region of isolated GO and SSHG is the likely reason for their reduced (in-plane) charge carrier mobilities compared to PG, a common feature for functionalized graphenes [31,33].

Top/surface contacting of functionalized graphene (GO and SSHG) with Pt gives rise to a more prominent change in the electronic structure as compared to contacting PG (Figure 5.10). The large bandgaps of the free-standing GO and SSHG both vanish when contacted with Pt, while at the same time the band features are distorted (Figure 5.11From the DOS and band structures, one can determine that n-type doping is induced (i.e. E_f is upshifted) for both GO and SSHG upon contacting with Pt. This in contrast to the p-type doping observed for PG. Even though the Pt-d orbitals now dominate the Fermi region (Figure 5.11), the overall composition of the main atomic orbital contributions from the graphene C and O/H atoms remains qualitatively unaltered, when compared to their isolated graphene counterparts. In detail, GO has primarily a p_{xy} character (contributed mainly by O-p_{xy} orbitals and by C- p_{xy} orbitals) in the valence band, whereas the C and O p_z orbitals dominate the conduction band. Besides, the C-Pt interactions are chemically shielded by the presence of oxygen. In contrast, SSHG displays an even-stronger p_z character (from the carbon atoms) when contacted with Pt, whereas its p_{xy} states are suppressed. The H-s orbitals have only a minor contribution to the DOS of SSHG, and a reduced shielding of the C-Pt interactions is expected, compared to GO.

The substantial change in electronic properties of functionalized graphene points at the stronger bonded (covalent/ionic) interactions of graphene with the Pt through the functional groups, unlike the PG case where the weaker non-bonded (vdW) interactions govern the transmission efficiencies. DFT/LDA minimum structures reveal that bonded interactions enable shorter Pt-graphene coupling lengths for GO (with minimum O-Pt distances of ca. 2.30 Å) and SSHG (H-Pt: 1.86 Å) as compared to PG (C-Pt: ca. 3.33 Å). The less compact coupling of Pt-GO than Pt-SSHG can be attributed to the larger vdW radius of oxygen. Besides, Bader analysis of partial charges suggests that Pt contact donates a charge of approximately 0.50*e* to GO, whereas only a 0.17*e* transfer is expected for SSHG. Larger charge transfer for GO hints at a stronger interaction of GO with Pt than SSHG and PG with Pt. This is further supported by the predicted GO/Pt binding energy of 104 meV/atom, whereas that of SSHG is significantly weaker

(ΔE_b=77 meV/atom), but still stronger than that of PG (ΔE_b=35 meV/atom). These findings suggest that the Pt wetting efficiency can be ordered as follows: GO > SSHG > PG. This is in line with the quicker Pt film closure observed in Figure 5.5 for the O_2 plasma treated graphene compared to the H_2-treated and pristine graphene, respectively.

To analyze the effect of contact type (top/surface vs. edge/side, see Figure 5.9) on the nature of Pt-graphene interaction, two models comprising PG and SSHG edge-contacted to Pt(111) were investigated (Insets Figure 5.12). GO was not analyzed because a prolonged O_2 plasma treatment (unlike H_2) renders the graphene amorphous before an edge-contact could be formed. The resulting partial DOS plots (Figure 5.12) reveal the major changes in charge carrier transport means for both PG and SSHG depending on the junction type. As already discussed, in a conventional top/surface contact the coupling of Pt and pristine graphene is achieved through C-p_z and Pt-d orbitals and the coupling length is large due to stable π-bonds. Likewise, out-of-plane C-p_z Pt-d interactions are still the key factor for carrier transmittance in a SSHG-Pt top contact, with additional pathways introduced by the H-s Pt-s interactions. In contrast, for the high transmission efficiencies in edge-contacted junctions, the pπ and pσ orbitals play an equivalently important role besides the shorter coupling lengths [75]. From Figure 5.12 it becomes evident that the C-p_{xy} orbitals have the highest DOS contributions near E_f for both edge-contacted PG and SSHG. These orbitals couple well with the Pt-p_{xy} (alongside Pt-d) orbitals to enable in-plane conduction paths. Additionally, C-s and Pt-s interactions arise due to the dangling bonds at the graphene edges. The H-s orbitals in SSHG augment the pσ interactions compared to PG, which could further increase the cohesive coupling between Pt-graphene and decrease the contact resistance.

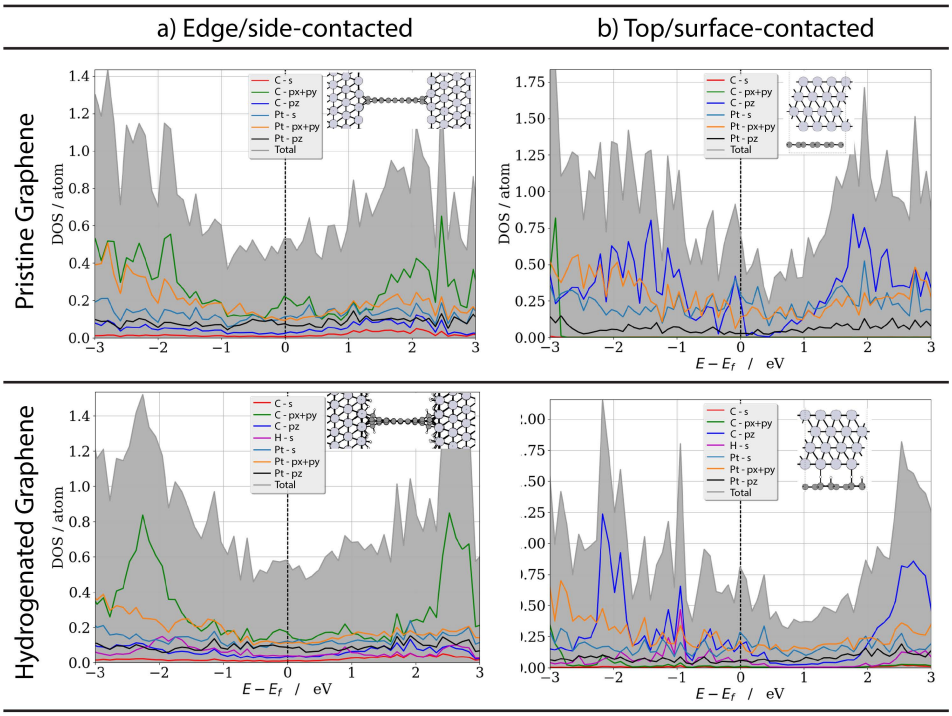


Figure 5.12: GGA/vdW-DF2 level atom-projected DOS of PG and SSHG that are (a) edge- or (b) top-contacted to Pt metal. Insets show the models used for the calculations. Contributions by atomic orbitals of C, H and Pt are given by diverse colors. Pt-d orbital contributions are not shown for clarity. See Figure 8 caption for other details.

The observations made above, suggest that the Fermi region (valence and conduction bands) of SSHG is dominated by C-p_z orbitals that are well aligned with Pt-d orbitals. Therefore, the in-plane conduction pathways of charge carriers are still accessible for SSHG through extended π-conjugation, even when top-contacted with Pt. In contrast, GO has a stronger interaction with the Pt contact mainly through the Pt-d and O-p_{xy} orbitals and to a smaller extent the p_z, which activates the out-of-plane conduction modes rather than in-plane ones. This enhances the major carrier conduction along the dipole formed across the Pt-GO junction, but limits the conduction along the channel. Since a high-quality metal-graphene contact requires both a good in-plane and out-of-plane conductivity SSHG would be a better choice for a top-contact configuration as it provides a good balance between the two conduction modes. The improved contact resistances observed for H_2 plasma treated graphene compared to O_2 plasma treated graphene (Figure 5.8) agree well with this observation.

In case of an edge-type contact configuration the contact-channel transmission/conduction pathways are governed by π-bond (C-p_{xy} with Pt-p_{xy} and Pt-d orbitals) as well as σ-bond (C-s with Pt-s) interactions. Besides, a good conduction along the graphene channel is provided by the intact π-conjugation system (formed by C-p_z orbitals). The enhanced interactions at the edge-like Pt/graphene interface, compared to a top-contact increase the transmission efficiencies and decreases the contact resistances (in line with previous reports) [12,75]. Besides, the SSHG is predicted to provide even stronger contact-channel interactions (thus lower contact resistances) than PG, due to the involvement of additional H-s and Pt-s orbital interactions. This is in agreement with the experimental observation in Figure 5.8 that the lowest contact resistance is obtained when almost all the graphene under the Pt contacts is removed and an edge-like contact is formed after a prolonged plasma exposure.

5.4 Conclusions

To conclude, Pt-graphene contacts were created by a combination of plasma functionalization, and ALD. The O_2 and H_2 plasma functionalization of graphene served two purposes. Firstly, the formation of functional groups on the graphene during plasma exposure created adsorption sites for the Pt ALD precursor molecules, allowing for uniform ALD of Pt on graphene. Additionally, the created functional groups improved the Pt-graphene interaction, which reduced the contact resistance between the Pt and the graphene.

The devices created using a H_2 plasma treatment performed considerably better (3x lower contact resistance) than the ones created using an O_2 plasma treatment. This points in the direction that C-H groups created by the H_2 plasma contribute to more efficient charge transfer pathways than the C-O groups created by the O_2 plasma. The improved performance of the H_2 plasma functionalized devices was expounded on by the DFT calculations, which indicated that the presence of hydrogen containing functionalities on graphene leave the dominating C-p_z character (π-conjugation) of graphene largely intact. Compared to pristine graphene the out-of-plane charge transfer improves through the additional Pt-H interactions alongside shorter coupling lengths. This brings about a good balance between the in-plane and out-of-plane conductivity for H_2 plasma treated graphene. The O_2 plasma treatment also improved the out-of-plane interactions due to additional Pt-O orbital interactions. However, the in-plane conduction along the channel is interrupted by the oxygen atoms, whose orbitals

dominate the valence and conduction bands rather than those of carbon, leading to a good out-of-plane conduction but severely degrades the in-plane conduction. Additionally, the amorphization of graphene as a result of the O_2 plasma treatment could play an unfavorable role.

The best contact resistance (0.4 ± 0.2 k$\Omega \cdot \mu$m and 1.2 ± 0.1 k$\Omega \cdot \mu$m for the H_2 and O_2 plasma treatment, respectively) was obtained when almost all graphene under the contacts was removed and likely an edge-contact was created. Compared to reference devices created by EBL, evaporation and plasma functionalization, the ALD created Pt-graphene contacts resulted in a lower contact resistance. The enhanced performance of the ALD created contacts was attributed to the absence of a Ti-adhesion layer, as was required for the reference devices.

The obtained results show that plasma functionalization in combination with ALD is a promising method for the creation of high quality metal graphene contacts. The use of H_2 plasma treatments to reduce the contact resistance are of particular interest, as they can be readily integrated in contact fabrication processes that use other contact metals and/or contact deposition techniques.

Acknowledgements

The authors would like to thank C.O. van Bommel, C.A.A. van Helvoirt, J.J.L.M. Meulendijks & J.J.A. Zeebregts for technical assistance. Dr. P.V.C. Medeiros and dr. J.R. Nelson are acknowledged for their fruitful discussions on the electronic structure calculations. This work is part of the research program of the Foundation for Fundamental Research on Matter (FOM), which is part of the Netherlands Organization for Scientific Research (NWO).

References

1. Schwierz, F. (2010) Graphene transistors. *Nat. Nanotechnol.*, **5** (7), 487–496.

2. Wu, Y., Jenkins, K.A., Valdes-Garcia, A., et al. (2012) State-of-the-Art Graphene High-Frequency Electronics. *Nano Lett.*, **12** (6), 3062–3067.

3. Xia, F., Mueller, T., Lin, Y., et al. (2009) Ultrafast graphene photodetector. *Nat. Nanotechnol.*, **4** (12), 839–843.

4. Nagashio, K., Nishimura, T., Kita, K., and Toriumi, A. (2009) Metal/graphene contact as a performance Killer of ultra-high mobility graphene analysis of intrinsic mobility and contact resistance. *2009 IEEE Int. Electron Devices Meet.*, 1–4.

5. Xia, F., Perebeinos, V., Lin, Y., et al. (2011) The origins and limits of metal–graphene junction resistance. *Nat. Nanotechnol.*, **6** (3), 179–184.

6. Moriyama, T., Nagashio, K., Nishimura, T., and Toriumi, A. (2013) Carrier density modulation in graphene underneath Ni electrode. *J. Appl. Phys.*, **114** (2), 24503.

7. Giovannetti, G., Khomyakov, P.A., Brocks, G., et al. (2008) Doping Graphene with Metal Contacts. *Phys. Rev. Lett.*, **101** (2), 26803.

8. Khomyakov, P.A., Giovannetti, G., Rusu, P.C., et al. (2009) First-principles study of the interaction and charge transfer between graphene and metals. *Phys. Rev. B*, **79** (19), 195425.

9. Chaves, F.A., Jiménez, D., Cummings, A.W., and Roche, S. (2014) Physical model of the contact resistivity of metal-graphene junctions. *J. Appl. Phys.*, **115** (16), 164513.

10. Wang, L., Meric, I., Huang, P.Y., et al. (2013) One-Dimensional Electrical Contact to a Two-Dimensional Material. *Science*, **342** (6158), 614–617.

11. Chu, T., and Chen, Z. (2014) Understanding the Electrical Impact of Edge Contacts in Few-Layer Graphene. *ACS Nano*, **8** (4), 3584–3589.

12. Yue, D.W., Ra, C.H., Liu, X.C., et al. (2015) Edge contacts of graphene formed by using a controlled plasma treatment. *Nanoscale*, **7** (2), 825–831.

13. Ifuku, R., Nagashio, K., Nishimura, T., and Toriumi, A. (2013) The density of states of graphene underneath a metal electrode and its correlation with the contact resistivity. *Appl. Phys. Lett.*, **103** (3), 33514.

14. Nath, A., Koehler, A.D., Jernigan, G.G., et al. (2014) Achieving clean epitaxial graphene surfaces suitable for device applications by improved lithographic process. *Appl. Phys. Lett.*, **104** (22), 224102.

15. Chavarin, C.A., Sagade, A.A., Neumaier, D., et al. (2016) On the origin of contact resistances in graphene devices fabricated by optical lithography. *Appl. Phys. A*, **122** (2), 58.

16. Song, S.M., and Cho, B.J. (2013) Contact resistance in graphene channel transistors. *Carbon Lett.*, **14** (3), 162–170.

17. Thissen, N.F.W., Vervuurt, R.H.J., Mackus, A.J.M., et al. (2017) Graphene devices with bottom-up contacts by area-selective atomic layer deposition. *2D Mater.*, **4** (2), 25046.

18. Mackus, A.J.M., Thissen, N.F.W., Mulders, J.J.L., et al. (2017) Resist-free fabricated carbon nanotube field-effect transistors with high-quality atomic-layer-deposited platinum contacts. *Appl. Phys. Lett.*, **110** (1), 13101.

19. Karasulu, B., Vervuurt, R.H.J., Kessels, W.M.M., and Bol, A.A. (2016) Continuous and ultrathin platinum films on graphene using atomic layer deposition: a combined computational and experimental study. *Nanoscale*, **8** (47), 19829–19845.

20. Kim, K., Lee, H.-B.-R., Johnson, R.W., et al. (2014) Selective metal deposition at graphene line defects by atomic layer deposition. *Nat. Commun.*, **5**, 4781.

21. Wang, X., Tabakman, S.M., and Dai, H. (2008) Atomic Layer Deposition of Metal Oxides on Pristine and Functionalized Graphene. *J. Am. Chem. Soc.*, **130** (26), 8152–8153.

22. Park, K.S., Kim, S., Kim, H., et al. (2015) Wafer-scale single-domain-like graphene by defect-selective atomic layer deposition of hexagonal ZnO. *Nanoscale*, **7** (42), 17702–17709.

23. Garces, N.Y., Wheeler, V.D., and Gaskill, D.K. (2012) Graphene functionalization and seeding for dielectric deposition and device integration. *J. Vac. Sci. Technol. B Microelectron. Nanom. Struct.*, **30** (3), 30801.

24. Marichy, C., and Pinna, N. (2013) Carbon-nanostructures coated/decorated by atomic layer deposition: Growth and applications. *Coord. Chem. Rev.*, **257** (23–24), 3232–3253.

25. Kim, J., and Jandhyala, S. (2013) Atomic layer deposition of dielectrics for carbon-based electronics. *Thin Solid Films*, **546**, 85–93.

26. Vervuurt, R.H.J., Kessels, W.M.M.E., and Bol, A.A. (2017) Atomic Layer Deposition for Graphene Device Integration. *Adv. Mater. Interfaces*, **1700232**, 1700232.

27. Lee, B., Mordi, G., Kim, M.J., et al. (2010) Characteristics of high-k Al2O3 dielectric using ozone-based atomic layer deposition for dual-gated graphene devices. *Appl. Phys. Lett.*, **97** (4), 43107.

28. Jandhyala, S., Mordi, G., Lee, B., et al. (2012) Atomic Layer Deposition of Dielectrics on Graphene Using Reversibly Physisorbed Ozone. *ACS Nano*, **6** (3), 2722–2730.

29. Nayfeh, O.M., Marr, T., and Dubey, M. (2011) Impact of Plasma-Assisted Atomic-Layer-Deposited Gate Dielectric on Graphene Transistors. *IEEE Electron Device Lett.*, **32** (4), 473–475.

30. Lim, T., Kim, D., and Ju, S. (2013) Direct deposition of aluminum oxide gate dielectric on graphene channel using nitrogen plasma treatment. *Appl. Phys. Lett.*, **103** (1), 13107.

31. Vervuurt, R.H.J., Karasulu, B., Verheijen, M.A., et al. (2017) Uniform Atomic Layer Deposition of Al_2O_3 on Graphene by Reversible Hydrogen Plasma Functionalization. *Chem. Mater.*, **29** (5), 2090–2100.

32. Robinson, J.A., LaBella, M., Zhu, M., et al. (2011) Contacting graphene. *Appl. Phys. Lett.*, **98** (5), 53103.

33. Foley, B.M., Hernández, S.C., Duda, J.C., et al. (2015) Modifying Surface Energy of Graphene via Plasma-Based Chemical Functionalization to Tune Thermal and Electrical Transport at Metal Interfaces. *Nano Lett.*, **15** (8), 4876–4882.

34. Ma, B., Gong, C., Wen, Y., et al. (2014) Modulation of contact resistance between metal and graphene by controlling the graphene edge, contact area, and point defects: An ab initio study. *J. Appl. Phys.*, **115** (18), 183708.

35. Vervuurt, R.H.J., Sharma, A., Jiao, Y., et al. (2016) Area-selective atomic layer deposition of platinum using photosensitive polyimide. *Nanotechnology*, **27** (40), 405302.

36. Knoops, H.C.M., Mackus, A.J.M., Donders, M.E., et al. (2009) Remote Plasma ALD of Platinum and Platinum Oxide Films. *Electrochem. Solid-State Lett.*, **12** (7), G34.

37. Blöchl, P.E. (1994) Projector augmented-wave method. *Phys. Rev. B*, **50** (24), 17953–17979.

38. Kresse, G., and Joubert, D. (1999) From ultrasoft pseudopotentials to the projector augmented-wave method. *Phys. Rev. B*, **59** (3), 1758–1775.

39. Kresse, G., and Hafner, J. (1993) Ab initio molecular dynamics for liquid metals. *Phys. Rev. B*, **47** (1), 558–561.

40. Kresse, G., and Hafner, J. (1994) Ab initio molecular-dynamics simulation of the liquid-metal–amorphous-semiconductor transition in germanium. *Phys. Rev. B*, **49** (20), 14251–14269.

41. Kresse, G., and Furthmüller, J. (1996) Efficiency of ab-initio total energy calculations for metals and semiconductors using a plane-wave basis set. *Comput. Mater. Sci.*, **6** (1), 15–50.

42. Kresse, G., and Furthmüller, J. (1996) Efficient iterative schemes for ab initio total-energy calculations using a plane-wave basis set. *Phys. Rev. B*, **54** (16), 11169–11186.

43. Vanin, M., Mortensen, J.J., Kelkkanen, A.K., et al. (2010) Graphene on metals: A van der Waals density functional study. *Phys. Rev. B*, **81** (8), 81408.

44. Mostaani, E., Drummond, N.D., and Fal'Ko, V.I. (2015) Quantum Monte Carlo Calculation of the Binding Energy of Bilayer Graphene. *Phys. Rev. Lett.*, **115** (11), 1–5.

45. Klimeš, J., Bowler, D.R., and Michaelides, A. (2010) Chemical accuracy for the van der Waals density functional. *J. Phys. Condens. Matter*, **22** (2), 22201.

46. Lee, K., Murray, É.D., Kong, L., et al. (2010) Higher-accuracy van der Waals density functional. *Phys. Rev. B - Condens. Matter Mater. Phys.*, **82** (8), 3–6.

47. Hohenberg, P., and Kohn, W. (1964) Inhomogeneous Electron Gas. *Phys. Rev.*, **136** (3B), B864–B871.

48. Kohn, W., and Sham, L.J. (1965) Self-Consistent Equations Including Exchange and Correlation Effects. *Phys. Rev.*, **140** (4A), A1133–A1138.

49. Medeiros, P.V.C., Tsirkin, S.S., Stafstrom, S., and Bjork, J. (2015) Unfolding spinor wave functions and expectation values of general operators: Introducing the unfolding-density operator. *Phys. Rev. B - Condens. Matter Mater. Phys.*, **91** (4), 1–5.

50. Medeiros, P.V.C., Stafström, S., and Björk, J. (2014) Effects of extrinsic and intrinsic perturbations on the electronic structure of graphene: Retaining an effective primitive cell band structure by band unfolding. *Phys. Rev. B - Condens. Matter Mater. Phys.*, **89** (4).

51. Nourbakhsh, A., Cantoro, M., Klekachev, A. V., et al. (2011) Single Layer vs Bilayer Graphene: A Comparative Study of the Effects of Oxygen Plasma Treatment on Their Electronic and Optical Properties. *J. Phys. Chem. C*, **115** (33), 16619–16624.

52. Nourbakhsh, A., Cantoro, M., Vosch, T., et al. (2010) Bandgap opening in oxygen plasma-treated graphene. *Nanotechnology*, **21** (43), 435203.

53. Wang, Q., Pang, R., and Shi, X. (2015) Molecular Precursors-Induced Surface Reconstruction at Graphene/Pt(111) Interfaces. *J. Phys. Chem. C*, (111), 150928155727005.

54. Min, K.-A., and Hong, S. (2015) Doping effect in graphene on oxide substrates: MgO(111) and SiO2(0001). *Curr. Appl. Phys.*, **15** (111), S103–S107.

55. Gao, H., Wang, L., Zhao, J., et al. (2011) Band gap tuning of hydrogenated graphene: H coverage and configuration dependence. *J. Phys. Chem. C*, **115** (8), 3236–3242.

56. Vervuurt, R.H.J., Karasulu, B., Thissen, N.F.W., et al. Pt-Graphene Contacts Fabricated by Plasma Functionalization and Atomic Layer Deposition. *To be Publ.*

57. Tang, W., Sanville, E., and Henkelman, G. (2009) A grid-based Bader analysis algorithm without lattice bias. *J. Phys. Condens. Matter*, **21** (8), 84204.

58. Neugebauer, J., and Scheffler, M. (1992) Adsorbate-substrate and adsorbate-adsorbate interactions of Na and K adlayers on Al(111). *Phys. Rev. B*, **46** (24), 16067–16080.

59. Schwan, J., Ulrich, S., Batori, V., et al. (1996) Raman spectroscopy on amorphous carbon films. *J. Appl. Phys.*, **80** (1), 440.

60. Ferrari, A.C., and Basko, D.M. (2013) Raman spectroscopy as a versatile tool for studying the properties of graphene. *Nat. Nanotechnol.*, **8** (4), 235–246.

61. Eckmann, A., Felten, A., Mishchenko, A., et al. (2012) Probing the Nature of Defects in Graphene by Raman Spectroscopy. *Nano Lett.*, **12** (8), 3925–3930.

62. Lin, Y.-C., Lu, C.-C., Yeh, C.-H., et al. (2012) Graphene Annealing: How Clean Can It Be? *Nano Lett.*, **12** (1), 414–419.

63. Zhu, W., Low, T., Perebeinos, V., et al. (2012) Structure and Electronic Transport in Graphene Wrinkles. *Nano Lett.*, **12** (7), 3431–3436.

64. Färm, E., Kemell, M., Ritala, M., and Leskelä, M. (2008) Selective-Area

Atomic Layer Deposition Using Poly(methyl methacrylate) Films as Mask Layers. *J. Phys. Chem. C*, **112** (40), 15791–15795.

65. Elias, D.C., Nair, R.R., Mohiuddin, T.M.G., et al. (2009) Control of Graphene's Properties by Reversible Hydrogenation: Evidence for Graphane. *Science*, **323** (5914), 610–613.

66. Luo, Z., Yu, T., Kim, K., et al. (2009) Thickness-Dependent Reversible Hydrogenation of Graphene Layers. *ACS Nano*, **3** (7), 1781–1788.

67. Reeves, G.K. (1980) Specific contact resistance using a circular transmission line model. *Solid. State. Electron.*, **23** (5), 487–490.

68. Marlow, G.S., and Das, M.B. (1982) The effects of contact size and non-zero metal resistance on the determination of specific contact resistance. *Solid. State. Electron.*, **25** (2), 91–94.

69. Ahmad, M., and Arora, B.M. (1992) Investigation of AuGeNi contacts using rectangular and circular transmission line model. *Solid. State. Electron.*, **35** (10), 1441–1445.

70. Klootwijk, J.H., and Timmering, C.E. (2004) Merits and limitations of circular TLM structures for contact resistance determination for novel III-V HBTs. *Proc. 2004 Int. Conf. Microelectron. Test Struct. (IEEE Cat. No.04CH37516)*, **17** (March), 247–252.

71. Li, J.-L., Kudin, K.N., McAllister, M.J., et al. (2006) Oxygen-Driven Unzipping of Graphitic Materials. *Phys. Rev. Lett.*, **96** (17), 176101.

72. Smith, J.T., Franklin, A.D., Farmer, D.B., and Dimitrakopoulos, C.D. (2013) Reducing Contact Resistance in Graphene Devices through Contact Area Patterning. *ACS Nano*, **7** (4), 3661–3667.

73. Sutter, P., Sadowski, J.T., and Sutter, E. (2009) Graphene on Pt(111): Growth and substrate interaction. *Phys. Rev. B - Condens. Matter Mater. Phys.*, **80** (24), 1–10.

74. Haberer, D., Giusca, C.E., Wang, Y., et al. (2011) Evidence for a New Two-Dimensional C 4 H-Type Polymer Based on Hydrogenated Graphene. *Adv. Mater.*, **23** (39), 4497–4503.

75. Matsuda, Y., Deng, W.-Q., and Goddard, W.A. (2010) Contact Resistance for "End-Contacted" Metal−Graphene and Metal−Nanotube Interfaces from Quantum Mechanics. *J. Phys. Chem. C*, **114** (41), 17845–17850.

Chapter 6

Conclusions & Outlook

6.1 Conclusions

The work presented in this thesis involves several aspects concerning the development of atomic layer deposition (ALD) processes for the growth of uniform dielectrics and metals on graphene. The following general conclusions and findings can be drawn from the work presented.

- Due to the lack of reactive surface sites on graphene, ALD precursor molecules tend to physisorb on graphene instead of forming a chemical bond. This weak precursor-graphene interaction makes ALD on pristine graphene strongly dependent on the graphene cleanliness, and ALD process conditions. The appropriate choice of precursor and an increase of the precursor dose times compared to the standard ALD process can increase the number of physisorbed species on the graphene and improve the deposition uniformity. The use of a lower deposition temperature has a similar effect, but is often accompanied by a lower-quality material being deposited.
- The creation of reactive surface sites on graphene by various surface preparation techniques results in the chemisorption of ALD precursor molecules on graphene. This makes it possible to deposit uniform layers on graphene by ALD. To prevent damage and/or unintentional doping of graphene, functionalization techniques which involve the deposition of metal seed-layers using PVD techniques or polymer seed-layers are best avoided. Methods that use a sacrificial graphene layer or that rely on the physisorption of reactive species at low temperature do not suffer from these adverse effects, but are time consuming due to the requirement of extra processing steps.

In the ideal case one would like to grow ALD films on graphene at the temperature at which the best material properties are obtained. This requires functionalization methods that can withstand high (> 100 °C) temperatures, and at the same time do not damage the graphene. In principle, this provides the optimum material quality, while the pristine properties of graphene are preserved

- In **Chapter 3** a functionalization method involving the use of a H_2 plasma for the creation of reactive sites on graphene is introduced. The plasma treatment creates functional groups on the graphene surface on which the ALD precursor molecules are able to adsorb. With the use of a H_2 plasma treatment, uniform growth of Al_2O_3 layers down to 8 nm in thickness can be achieved on graphene by ALD. In contrast to O_2 plasma treatments, a H_2 plasma treatment does not deteriorate the graphene properties due to the abstraction of the functional groups from the graphene surface upon ALD precursor adsorption. This makes it possible to directly deposit uniform Al_2O_3 layers on graphene without damage to the graphene at relatively high temperatures (up to 200 °C) when compared to other functionalization techniques.
- Apart from the initialization of the growth of dielectric materials also metal ALD benefits from the functionalization of graphene by plasma treatments, as is discussed in **Chapter 5**. Both O_2 and H_2 plasmas can be used to initialize uniform growth of Pt on graphene. In the case of metal ALD on graphene for the fabrication of metal-graphene contacts, the creation of sp^3 carbon as a result of the plasma treatment can be beneficial for the quality of the created metal-graphene contact. Important however, is how the plasma treatment creates these functional groups. In the case of an O_2 plasma treatment amorphization of the graphene occurs. This limits the improvement of the contact resistance due to the damaging of the graphene backbone. Functionalization of the graphene by a H_2 plasma does not result in amorphization of graphene, and leaves the graphene backbone intact further improving the contact resistance.

ALD in combination with H_2 plasma treatments therefore make it possible to deposit high quality dielectrics and metals on graphene, while maintaining the intrinsic properties of graphene. However, like other gas phase deposition techniques, ALD has no inherent growth control in the lateral dimension, which is desired for many device applications. For this reason area-selective ALD (AS-ALD) methods have gained

significant interest. AS-ALD methods often rely on polymers or SAMs that block ALD growth and have a relatively low temperature stability (< 150 °C). Many ALD process require higher deposition temperatures.

- To allow for higher ALD deposition temperatures (> 150 °C) a method that uses photosensitive polyimide as a blocking layer for the ALD of Pt was introduced in **Chapter 4**. Polyimide has a much higher temperature stability (> 350 °C), and therefore does not suffer from reflow effects that other polymers have when used at higher temperatures. This allows for a better uniformity of the deposited Pt patterns, and superior pattern definition. Normally polyimide has the disadvantage that it is difficult to remove after processing. However, in this case the polyimide could easily be removed after Pt ALD by a H_2 plasma treatment. This is most likely due to the weakening of the polyimide during the ALD process or the catalytic activity of Pt traces on the polyimide surface.
- The combination of AS-ALD to block ALD growth and plasma treatments to initiate the ALD growth of Pt made it possible to deposit Pt patterns on graphene for the fabrication of metal graphene contacts, see **Chapter 5**. Despite the use of long plasma treatments that are required to activate the growth on graphene the Pt process remained selective. This indicates that the polyimide is not modified by the plasma treatments and might offer opportunities for the AS-ALD of plasma ALD processes.

6.2 Outlook

The results obtained in this thesis illustrate that a H_2 plasma pre-treatment combined with ALD is a promising method for the integration of graphene in future device applications. Still some open questions remain, as well as opportunities for further research.

- The current approach of using H_2 plasma treatment to create functional groups followed by ALD of Al_2O_3 limits the minimum thickness required to obtain a closed layer to ~ 8 nm. To further reduce the minimum thickness several approaches are worth investigating. One method could be the use of multiple H_2 plasma exposure steps in a so-called supercycle ALD process where after every *X* number of cycles a H_2 plasma is used. The repetition of the H_2 plasma

exposure, would functionalize the areas that are not functionalized during initial exposure, for example areas covered, with polymer residue. These areas probably require a longer H_2 plasma exposure before functionalization is achieved, since the residual polymer needs to be removed first by the plasma treatment. This can be done by repeating the plasma treatment every so many cycles, while at the same the graphene already covered by Al_2O_3 is protected during the plasma exposure. The repetition of the H_2 plasma exposure could therefore reduce the number of ALD cycles required to form a uniform layer, making the deposition of thinner dielectrics on graphene possible.

- The presence of ions, and photons in the plasma most likely limits the reversibility of the H_2 plasma treatment. These species can remove carbon atoms from the graphene lattice by breaking C-C bonds, creating defects in the graphene. Lowering the ion energy or using alternative methods to hydrogenate the graphene, such as hot-wire dissociation of H_2, might increase the amount of hydrogen groups on the graphene before it is irreversibly damaged.
- The exploration of different plasmas to functionalize the graphene for the initiation of ALD growth is also of interest. From the results presented in this thesis it can be concluded that the functional groups created by an O_2 plasma are too stable to be removed by subsequent ALD processing, whereas the functional groups created by a H_2 plasma are already partially removed at processing temperatures < 200 °C. It would therefore be interesting to study the stability of functional groups created by other plasma treatments such as N_2 plasmas or SF_6 plasmas. These might have a higher temperature stability compared to H_2 but weaker compared to O_2. This would allow ALD processing at temperatures above 200 °C, while maintaining functional group reversibility. XeF_2 gas treatments of graphene for example have shown that F containing functional groups are stable up to 225 °C, but do not result in a change of the graphene properties after ALD [1]. Creating these groups by a plasma might make it possible to increase the ALD temperature further.

The type of plasma treatment and how it its integrated in the process flow is important for the quality and minimum thickness of the layer deposited by ALD, as well as the preservation of the pristine properties of the graphene. Apart from the plasma functionalization also other changes in the ALD process are of interest.

- Currently, the choice of ALD precursor used for the deposition on graphene is largely based on availability, cost and process ease. The use of different ALD precursors that are specifically tailored to have a high physisorption energy on graphene, would be beneficial for the deposition of thinner uniform-layers on graphene. Precursors with cyclopentadienyl, benzene or similar ligands interact relatively strongly with the graphene via pi-stacking mechanisms, due to their similar sp^2 carbon hybridization [2]. Choosing precursors containing these ligands for ALD on graphene could therefore be beneficial for the deposition uniformity.
- The deposition of dielectrics other than Al_2O_3 is also of importance. Al_2O_3 is a robust, well understood ALD process that can be used to prove a functionalization concept. However, in terms of dielectric performance and current leakage other dielectric materials far outperform Al_2O_3. TiO_2 is an interesting alternative in this regard. The dielectric constant of TiO_2 (83-160) is much higher than Al_2O_3 (8-9) and the more commonly used HfO_2 (16-24). In Si FET fabrication the use of TiO_2 is avoided. This is because a low quality SiO_2 layer tends to form at the interface between TiO_2 and Si deteriorating device performance [3]. Graphene however, has no native oxide and therefore does not suffer from the formation of an interfacial sub-oxide. This makes TiO_2 a promising dielectric to be used in graphene devices.

Besides graphene, other 2D materials, such as MoS_2 and BN, also lack reactive surface sites which could hinder ALD growth on these materials as well.

- Presently the quality of these 2D materials, still tends to vary considerably [4], and their grain sizes are relatively small [5]. This means that sufficient reactive sites, such as grain boundaries, are present. Therefore ALD growth on these materials is often uniform. However, with the continued improvement of 2D material synthesis methods, mostly aimed at increasing the grain size of the material, it will also become more difficult to obtain uniform ALD growth on them [6]. Functionalization of these materials using plasma pre-treatments could therefore be of use for these materials as well. Furthermore plasma functionalization might make it possible to grow different 2D materials directly on top of each other.

References

1. Wheeler, V., Garces, N., Nyakiti, L., et al. (2012) Fluorine functionalization of epitaxial graphene for uniform deposition of thin high-κ dielectrics. *Carbon*, **50** (6), 2307–2314.

2. Björk, J., Hanke, F., Palma, C.-A., et al. (2010) Adsorption of Aromatic and Anti-Aromatic Systems on Graphene through π−π Stacking. *J. Phys. Chem. Lett.*, **1** (23), 3407–3412.

3. Brillson, L.J., Slade, M.L., Richter, H.W., et al. (1985) Control of titanium silicon and silicon dioxide reactions by low temperature rapid thermal annealing. *Appl. Phys. Lett.*, **47** (10), 1080–1082.

4. Yu, J., Li, J., Zhang, W., and Chang, H. (2015) Synthesis of high quality two-dimensional materials via chemical vapor deposition. *Chem. Sci.*, **6**, 6705–6716.

5. Groven, B., Heyne, M., Nalin Mehta, A., et al. (2017) Plasma-Enhanced Atomic Layer Deposition of Two-Dimensional WS2 from WF_6 , H_2 Plasma, and H_2S. *Chem. Mater.*, **29** (7), 2927–2938.

6. McDonnell, S., Brennan, B., Azcatl, A., et al. (2013) HfO_2 on MoS_2 by atomic layer deposition: Adsorption mechanisms and thickness scalability. *ACS Nano*, **7** (11), 10354–10361.

Summary

Atomic Layer Deposition of Graphene: Towards Graphene Device Integration

Graphene is a two-dimensional material that has attracted considerable scientific interest over the past few years, due to its exceptional mechanical, electrical and optical properties, which make it a promising candidate for post-silicon optical and electronic devices. For device integration the ability to deposit thin high-κ dielectrics and metals on graphene is essential. To deposit these layers atomic layer deposition (ALD) is the method of choice, due to its ability to deposit uniform high-quality materials with sub-monolayer thickness control. ALD on pristine graphene, however, is a challenge due to the lack of out-of-plane bonds. ALD growth of dielectrics and metals on pristine graphene therefore only occurs on defect sites or grain boundaries where dangling bonds or functional groups are present.

To overcome these nucleation issues several different surface preparation techniques to initialize ALD on graphene have been explored over the years and are critically reviewed in chapter 2. An overview of the different functionalization methods to achieve uniform ALD growth is presented together with their advantages and disadvantages. Among the different functionalization methods, plasma functionalization shows promise due to its processing ease, compatibility with silicon technology and limited amount of extra processing steps required. However, when O_2 or N_2 plasmas are used for functionalization, the sp^2 backbone of graphene is damaged, deteriorating its electrical properties, such as the charge carrier mobility.

In chapter 3 a new method to deposit ultrathin, uniform Al_2O_3 layers on graphene using reversible H_2 plasma functionalization followed by ALD is introduced. It is shown that H_2 plasma functionalization of graphene leads to uniform ALD of closed Al_2O_3 films down to 8 nm in thickness. Hall measurements and Raman spectroscopy reveal that the hydrogen plasma functionalization is reversible upon Al_2O_3 ALD and does not deteriorate the graphene charge carrier mobility. Density functional theory DFT analysis of the possible reaction pathways for $Al(CH)_3$ precursor adsorption on hydrogenated graphene predict a H_2 and CH_4 release mechanism that cleans off the hydrogen functionalities from the graphene surface, which explains the observed reversibility of the hydrogen plasma functionalization of graphene upon Al_2O_3 ALD.

The use of H_2 and O_2 plasma functionalization to initialize ALD growth on graphene is also exploited for the fabrication of metal-graphene contacts. First we developed an area-selective ALD (AS-ALD) process for the selective deposition of Pt using photosensitive polyimide, in chapter 4. The polyimide can be patterned using photolithography and acts as a blocking layer, preventing the adsorption of the Pt ALD precursor. The high temperature stability of the polyimide made it ideal for the selective deposition of Pt at 300 °C, yielding an improved uniformity of the Pt deposits and superior definition of the Pt patterns compared to the more commonly used poly(methyl-methacrylate) resist.

The combination of polyimide to block ALD growth and plasma treatments to initiate ALD growth on graphene, allowed for the fabrication of high-quality Pt-graphene contacts, shown in chapter 5. Improved contact resistances were measured compared to standard evaporated Pt-graphene contacts. Furthermore, H_2 plasma functionalization resulted in better contact resistances than O_2 plasma functionalization. This was explained by a different edge termination of the graphene after a H_2 or O_2 plasma (C-H vs. C=O).

In conclusion, in this work it is demonstrated that a H_2 plasma functionalization is an excellent way to enable direct ALD growth on graphene. Most of this thesis work has been or will be published in peer-review scientific journals, and provides new opportunities for the integration of graphene in devices for various applications.

Contributions of the Author

The research project presented in this work was entitled: 'A physical-analytical approach to atomic layer deposition of ultra-thin high-κ dielectrics on graphene' and aimed at the fabrication of ultrathin (< 10 nm), uniform, pinhole free oxides on graphene by ALD. The project consisted of two parts: An experimental part focusing on the development of new ALD processes for uniform film growth on graphene, and a theoretical part focusing on the atomistic scale simulations of ALD chemistry on graphene. The experimental part was related to a PhD student position – taken up by the author of this thesis – whereas the theoretical part was related to a post doctorate position – taken up by Dr. B. Karasulu.

The work presented in this thesis encompasses the original work coordinated and carried out by the PhD student. Nonetheless, some parts of this thesis deserve extra clarification.

The work presented in **Chapter 3** and **Chapter 5** is the result of the collaboration between the author and Dr. B. Karasulu. The experiments were designed and performed by the author, and the atomistic scale simulations used to support the experimental work were performed by Dr. B. Karasulu. The author assisted in the understanding and presentation of these simulations.

Similarly, Dr. B. Karasulu designed experiments focusing on the atomistic scale simulations involving the ALD precursor adsorption on graphene. These simulations were corroborated with experimental work from the author. This work is not included in this thesis, but can be found in list of publications related to this work.

List of Peer-Reviewed Publications

This Thesis

- **R.H.J. Vervuurt**, W.M.M. Kessels & A.A. Bol, 'Atomic Layer Deposition for Graphene Device Integration' Advanced Materials Interfaces 1700232 (2017)

- **R.H.J. Vervuurt**, B. Karasulu, M.A. Verheijen, W.M.M. Kessels & A.A. Bol, 'Uniform Atomic Layer Deposition of Al_2O_3 on Graphene by Reversible Hydrogen Plasma Functionalization' Chemistry of Materials, 29(5), 2090-2010 (2017)

- **R.H.J. Vervuurt**, A. Sharma, Y. Jiao, W.M.M. Kessels & A.A. Bol, 'Area-selective atomic layer deposition of platinum using photosensitive polyimide' Nanotechnology, 27(40), 405302 (2016)

- **R.H.J. Vervuurt**, B. Karasulu, N.F.W. Thissen, Y. Jiao, J.W. Weber, W.M.M. Kessels & A.A. Bol, 'Pt-Graphene Contacts Fabricated by Plasma Functionalization and Atomic Layer Deposition' to be submitted

Related to this work

- W.T.E. Van Den Beld, M. Odijk, **R.H.J. Vervuurt**, J.W. Weber, A.A. Bol, A. Van Den Berg, & J.C.T. Eijkel, 'In-situ Raman spectroscopy to elucidate the influence of adsorption in graphene electrochemistry' Scientific Reports, 7:45080 (2017)

- N.F.W. Thissen, **R.H.J. Vervuurt**, A.J.M. Mackus, J.J.L Mulders, J.W. Weber W.M.M. Kessels & A.A. Bol, 'Graphene devices with bottom-up contacts by area-selective atomic layer deposition' 2D Materials, 4(2), 025046-025046 (2017)

- B. Karasulu, **R.H.J. Vervuurt**, W.M.M. Kessels & A.A. Bol, 'Continuous and ultrathin platinum films on graphene using atomic layer deposition' Nanoscale, 8(47), 19829-19845 (2016)

- L. Gao, Y. Cui, **R.H.J. Vervuurt**, D. van Dam, R. van Veldhoven, J.P. Hofmann, A.A. Bol, J.E.M. Havekort, J.E.M. Notten, E.P.A.M. Bakkers & E.J.M. Hensen, 'High-efficiency InP-based photocathode for hydrogen production by interface energetics design and photon management' Advanced Functional Materials, 26(5), 679-686 (2016)

- A.J.M. Mackus, M.J. Weber, N.F.W. Thissen, D. Garcia-Alonso Garcia, **R.H.J. Vervuurt**, S. Assali, A.A. Bol, M.A. Verheijen & W.M.M. Kessels, 'Atomic layer deposition of Pd and Pt nanoparticles for catalysis' Nanotechnology, 27(3), 034001 (2016)

- N.F.W. Thissen, **R.H.J. Vervuurt**, J.J.L. Mulders, J.W. Weber, W.M.M. Kessels & A.A. Bol, 'The effect of residual gas scattering on Ga ion beam patterning of graphene' Applied Physics Letters, 107, 2131101 (2015)

- C.A. Wolden, K. Adeyemo, **R.H.J. Vervuurt**, M. Ostwal & J.D. Way, 'Mechanistic studies of hydrogen transport through MO_2C/V composite membranes' Journal of Membrane Science, 427, 150-154 (2013)

Acknowledgements

I have had a lot of fun during my stay in the PMP group. The atmosphere within the group both during work and outside of it has always been incredible. Though all of you make PMP a great place to work, there are some people that I would like to thank specifically.

First of all I would like to thank **Ageeth** for giving me the opportunity to continue at PMP after my Master even though there was not directly a project available. Your enthusiasm and conviction that in the end it would all work out, is wat made this work a success. The time you invested in the many corrections of my work, have really helped improve my writing skills. I also appreciated the efficiency of our meetings. I don't think we ever had a meeting that lasted longer than half an hour. This brings me to the next person on the list. **Erwin**, short meetings or MoMo's are not your strongpoint. However, despite this (minor) flaw, your dedication and attention to detail, which is second to none, is one of the reasons why PMP is such a great group. I appreciate the effort you took in reading and correcting my work, it really helped to "take it to a higher level". Next I would like to thank the people directly involved in the work that helped bring about this thesis, **Jan-Willem**, **Bora**, **Nick**, **Akhil, Marcel** and **Yuqing**. J-W, it was always a pleasure to work with you in the lab, especially testing crazy graphene transfer methods on the Friday afternoon. Bora, your calculations complimented my experimental work perfectly, together we formed a great team. I also would like to thank my Bachelor and Master students, **Remco**, **Yuri** & **Karsten**. Even though your projects were often not related to my work directly, it was always nice to discuss the details of graphene growth with you. Seeing you face the randomness that transferring graphene can be, helped me realize that some things are out of one's control. Your enthusiasm for the work we were doing, motivated me for my own.

The technicians of PMP should of course not be forgotten: **Janneke**, **Joris**, **Caspar**, **Cristian** and **Jeroen**. Your continued effort to keep the lab up and running, despite my best efforts to do otherwise, is truly amazing. Much of the research we do would not be possible, or would at least take a lot longer, without your help. Also the coffee breaks, lunches and general entertainment in the lab (Joris, although your music taste is debatable) wouldn't be the same without you. The secretaries **Jeanne** and **Lianne**, for helping filling in the many forms, declarations and procedures that seem to change every other week.

The Colorado 4, **Bas**, **Bart** and **Nick** (excluding myself here). I could always count on you for comic relief. When all four of us are around a serious conversation is

impossible, thanks Bas. The Road trips we made in the USA were the best, I hope we continue this in the future. Nick, we could always count on you for driving. However, the next time you decide to go drifting in the snow, please let us out first. Bart, your word jokes can drive anyone crazy, though I must say I have learned to appreciate (expect) them over time. I should of course not forget our aspiring member **Roger**, nothing escapes your eye, nor your opinion. Furthermore I would like to thank **Harm**, **Martijn, Cristian** and **Valerio** who joined on "conferences" to Costa Rica, USA, Japan or Finland. I really enjoyed our time traveling together.

Furthermore I would like to thank **Florian, Vincent, Harm, Adrie, Chai, Roger, Martijn, Martine, Sonali, Nick, Bart** and other **Bart** for the amazing times at Octoberfest. Whether it was Munich, Sittard or Nara, bad (or good?) German music, and beer for that matter, was never in short supply. Since we are talking about drinking, I shouldn't forget the Borrel, everyone shows up here at some point during their stay at PMP, some more often than others. Other **Bart**, and more recently also **Marija**, I could always count on you on a Thursday afternoon. Furthermore I would like to thank everyone at PMP for the great atmosphere within the group and for putting up with my sarcastic comments, especially **Sonali**.

Danny and **Mike,** fellow members of " Zjwumclub de Spetters". Our bi-weekly excursions to Germany always helped me relax and forget the stress from work. Last I would like to thank my **Family** for their continued support. Mom, dad, I really appreciate all that you have done for me.

Curriculum Vitae

14 August 1989	Born in Roermond, The Netherlands
2001 – 2007	VWO Diploma *cum laude* Bisschoppelijk College Schöndeln Roermond
2007 – 2010	Bachelor Degree Applied Physics *cum laude* Eindhoven University of Technology
2010 – 2012	Master Degree Applied Physics Eindhoven University of Technology
Spring 2011	Research Internship in the group of prof. C.A. Wolden Colorado School of Mines, Golden, USA.
2013-2017	PhD. Student in the Plasma & Materials Processing Group Department of Applied Physics Eindhoven University of Technology